
Electronic Thesis and Dissertation Repository

9-5-2013 12:00 AM

Piezoelectric Transformer and Hall-Effect Based Sensing and Disturbance Monitoring Methodology for High-Voltage Power Supply Lines

Sneha Arun Lele
The University of Western Ontario

Supervisor
Dr. Robert Sobot
The University of Western Ontario Joint Supervisor
Dr. Tarlochan S. Sidhu
The University of Western Ontario

Graduate Program in Electrical and Computer Engineering
A thesis submitted in partial fulfillment of the requirements for the degree in Doctor of Philosophy

© Sneha Arun Lele 2013

Follow this and additional works at: <https://ir.lib.uwo.ca/etd>



Part of the [Power and Energy Commons](#), [Signal Processing Commons](#), and the [VLSI and Circuits, Embedded and Hardware Systems Commons](#)

Recommended Citation

Lele, Sneha Arun, "Piezoelectric Transformer and Hall-Effect Based Sensing and Disturbance Monitoring Methodology for High-Voltage Power Supply Lines" (2013). *Electronic Thesis and Dissertation Repository*. 1618.

<https://ir.lib.uwo.ca/etd/1618>

This Dissertation/Thesis is brought to you for free and open access by Scholarship@Western. It has been accepted for inclusion in Electronic Thesis and Dissertation Repository by an authorized administrator of Scholarship@Western. For more information, please contact wlsadmin@uwo.ca.

PIEZOELECTRIC TRANSFORMER AND HALL-EFFECT BASED
SENSING AND DISTURBANCE MONITORING METHODOLOGY FOR
HIGH-VOLTAGE POWER SUPPLY LINES
(Thesis format: Monograph)

by

Sneha Lele

Graduate Program in Electrical and Computer Engineering

A thesis submitted in partial fulfillment
of the requirements for the degree of
Doctor of Philosophy

The School of Graduate and Postdoctoral Studies
The University of Western Ontario
London, Ontario, Canada

© Sneha Arun Lele 2013

Abstract

Advancements in relaying algorithms have led to an accurate and robust protection system widely used in power distribution. However, in low power sections of relaying systems, standard voltage and current measurement techniques are still used. These techniques have disadvantages like higher cost, size, electromagnetic interference, resistive losses and measurement errors and hence provide a number of opportunities for improvement and integration. We present a novel microsystem methodology to sense low-power voltage and current signals and detect disturbances in high-voltage power distribution lines. The system employs dual sensor architecture that consists of a piezoelectric transformer in combination with Hall-effect sensor, used to detect the disturbances whose harmonics are in the kHz frequency range.

Our numerical analysis is based on three-dimensional finite element models of the piezoelectric transformer (PT) and the principle of Hall-effect based “Integrated Magnetic Concentrator (IMC)” sensor. This model is verified by using experimental data recorded in the resonant frequency and low frequency regions of operation of PT for voltage sensing. Actual measurements with the commercial IMC sensor too validate the modelling results.

These results describe a characteristic low frequency behaviour of rectangular piezoelectric transformer, which enables it to withstand voltages as high as 150V. In the frequency range of 10Hz to 250Hz, the PT steps down 10–150V input with a linearity of $\pm 1\%$. The recorded group delay data shows that propagation delay through PT reduces to few microseconds above 1kHz input signal frequency. Similarly, the non-intrusive current sensor detects current with a response time of $8\mu\text{s}$ and converts the current into corresponding output voltage. These properties, in addition to frequency spectrum of voltage and current input signals, have been used to develop a signal processing and fault detection system for two real-time cases of faults to produce a 6-bit decision logic capable of detecting various types of line disturbances in less than 3ms of delay.

Keywords: piezoelectric transformer, analysis, frequency, numerical modelling, signal processing, filter, delay, Hall-effect, flux, current sensing, magnetic concentrator

Acknowledgements

Graduate studies at The University of Western Ontario have been an enriching learning experience and I would like to acknowledge all those who have been a significant part of this journey.

Firstly, I would like to thank Dr. Robert Sobot and Dr. Tarlochan S. Sidhu, my supervisors, for giving me an opportunity to work on this project and graciously supporting me throughout the duration of this course. I express my deepest gratitude to Dr. Sobot for his constant support, guidance and encouragement. He has been a mentor along with being my advisor, without his support and patience this work would not have been possible.

I am grateful to the Electrical and Computer Engineering department at The University of Western Ontario for providing the necessary funding, facilities and a suitable work environment. My special thanks to all the course instructors, to the electronics shop and to all the staff members for their timely support. I would also like to express my gratitude to GE Multilin and CMC Microsystems for supporting our research. I am grateful to all the examiners and the chair who offered to be part of the defense examination and provided me with useful evaluations and feedback on my thesis.

I would like to thank my lab-mates (Na, Shawon, both Kyles) and my house-mates here in London (Rachita, Aditi, Prakruti, Veena) who have been like a family to me away from home. My sincere thanks to all my friends (Karthick, HK, Sri, Viji to name a few) for making all these years enjoyable and worthwhile.

My wholehearted thanks to my sister (Amruta) and all the relatives and friends who never stop believing in me. Last but not the least, I would like to express my heartfelt gratitude to my mother (Vasudha Lele) who has struggled all her life and made this day possible for me. She has been my constant source of inspiration. I dedicate this work to my father (Arun Lele) who is not between us but has always been alive in our memories.

Contents

Abstract	ii
Acknowledgements	iii
List of Figures	vii
List of Tables	x
List of Abbreviations and Symbols	xi
1 Introduction	1
1.1 Overview	1
1.2 Scope, objective and contributions of the thesis	6
1.3 Organization of the thesis	9
2 Piezoelectric Transformer	10
2.1 Piezoelectricity	11
2.1.1 Basic principle	11
2.1.2 Properties and operating modes	12
2.2 Piezoelectric transformers	14
2.2.1 Types and configurations of PTs	15
2.2.2 Application specific PT structures	16
2.3 Electrical Representation	17
2.3.1 Mathematical modelling	18
2.3.2 Electrical equivalent model	25
2.4 Summary	27
3 Current sensor	28
3.1 Current Sensing Techniques	28
3.1.1 Resistive current sensing	29
3.1.2 Magnetic current sensing	30
3.1.3 Optical current sensing	31
3.2 Hall-effect based current sensing	33
3.2.1 Hall effect principle	33
3.2.2 Integrated magnetic concentrator based Hall-effect sensing	35
3.3 Summary	37

4	Modelling and Experimental Analysis – Piezoelectric Transformer	38
4.1	Finite Element Modelling and Simulation	38
4.1.1	Evolution of FEM analysis	39
4.1.2	Modelling using COMSOL	40
	Natural Resonant Modes	44
	Frequency Domain Behaviour	46
	Time Domain Analysis	48
4.1.3	Other considerations	51
	Group delay	51
	Propagation velocity, PT dimension and resonant frequency	52
	Initial displacement and loss factors	53
4.2	Experimental Results	54
4.2.1	Device under test	54
4.2.2	Experimental requirements and set-up	56
4.2.3	Single-tone results	58
4.2.4	Loading Effect	60
4.2.5	Real-time analysis	62
4.2.6	Experimental group delay measurement	64
4.3	Limitations of PT considering existing system conditions	66
4.3.1	Mechanical considerations	67
4.3.2	Non-linearity and Hysteresis	69
4.3.3	Material properties, ageing and effect of temperature	70
4.4	Summary	71
5	Modelling and Experimental Analysis – Hall sensor	74
5.1	Device under test	75
5.2	COMSOL model and effect of real-time PS CAD current signals	76
5.3	Other considerations in IMC based Hall sensing	83
5.4	Summary	84
6	Signal processing system	85
6.1	Background and introduction	85
6.2	Fault detection technique	87
6.3	Frequency spectrum of the input signals	88
6.4	Signal processing and decision making system	90
6.4.1	Behavioural model and logic	91
6.4.2	PT output and High Pass Filter	94
6.4.3	Envelope detection and comparator action	97
6.4.4	Digital output bit representation	99
	Bit 1 output	99
	Bit 2 output	102
	Bits 4 and 5 output	103
6.4.5	Actual circuit implementation	108
	Buffer circuit	108
	Filters and Peak detector circuit	108

Comparator circuit	109
6.5 Summary	109
7 Conclusions and Future Work	111
7.1 Conclusions	111
7.2 Future Work	114
Bibliography	115
Appendix A : <i>COMSOL</i> piezoelectric general equations	128
Appendix B : <i>MATLAB</i> functions in signal processing model	129
Curriculum Vitae	131

List of Figures

1.1	Block diagram of a typical microprocessor-based relay system used in power distribution substations.	3
1.2	Simplified schematic diagram of voltage and current step-down techniques for input to relay; typical voltage transformation method (top), typical current transformation method (bottom).	4
1.3	Block diagram of the proposed signal monitoring system.	7
2.1	Polarization process to generate piezoelectric effect	11
2.2	Plot of the dielectric hysteresis loop for a PZT material.	12
2.3	Simplified diagram showing geometry of a typical Rosen type piezoelectric transformer.	14
2.4	Plot of the first three fundamental harmonics inside a piezo element.	14
2.5	Thickness vibration mode PT	15
2.6	Radial vibration mode PT	16
2.7	Stress-strain cycle that defines electromechanical coupling coefficient.	19
2.8	Input part of Rosen PT vibrating in thickness mode.	21
2.9	Output part of the Rosen PT vibrating in the longitudinal mode	24
2.10	Simplified schematic diagram of electrical model of PT	25
2.11	Simulated efficiency plot at resonance for varying load in electrical model. . . .	26
3.1	Simplified diagram of Hall-effect operational principle.	33
3.2	Simple configuration of a basic Hall-effect sensor	34
3.3	Hall-effect based sensing using Integrated Magnetic flux Concentrators.	36
4.1	Block diagram showing key steps involved in PT modelling with <i>COMSOL</i> Multiphysics software and <i>MEMS</i> modules.	40
4.2	Orthogonal polarizations in input and output sections of PT.	42
4.3	Free tetrahedral meshing applied to <i>COMSOL</i> PT model.	42
4.4	3D plots for PT displacement (volume deformation) in nm at eigen frequencies 14.79kHz, 40.71kHz, 75.62kHz, 120.57kHz, 168.05kHz and 209.04kHz	44
4.5	3D plots for PT displacement in nm (top) and output potential in V (bottom) at resonance	45
4.6	Simulated susceptance at the output terminal of PT model at main resonant frequency and at second harmonic frequency.	46
4.7	Simulated frequency response of PT model showing main resonance and second harmonic frequency (top), low frequency response (bottom) with 10M Ω load termination for varying input voltage.	47

4.8	Simulated effect of resistive loading on PT model output behaviour in <i>COMSOL</i> at varying frequencies.	48
4.9	Typical types of faults in a 3 Φ power system.	49
4.10	Time-domain <i>PSCAD</i> generated voltage signal applied to PT model as input. .	50
4.11	Stepped down output voltage of PT model for high voltage time-domain input applied	50
4.12	Simulated phase delay between input to PT model and output recorded for that input for 60Hz component.	51
4.13	Simulated phase delay between input to PT model and output recorded for that input for high frequency component.	52
4.14	Photo of input and output connections for single-ended PT.	54
4.15	PT configurations: Single ended connection (left), differential connection (right)	55
4.16	Experimental set-up for measurements with real-time input signals.	56
4.17	Most recent experimental set-up for measurements with real-time input signals.	57
4.18	Experimentally recorded frequency response showing main resonance and second harmonic frequency (top), low frequency response (bottom) with no load condition for varying input voltage.	58
4.19	Experimentally recorded low frequency response for 100V _{rms} input overlapped with results of the fitting linear function of the form $y = ax + b$ (top), percentage error between measured output and fitted data (bottom).	59
4.20	Experimentally recorded low frequency response for 100V _{rms} input using a regular BNC compared with passive probe demonstrating loading effect. . . .	60
4.21	Experimentally recorded effect of resistive loading on PT output behaviour for varying frequency	61
4.22	Schematic diagram for <i>PSCAD</i> case 1 power system simulation model example.	63
4.23	Schematic diagram for <i>PSCAD</i> case 2 power system simulation model example.	63
4.24	Stepped down PT output voltage for high power input applied experimentally .	64
4.25	Experimentally measured group delay through PT sample for varying frequencies.	65
4.26	Experimentally observed group delay through PT sample for real-time faulty input signal.	66
4.27	Photo of a PT size compared to a Canadian penny, held using cellophane tape (left), PT clamped on to a PCB using a cable tie (right).	67
4.28	Negligible hysteresis observed during experimental measurements at power-line frequency.	69
4.29	Photo of PT with mechanical defect.	70
5.1	Photo of development kit used for measurements based on IMC MLX91205 IC and its 3D rendering showing narrow conductor width under the IC	75
5.2	3D <i>COMSOL</i> model representing the Hall-effect based IMC concept showing the conductor with lateral Hall elements and two hexagonal magnetic concentrators.	76
5.3	Simulated effect of varying width of the part of the conductor under the Hall elements, on normal magnetic flux density distribution in the <i>COMSOL</i> model.	77

5.4	Simulated z component of magnetic flux density variation observed between the hexagonal concentrators along the two facing boundaries in the model. . . .	78
5.5	Time-domain plot of secondary current exported from <i>PSCAD</i> power system model applied to Hall model in <i>COMSOL</i> , for fault and no fault condition. . .	79
5.6	Time-domain plot of z component of magnetic flux density recorded on concentrator boundaries facing each other in the gap, for time varying input current.	80
5.7	Schematic diagram of direct single-ended connection for the open loop MLX current sensor.	81
5.8	Experimentally recorded MLX output voltage for increasing current, flux variation with current in <i>COMSOL</i> model representation (top), Experimental MLX frequency response, recorded flux change with frequency in <i>COMSOL</i> Hall model representation, for 1A and 5A (bottom).	82
6.1	Block diagram of a signal flow representation showing steps involved in sensing, processing and decision making process in a digital relay.	86
6.2	Frequency spectrum of experimentally recorded piezo outputs for case 1 fault condition.	89
6.3	Frequency spectrum of experimentally recorded piezo outputs for case 2 fault condition.	90
6.4	Frequency spectrum of simulated piezo outputs for case 2 fault condition. . . .	91
6.5	Zoom-in frequency spectrum of 1710Hz centred BP filter for case 2 fault condition, simulated (left) and experimentally recorded (right).	92
6.6	Truth table of decision making system	93
6.7	Behavioural block diagram of the decision making system.	94
6.8	Behavioural block diagram of the signal processing system.	94
6.9	Simulated and experimental piezo output for case 2, fault AB-g condition. . . .	95
6.10	Schematic diagram of high-pass filter circuit representation.	95
6.11	Simulated and experimental piezo output for case 2 (zoomed near fault region), fault AB-g condition (top), HP filtered output (bottom).	96
6.12	Schematic diagram of peak detector circuit based on the “ideal diode” circuit. .	97
6.13	Time domain peak detector output signal (top), comparator output signal (bottom) for first bit of information (bit 1).	98
6.14	Time-domain plots of positive and negative comparator waveforms and corresponding AND gate decision signal during start of fault (top) and end of fault (bottom).	100
6.15	Experimentally recorded time-domain piezo output overlapped with comparator outputs for case 2, fault AB-g condition.	101
6.16	Frequency spectrum of original PT output for fault AB-g, case 2 and PT output for no-fault condition, overlapped with output after being treated with HP and 1710Hz BP filter, simulated (top) and experimentally recorded (bottom). . . .	103
6.17	Output time-domain signals from the 1710Hz BP filter (top), peak detector output (second), comparator output for bit 4 (third), comparator output for bit 5 (bottom).	104
6.18	Simplified schematic diagram of two-level window comparator.	106
6.19	Frequency spectrum of simulated secondary current signals from <i>PSCAD</i>	107

List of Tables

2.1	Circuit parameters in PT electrical equivalent	25
4.1	Properties of PT type C-205 used in modelling	43
4.2	Effect of length of PT (l) on resonant frequency (f_R) and on low frequency output voltage	53
4.3	Specifications of PTs under test	54

List of Abbreviations, Symbols, and Nomenclature

NERC	North American Electric Reliability Corporation
ALR	Adequate Level of Reliability
AC	Alternate Current
DC	Direct Current
ADC	Analogue-to-Digital Converter
PT	Piezoelectric Transformer
CT	Current Transformer
VT	Voltage Transformer
MOV	Metal–Oxide Varistor
EMI	Electromagnetic Interference
FEM	Finite Element Modelling
IMC	Integrated Magnetic Concentrator
3D	Three Dimensional
2D	Two Dimensional
CCFL	Cold Cathode Fluorescent Lamp
PZT	Lead Zirconate Titanate
HB	Half–Bridge
ϵ	Dielectric Permittivity
d	Piezoelectric Charge Constant
s	Compliance
Y	Young’s Modulus
k	Electromechanical Coupling Coefficient
u	Displacement
ρ	Density of Material
v	Wave Propagation Velocity
MEMS	Microelectromechanical Systems
PSCAD	Power System Computer Aided Design
EMTDC	Electromagnetic Transients including DC
f_R	Resonant Frequency
L	Inductance
C	Capacitance
R	Resistance
Y	Admittance

B	Susceptance
mm	Millimetres
nm	Nanometres
SPICE	Simulation Program with Integrated Circuit Emphasis
c	Elasticity
e	Coupling Coefficient
VCVS	Voltage Controlled Voltage Source
CCCS	Current Controlled Current Source
CMRR	Common Mode Rejection Ratio
RTP	Real Time Playback
PC	Personal Computer
3Φ	Three Phase
IC	Integrated Circuit
BNC	Bayonet Neill–Concelman
PCB	Printed Circuit Board
T_C	Curie Temperature
LPF	Low Pass Filter
HPF	High Pass Filter
BPF	Band Pass Filter
GPS	Global Positioning System
Op–Amp	Operational Amplifier
SMD	Surface Mount Device
GMR	Giant Magnetoresistance
HV	High Voltage
CMOS	Complementary Metal Oxide Semiconductor
SOIC	Small–Outline Integrated Circuit
ESD	Electrostatic Discharge

Chapter 1

Introduction

This chapter introduces the background of the research documented in this thesis. An overview of a typical relay system, its evolution and the existing technologies driving this system are discussed here. The motivation behind the solutions explored in this thesis, scope of the work and finally the outline of this thesis follow in this chapter.

1.1 Overview

Relays have been used in the power industry for more than 100 years for purposes of disturbance detection in power systems and isolation of fault-causing component. The first relay installations made by companies like GE and ABB in early 1900s [1] were of electromechanical type, based on simple induction principles to provide protection to power systems. As an effort towards integration, this technology was then followed by the emergence of solid-state relays. These relays offered advantages like high speed, increased lifetime and high space efficiency over electromechanical relays. As solid-state relays appeared to have established in the protection area, digital-based relaying was first contemplated during the late 1960s. The idea that all the power system equipment in a substation could be protected using digital computers has ever since led to ongoing research in digital protection.

Microprocessor-based relays were first introduced in 1980s [2]. Since then, the rapid evo-

lution that microprocessor technologies underwent, encouraged the growth of these relays in power industry. Not only do microprocessor-based relays combine most of the functions of several components of electromechanical and solid-state relays, but also provide features like programmable logic, real-time metering and ability to communicate with processors of other relays, that were not available in the older technologies [3]. The main advantages that digital protection has over conventional methods are [4] listed below.

1. **Reliability** of a system depends on the following characteristics of a power system [5],
 - (a) Capacity to perform within acceptable limits during normal operation;
 - (b) Capacity to limit the scope and impact of failures if any;
 - (c) Ability to restore integrity promptly if lost;
 - (d) Ability to supply continuous power taking into account both scheduled and unscheduled outages.

Features like self-monitoring and built-in redundancy in digital relays ensure improved reliability. The NERC *2012 State of Reliability* report suggests a stable bulk power system reliability for the period 2008 to 2011. The advances in power system protection have ensured that the bulk power system is within the defined acceptable adequate level of reliability (ALR) conditions.

2. **Adaptability** of digital relays due to the fact that they are programmable and have an extensible design architecture, makes it possible to use the same relay for more than one function.
3. **Cost** involved in relay systems has substantially reduced due to advancement in integrated technology and high volume production. On the other hand, cost of conventional relays has continued to increase due to outdated technologies and high maintenance.
4. **Performance and other features** like post-fault analysis capabilities and increased accuracy in fault-location methods have no parallel in conventional technologies.

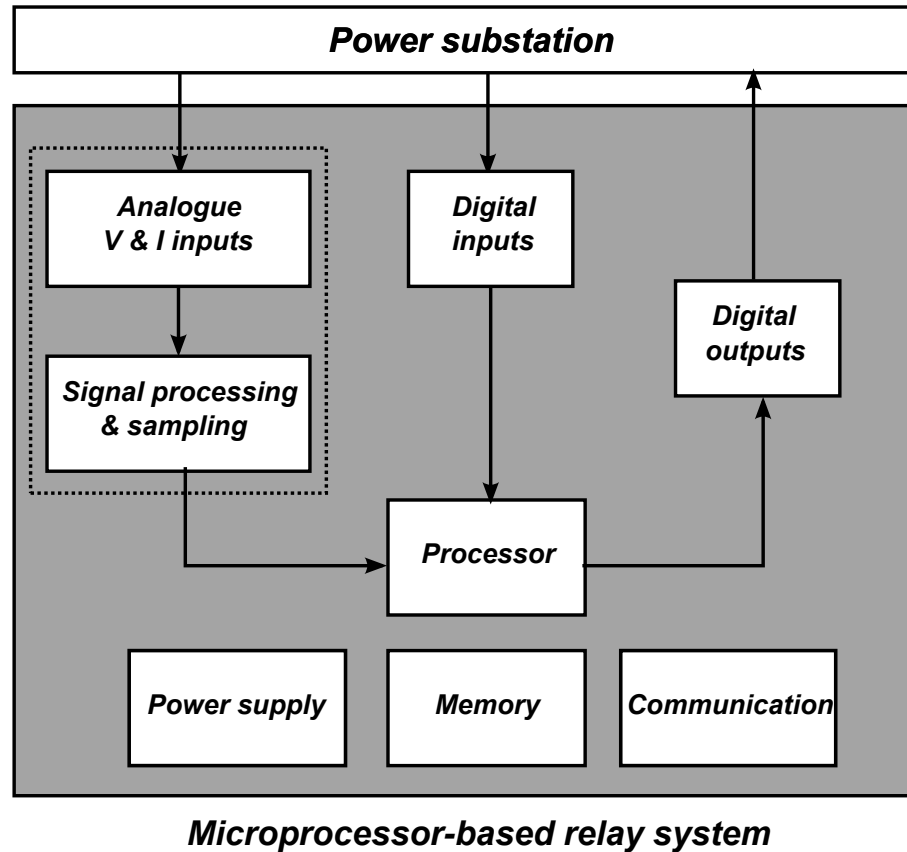


Figure 1.1: Block diagram of a typical microprocessor-based relay system used in power distribution substations.

A typical microprocessor-based relay system, Fig. 1.1, consists of sub-circuits that interface with the secondary signals in high-power application environment and convert high energy signals into low energy signals. The analogue sub-systems reduce the levels of input signals, these signals are then converted to digital signals after signal conditioning. These low energy isolated digital signals are then fed directly to processors and their peripherals. The relay algorithms process this acquired information and send digital commands for smooth operation of the entire system [3]. Even though well-established designs for sub-circuits that drive these relays exist, there is need for improved technology with respect to size, efficiency and reliability.

Apart from digital inputs to relay that indicate contact status, two main types of analogue inputs to the power relay hardware are AC voltage and AC current inputs. At the power system

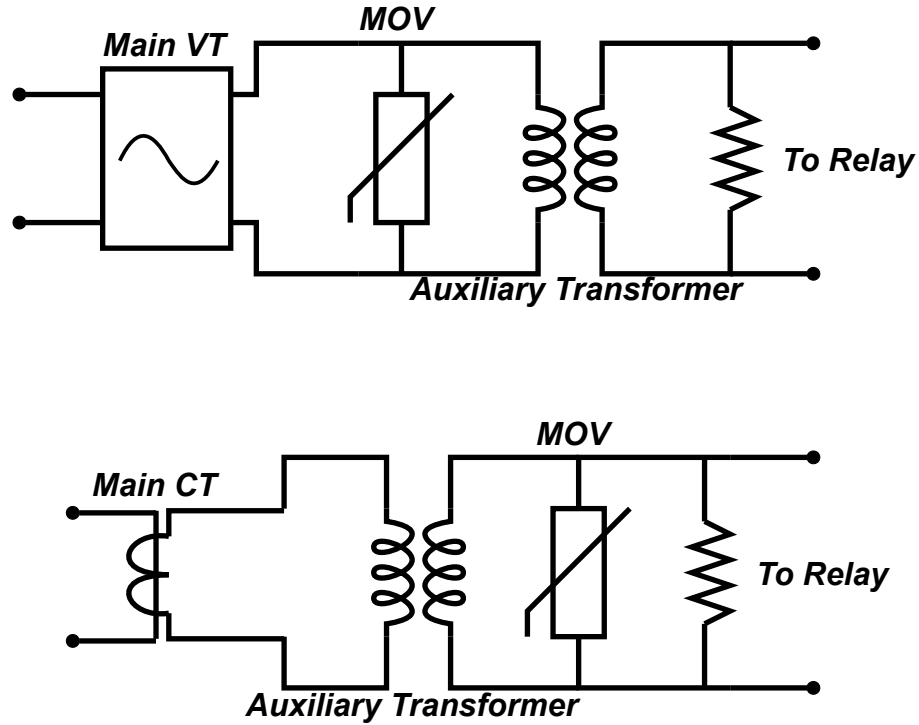


Figure 1.2: Simplified schematic diagram of voltage and current step-down techniques for input to relay; typical voltage transformation method (top), typical current transformation method (bottom).

level these signals are in the range of hundreds of kV and kA respectively. The levels of these signals are reduced by voltage and current transformers typically to 50/240V and 1/5A nominal values. The output of these instrument transformers are then applied to the analogue sub-circuit within the relay where all analogue inputs have to be converted to voltage signals suitable for conversion into digital form. This is done by the analogue-to-digital converter (ADC) whose input signal range is usually limited to a full scale value of $\pm 10\text{V}$. Hence the current and voltage signals obtained from current and voltage transformer secondary windings must be scaled accordingly [6].

Within this sub-system, auxiliary electromagnetic transformers are commonly used to transform 50/240V down to a workable voltage of 5/10V. Before applying the high input voltages to the auxiliary transformer, they are typically first treated with a metal-oxide varistor (MOV) [7], whose behaviour is modelled as a voltage dependent resistor with non-linear

voltage–current characteristics, used to protect circuits against excessive transient voltages. Figure 1.2 (top) shows a typical existing voltage transformation technique.

For metering purposes, current inputs must be converted to voltages, for example by resistive shunts. As the current transformer secondary may be as high as hundreds of amperes in normal operating conditions, shunts of resistance of few $\text{m}\Omega$ are needed to produce the desired level of input voltage for the ADCs. One alternative is to use an auxiliary current transformer. However, any inaccuracies in transformer would propagate and result in total error in the conversion process, which must be kept as low as possible. One advantage of using a transformer is that it provides electrical isolation between main CT secondary and digital computer system. After the step down of high AC currents to $1/5\text{A}$, the current is converted to a voltage for compatibility with the ADC. Figure 1.2 (bottom) shows a typical existing current transformation technique. These signals containing information about power line voltages and currents are then subjected to pre–filtering, sampling and finally to an ADC and the processing circuit.

Research has been done in areas of voltage and current metering and instrumentation on high power side of relay systems and on signal processing end of the system. Recently used technique which consists of a primary current sensing system based on an optically interrogated mechanism devised by GE, Global Research [8] allows for multiplexing of more than one monitoring channel.

Other innovations, such as monitoring system based on optical fibres in combination with a laser diode and photo–voltaic cell [9], have shown to be safe and reliable alternatives to metallic lines that transmit sensor signals.

In a typical power system, analogue current is periodically sampled and converted to digital data for analysis and to facilitate monitoring and detection of faults. In [10], the authors discuss an improved monitoring system which samples analogue signals at a rate higher than 128 samples per second, to capture those high–speed transients which cannot be detected by conventional sampling techniques.

Resistive current sensors, Rogowski coils based on Faraday’s law of induction, magnetic

field sensors, and current sensors based on Faraday's effect, are few of the principles established and implemented in commercial and industrial applications for current sensing [11, 12]. Optical current sensors are gaining high acceptance in power system applications, [13], due to their high accuracy, high bandwidth and inherent isolation property as compared to the above mentioned sensors. An electro-optic, hybrid current sensing technique which uses a combination of Rogowski coil and optical fibre cable in [14] presents a current measurement instrument for high-voltage power lines.

However, so far, to the best of our knowledge, there have been no reported alternatives suggested for electromagnetic transformer in low power side of relay system for voltage measurement and step-down. Similarly, in this particular area of application, there have been no suggested alternatives for current metering other than the conventional resistor based method.

1.2 Scope, objective and contributions of the thesis

The main objective of this work is to develop a method that may enable the replacement of existing sensing devices on the low power side of relay system, with alternatives that meet requirements of electrical isolation, accuracy, exact reproduction of the primary signal and least delay time as the signal travels from input to output. In our proposed methodology we use a piezoelectric transformer (PT) in its low frequency region of operation for voltage sensing and step-down and a Hall-effect based sensor for current sensing and metering.

The existing voltage sensing mechanism makes use of the conventional magnetic transformers in a board based design. These transformers consist of a winding, and considering the large number of analogue input subsystems that include these transformers, in a single substation, presence of these windings increases space occupancy and cost of manufacturing of the transformer. The magnetics of the transformer also leads to problems like electromagnetic interference (EMI) and potential short circuit hazards.

Use of PTs as an alternative to conventional magnetic transformers to achieve efficient

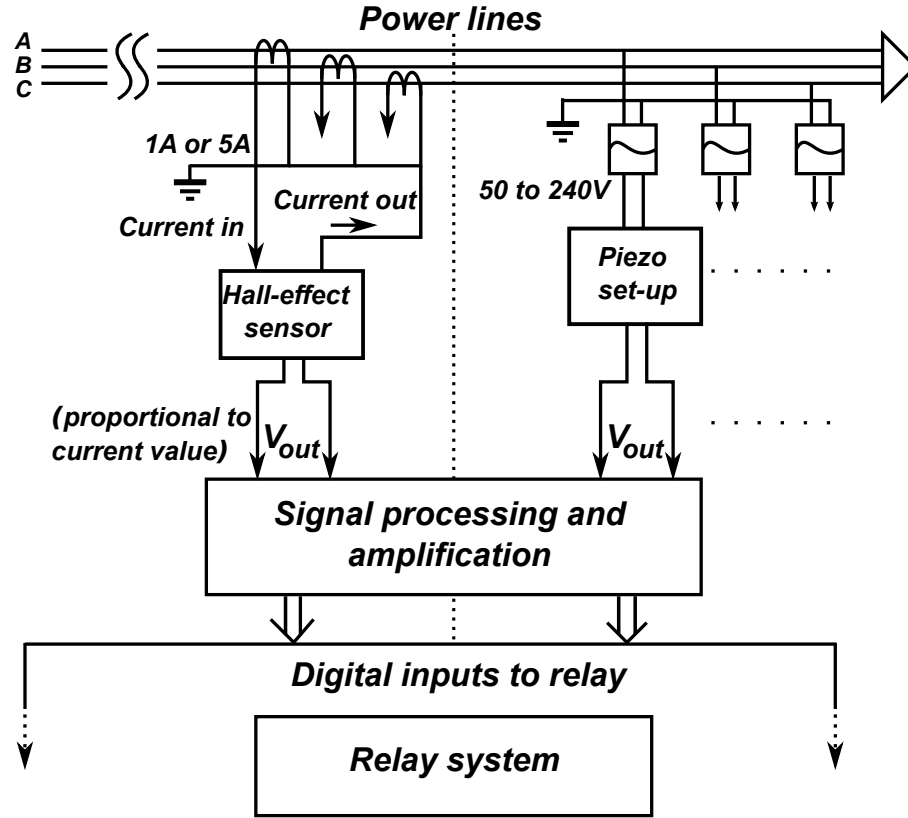


Figure 1.3: Block diagram of the proposed signal monitoring system.

and integrated electrical isolation has been explored since 1950s due to its advantages, e.g. low cost, high efficiency, high operating frequency, good input–output isolation [15], no EMI and no potential short–circuit fire hazard [16]. PTs have been typically used in cold cathode lamps, notebook computers, camera flash and some of the most compact high voltage sources. They exhibit high power density [17] and vibration frequency is the resonant frequency of piezoceramic block in 100kHz to 1MHz range. Reported applications of PT operating at its fundamental resonant frequency also include power converters [18] and gate–driver circuits [19]. A method to drive PT with a square waveform of frequency lower than the resonant frequency but which contains PT’s resonant harmonic is presented in [20]. However there are no reported applications of PT in its low frequency region of operation, neither have methods to drive PT directly with power–line frequency signals been discussed before.

In our initial experiments we used a commercially available piezoceramic transformer to

characterize its resonant and low-frequency behaviour. However, in order to develop a standardized voltage transformation system, a large number of PTs would be required to be analysed with respect to their size, physical and material properties, which was not practical in our study. Instead, finite element modelling (FEM) proves to be a very useful method for behavioural analysis in order to encompass a large sample set of PTs.

The other aspect of the objective is to propose a feasible alternative to replace the existing resistive current sensing methodology. The existing current metering in the analogue input subsystem is done by the transformer-resistor combination. Use of resistors to convert the current to a voltage leads to resistive losses and measurement errors. The growing need of a safe, isolated and low loss current detection technique has led to development of non-intrusive, non-resistive current sensing methods and devices [12]. Here, we explore the Hall-effect based current sensor based on the concept of integrated magnetic concentrator (IMC), to implement a resistor-free current sensing technique. A Hall-based sensor combines advantages of both, a transformer, by providing electrical isolation between high and low energy sides of a circuit and that of a resistor, by providing a robust and cheap way to convert the sensed current into a voltage equivalent. An analysis of a commercial current sensor supported by 3D modelling of the principle of integrated magnetic concentrator and Hall-effect shows a long-term potential to perform better than the shunt-based techniques currently used.

In the system proposed here, the scaled down voltage and current signals are passed through a signal processing system which consists of filters, peak detector circuit and comparator circuit, developed in order to detect the disturbance with minimum delay and help differentiate between the non-faulty and faulty signals. Finally, a combined sensing system which incorporates both voltage and current metering and signal processing sub-systems for all phases in a power system is proposed, Fig. 1.3.

1.3 Organization of the thesis

This thesis is structured in the following order:

In chapter 2, an overview of PT, its history and operational principle is discussed. The discussion then presents a mathematical analysis of direct and inverse piezoelectric effect. The electrical model is also briefly discussed in this chapter.

Chapter 3, gives an overview of the different methods used presently in industry and electronic applications for current sensing and metering. The concept of integrated magnetic concentrator is discussed and Hall-based commercial sensor used in our work is introduced.

Chapter 4 explains the modelling of PT in COMSOL based on the mathematical understanding of PT operation. This is followed by a discussion about PT eigen frequency analysis, frequency domain analysis and time domain analysis with simulation results. A section which presents results of all the experimental measurements carried out, the different PT configurations used, effect of load and high frequency transients and finally limitations involved in use of PT is also included in this chapter.

Chapter 5 discusses the nature of current inputs to relay system in normal and faulty conditions and presents a numerical model for Hall sensing principle. The simulated results are compared in trend with the actual measurements obtained from the commercial *Melexis* current sensor measurements.

In chapter 6, behavioural model of the decision making system developed for voltage and current sensing is presented with real-time inputs. A comparison between experimental and simulated results is shown to verify the truth table of the algorithm developed for fault detection and fault categorisation.

The research work is summarized in Chapter 7. The contributions are listed, and suggestions for future work are presented.

Chapter 2

Piezoelectric Transformer

‘Smart materials’ are structurally manipulated materials that have one or more of their properties significantly altered in a controlled manner, as compared to their original forms, to achieve a specific behaviour. This change is usually the result of an external stimuli in the form of stress, electric field, temperature, etc. [21]. Many such naturally existing and man-made materials are used to integrate functions like sensing, control and actuating by proper logic and design. Piezoelectric material is one such example of a smart material which produces a voltage on the application of stress and conversely, a voltage applied across the material causes a deformation. This reversible property has resulted in the wide use of piezoelectric materials in sensors and actuators.

The principle of piezoelectricity and direct piezoelectric effect was first demonstrated in the late 19th century by the Curie brothers. Later in the 20th century, piezoelectric devices were first used in practical applications like sonar. The early 1940s saw an intense search for man-made piezoelectric crystals suitable for electroacoustic transducers. Resonators of side-plated, end-plated and disk type were analysed for their dynamic piezoelectric properties in [22]. The expressions for impedances, operational frequencies and material constants were established for these resonators.

2.1 Piezoelectricity

Piezoelectricity is the interaction between electrical and mechanical systems. The direct piezoelectric effect causes electric charge to be produced as a result of mechanical stress, whereas the converse effect causes mechanical strain to be generated as a result of an applied electric field [23].

2.1.1 Basic principle

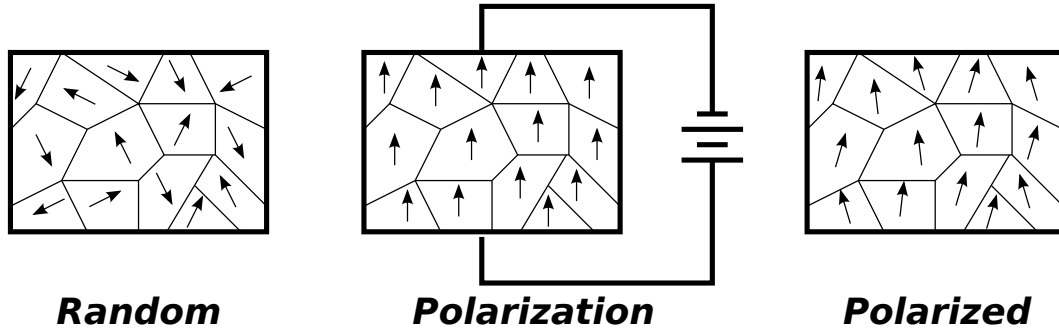


Figure 2.1: Polarization process to generate piezoelectric effect

Quartz, Rochelle salt, Topaz are a few examples of naturally occurring crystals that exhibit the piezoelectric effect. Apart from these, there are ferroelectric ceramic materials like lead zirconate titanate (PZT) that have been developed with improved piezoelectric properties. The polarization of dipoles in piezoelectric material affects the direction of the piezoelectric effect in the material. Prior to polarization, the dipoles are randomly directed, Fig. 2.1. When this piezoelectric material is heated above a ‘Curie’ temperature (T_C) under the application of a strong electric field, all dipoles are forced to align in the direction of polarization. The Curie temperature is the temperature at which intrinsic dipoles of a material change directions, and the material’s spontaneous electric polarization changes to induced electric polarization, or vice versa. The electric field applied E is related to polarization P of the material by ϵ_0 which

is permittivity of free space and electric displacement D ,

$$D = \varepsilon_0 \cdot E + P \quad (2.1)$$

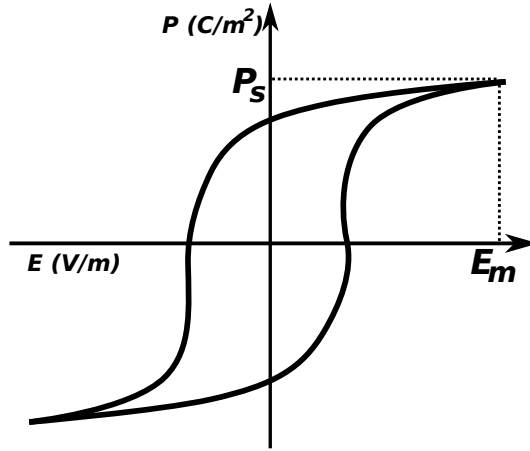


Figure 2.2: Plot of the dielectric hysteresis loop for a PZT material.

Beyond the maximum electric field E_m , the polarization reaches its saturation value P_s . After cooling, when the external field is reduced to zero, some dipoles switch back but most of the dipoles only become less strongly aligned, and do not return to their original alignment. Since there is still a very high degree of alignment, the polarization does not fall back to zero but to a lower value and the material now exhibits a remnant polarization. A further increase of electric field in the negative direction causes a new alignment of dipoles and saturation of polarization. This process repeats if the field is again increased in the positive direction towards zero and then to the positive threshold P_s , which closes the hysteresis curve, Fig. 2.2. The variation of electric displacement as a function of electric field follows very closely the curve for polarization [24]. The material can also be de-polarized when exposed to high temperatures or stress [25].

2.1.2 Properties and operating modes

The absence of centre of symmetry in a material is a required condition for the material to be piezoelectric in nature. Piezoelectric media are therefore intrinsically anisotropic. Piezoelec-

tricity provides a coupling between elastic and dielectric phenomena and hence the properties are always discussed with reference to the elastic and dielectric constants. For any direction of propagation of waves through piezo there are three possible acoustic waves with mutually perpendicular vibration directions but with different velocities. The wave equations for most general cases of longitudinal or shear propagating waves were established in [26]. In addition to the non-linear effects in these ceramics due to mechanical and electrical stimulus, the long-term properties of several piezoelectric ceramic compositions as functions of temperature and time were evaluated in [26].

Based on the excitation frequency applied to the ceramic, a bending pattern is observed in the ceramic body. The type of bending or displacement pattern is referred to as the vibration mode [27]. Modes of vibration of most solid bodies are due to existence of a system of standing waves; these vibration modes are therefore analytically derived from the wave equation. The shape of the ceramic and the desired vibration mode are interdependent. This basic shape of the piezo body, in addition to the polarization direction and direction of applied electric field, give rise to the different vibration modes: lumped mode, length vibration mode, thickness mode, radial and contour modes. Depending on the type of mode, wave equations are modified to represent piezo resonant behaviour.

A simple and commonly used method to describe both electrical and mechanical properties of a piezo body is use of their electrical equivalents. Hence specific electrical circuits are established for these vibration modes, [26]. A number of significant theoretical results were obtained to explain the macroscopic behaviour of piezoelectric devices, such as the Lagrangian and Green's function formulations of piezoelectricity. These concepts provide a clear understanding of piezoelectric phenomenon [28] and boosts developments in the actual hardware.

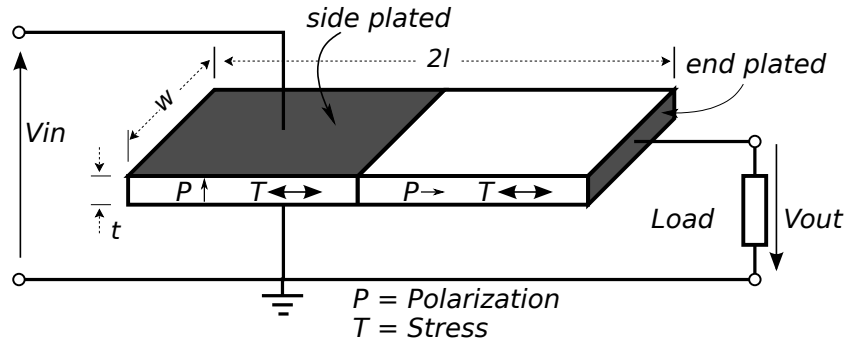


Figure 2.3: Simplified diagram showing geometry of a typical Rosen type piezoelectric transformer.

2.2 Piezoelectric transformers

A PT is an assembly of two piezoelectric elements forming an actuator–sensor combination that has an operation based on the principle of electromechanical conversion of energy. Piezotransformers are most suited for high voltage step–up transformation applications and the transformation ratio is approximately proportional to the ratio of PT thickness to PT length. This type of PT is usually found in applications like notebook back–light sources, high voltage lamps and cold cathode fluorescent lamps (CCFL) [29].

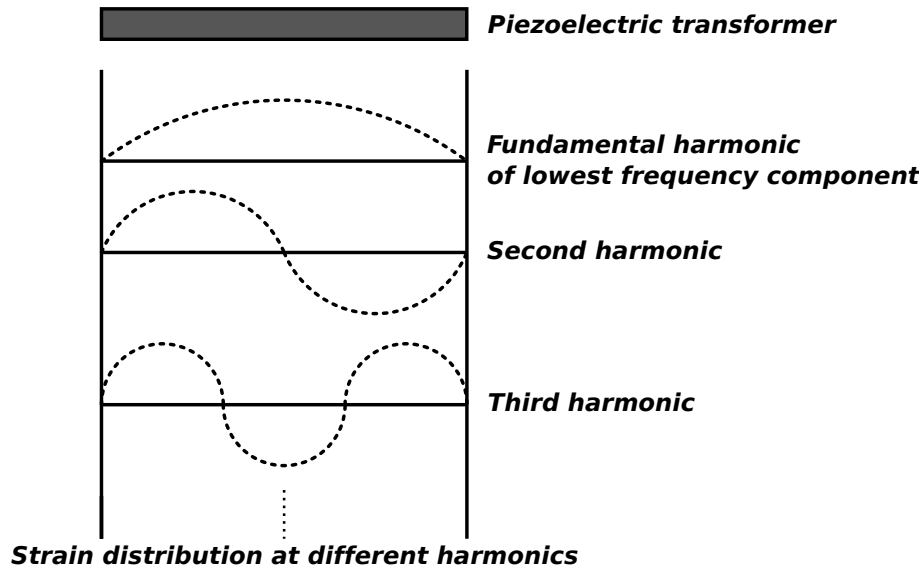


Figure 2.4: Plot of the first three fundamental harmonics inside a piezo element.

The “Rosen piezoelectric transformer”, a passive electrical energy–transfer device or trans-

ducer employing piezoelectric properties of a material to achieve transformation of voltage or current or impedance, was first introduced in [30]. This patent also illustrated a PT with a configuration to attain high voltage transformation ratios with the piezoelectric member having two regions of polarization, transverse and longitudinal, Fig. 2.3.

A sinusoidal input voltage applied at primary electrode creates an alternating stress in piezo and the material starts to vibrate with a frequency equal to the applied frequency. The strain distribution within the piezo body varies with the harmonics of the frequency used for excitation, Fig. 2.4. The mechanical vibration travels through the material, which causes the secondary part of the transducer to vibrate. In turn, these vibrations induce electrically isolated alternating voltage at the secondary electrode [31, 23], Fig. 2.3.

2.2.1 Types and configurations of PTs

Over the past twenty years, modifications have been done in PT designs with respect to their vibration modes. They are commonly classified into three main types, Rosen-type PT, thickness vibration mode PT and radial vibration mode PT. In Rosen-type PT, Fig. 2.3, the poling directions of actuator and sensor portions are orthogonal to each other [32]. The longitudinal vibrations are mechanically coupled to the secondary half of the PT, and induce a potential difference.

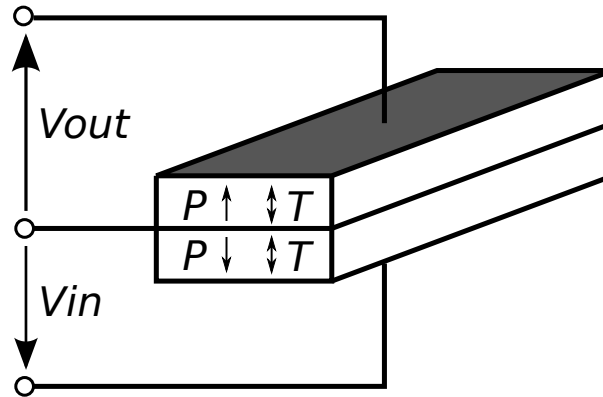


Figure 2.5: Thickness vibration mode PT

In the thickness vibration mode PT, similar to operation of the Rosen type transformer,

the electric field applied in the actuator section of the thickness vibration mode PT, Fig. 2.5, is parallel to the direction of poling. However, in this type, the latitudinal vibration mode is resonant, rather than a longitudinal vibration mode. Due to its inherent low voltage gain, this PT is also referred to as the low voltage PT, and is mainly used in DC/DC converters [33].

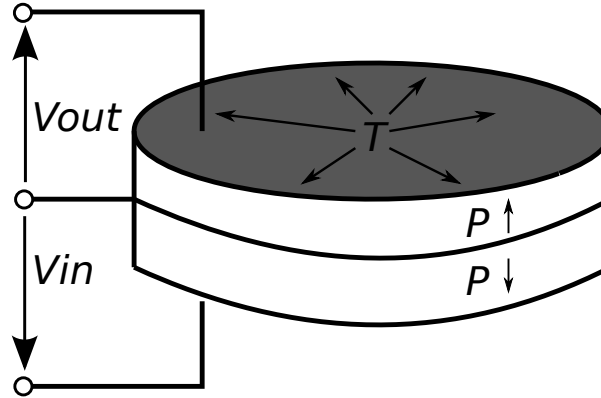


Figure 2.6: Radial vibration mode PT

The radial mode PT, Fig. 2.6, is poled in the thickness direction. Excitation of the primary section generates longitudinal (i.e. radial) vibrations throughout the device which generate a secondary voltage. The primary and secondary sections of radial PTs may consist of a number of layers to achieve the desired transformation characteristic as per the application. As compared to Rosen PTs, these PTs have a higher electromechanical coupling factor and hence they are used in applications like Transoners that employ multi-stacked radial PTs [33].

2.2.2 Application specific PT structures

Over time, various configurations and structures suitable for specific applications have been suggested and implemented, for example a structure that operates in second thickness extensional vibration mode applied to a 2MHz switch mode power supply, [18]. This mode is preferred over a Rosen type piezoelectric transformer which is unsuitable for power transmission, because of the high internal impedance, due to low frequency driving. Parallel PT combination exhibits higher step-up ratios and efficiency as compared to single PT. Multilayer unipolar PTs serve the common purpose for several PTs connected in parallel [34].

One instance of modular topology of PTs with an incorporation of a symmetrical double input layer in PT's design enabled simultaneous achievement of both high power and high voltage for space communications applications [35]. Energy harvesting application of PT in the form of a micro-transformer processed on a SOI wafer intended to supply micro-systems that require a very low amount of energy is demonstrated in [36], while piezoelectric MEMS generator comprising of a silicon wafer with laminated lead zirconate titanate (PZT) material and inter-digital electrodes is presented in [37].

Performance of a PT strongly depends on how its input is driven. Driving alternatives based on half-bridge (HB) topology and the input matching network using series and parallel inductor connections help obtain PT's optimum performance. These techniques allow driving PT sinusoidally or by use of soft-square voltage [38]. A sub-harmonic driving technique which involves application of a voltage to PT whose fundamental frequency contains its resonant harmonic at which energy transfer takes place is discussed in [20].

2.3 Electrical Representation

The electrical and mechanical behaviour of PT principally is represented by equivalent electrical circuits. The equivalent circuit for a piezoelectric resonator without consideration of mechanical losses and boundary conditions was first developed by Mason [39]. Representing PT with its non-linear behaviour with a strong dependence on factors like electric field, stress, temperature, external vibrations, etc. is complex. Several studies that deal with aspects like continuity of displacement and stress at the junction [40], maximum power transfer [16] and optimized efficiency [41] have been done. The different forms of PT in terms of their vibration modes and shapes and structures exhibit different electromechanical and resonant characteristics. There have been equivalent electrical circuit analyses that represent these vibration modes [42] and different PT configurations like multi-layer PTs which use circuit oriented simulation programs such as SPICE [43].

2.3.1 Mathematical modelling

In order to understand the process of modelling of PT, it is important to have knowledge about certain basic field and material properties of PT in general. For a PT, stress (T), strain (S), electric field (E) and electric displacement (D) are related to each other by dielectric permittivity (ϵ), piezoelectric charge constant (d) and compliance (s) [27, 44].

Here,

T – Applied force per cross-sectional area;

S – Ratio of change in dimension to original dimension;

E – Electric field strength;

D – Electric displacement;

ϵ – Permittivity;

d – Polarization generated per unit mechanical stress applied or, alternatively, is the mechanical strain per unit electric field applied;

s – Strain produced per unit stress applied.

The inverse of compliance is referred to as Young's Modulus (Y),

$$Y^E = \frac{1}{s^E} \quad (2.2)$$

where the superscript E denotes constant electric field.

The most significant parameter in the working of a PT, the electromechanical coupling coefficient (k), is the measure of ability of a piezoelectric material to transform electrical energy into mechanical energy and vice versa. It is evaluated based on energy cycle within the piezo to compute the effective energy conversion from mechanical form to electrical form and vice-versa [45]. One possible explanation can be demonstrated as follows:

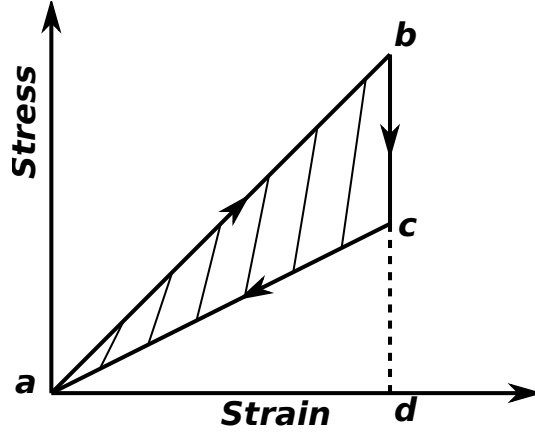


Figure 2.7: Stress–strain cycle that defines electromechanical coupling coefficient.

The piezo body, with no electrical connection, is first mechanically stressed, (Fig. 2.7 $a \rightarrow b$), storing both mechanical and electrical energies in the body ($\triangle abd$). The electrode surfaces are then held to restrain the deformation in the body and part of the energy stored in the body is allowed to dissipate through a load (e.g. resistance) connected between these electrodes, ($b \rightarrow c$ in Fig. 2.7). Finally, when all electrical energy is dissipated, ($\triangle abc$), the piezoelectric body is short-circuited so that it deforms back to its original shape, ($c \rightarrow a$ in Fig. 2.7), indicating mechanical work, ($\triangle acd$ in Fig. 2.7). A similar energy conversion analysis can be performed in the other direction in case of electrical driving and measurement of part of energy converted into mechanical work.

The electromechanical coupling coefficient is therefore represented as,

$$\sqrt{\frac{\text{Electrical energy}}{\text{Driving mechanical energy}}} \quad \text{or} \quad \sqrt{\frac{\text{Mechanical energy}}{\text{Driving electrical energy}}} \quad (2.3)$$

This coefficient depends on the vibration mode and is also expressed in terms of material properties and other piezoelectric constants as,

$$k = \frac{d}{\sqrt{s^E \cdot \epsilon^T}} \quad (2.4)$$

Behaviour of a piezoelectric ceramic is governed by combination of electrical behaviour of

the material, phenomenon of piezoelectricity and Hooke's law.

$$D = \varepsilon^T \cdot E \quad S = d \cdot E \quad S = s^E \cdot T \quad (2.5)$$

The poling direction in the piezo ceramic by convention defines the z axis of a three-dimensional orthogonal axis system. If numbers 1, 2 and 3 correspond to x , y and z axes respectively, then 4, 5 and 6 represent the directions of shear stress about the 1, 2 and 3 directions respectively. Based on the convention defined in [46], and if the first subscript refers to direction of electric field and the second subscript refers to direction of mechanical stress or strain, the tensor representation of phenomenon of piezoelectricity is given by,

$$\begin{bmatrix} S_1 \\ S_2 \\ S_3 \\ S_4 \\ S_5 \\ S_6 \end{bmatrix} = \begin{bmatrix} d_{11} & d_{21} & d_{31} \\ d_{12} & d_{22} & d_{32} \\ d_{13} & d_{23} & d_{33} \\ d_{14} & d_{24} & d_{34} \\ d_{15} & d_{25} & d_{35} \\ d_{16} & d_{26} & d_{36} \end{bmatrix} \begin{bmatrix} E_1 \\ E_2 \\ E_3 \end{bmatrix} \quad (2.6)$$

or

$$S_j = \sum d_{ij} E_i \quad \text{where } i = 1, 2, 3 \text{ and } j = 1, 2, \dots, 6. \quad (2.7)$$

Similarly Hooke's law in its tensor form for a constant electric field can be written as,

$$S_j = \sum s_{jk}^E T_k \quad \text{where } j = k = 1, 2, \dots, 6. \quad (2.8)$$

Similarly, a relationship exists for the electric displacement D as a function of E and T and for a rectangular PT, the general form of equations that depicts its combined electromechanical behaviour is written as,

$$S_j = \sum s_{jk}^E T_k + \sum d_{ij} E_i \quad (2.9)$$

where $i = 1, 2, 3$ and $j = k = 1, 2, \dots, 6$.

$$D_j = \sum d_{ij}^E T_j + \sum \varepsilon_{il}^T E_l \quad (2.10)$$

where, $i = l = 1, 2, 3$ and $j = 1, 2, \dots, 6$.

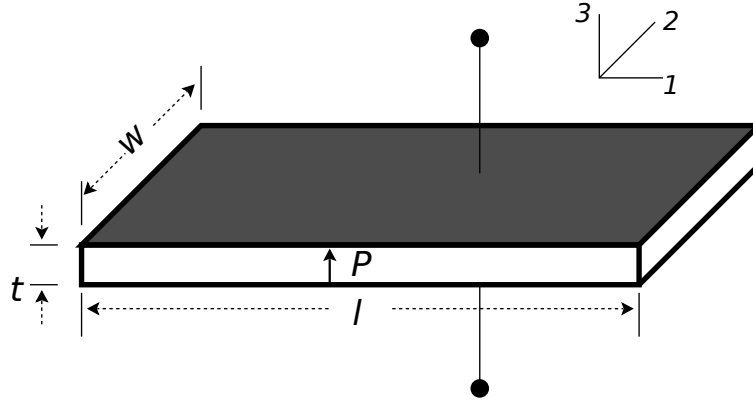


Figure 2.8: Input part of Rosen PT vibrating in thickness mode.

As PT is made of two differently polarized resonators, models are first developed individually and then analysed by combining these sections.

The input half of the PT in the thickness vibration mode is as shown in Fig. 2.8.

Since the bar is polarized in direction 3, the vibration is given by Newton's law as in (2.11), where u is the measure for displacement and ρ is the density of the crystal.

$$\rho \frac{\partial^2 u_1}{\partial t^2} = \frac{\partial T_1}{\partial x} + \frac{\partial T_2}{\partial y} + \frac{\partial T_3}{\partial z} \quad (2.11)$$

Considering electric field is applied in direction 3 and with zero stress in the lateral direction, the equations for S and D are,

$$S_1 = s_{11}^E \cdot T_1 + d_{31} \cdot E_3 \quad D_3 = d_{31} \cdot T_1 + \varepsilon_{33}^T \cdot E_3 \quad (2.12)$$

Expressing T_1 in terms of E_3 and S_1 and differentiating with respect to x gives (2.13), since electric field is constant,

$$\frac{\partial T_1}{\partial x} = \frac{1}{s_{11}^E} \frac{\partial S_1}{\partial x} \quad (2.13)$$

Considering strain as the measure of displacement in the x direction, (2.11) becomes,

$$\frac{\partial^2 u_1}{\partial x^2} - \rho s_{11}^E \frac{\partial^2 u_1}{\partial t^2} = 0 \quad (2.14)$$

Velocity v of the propagating wave in the piezoelectric medium is expressed as,

$$v^2 = \frac{1}{\rho s_{11}^E} \quad (2.15)$$

The variation of u , with time is written in phasor form as,

$$u_1 = \tilde{u}_1 e^{j\omega t} \quad (2.16)$$

Using (2.15) and (2.16), the displacement equation in x (2.14) can be written as,

$$\frac{\partial^2 \tilde{u}_1}{\partial x^2} - \frac{\omega^2}{v^2} \tilde{u}_1 = 0 \quad (2.17)$$

The solution of (2.17) with two arbitrary boundary conditions is,

$$\tilde{u}_1 = A \cos \frac{\omega x}{v} + B \sin \frac{\omega x}{v} \quad (2.18)$$

The constants A and B can be determined by differentiating (2.18) with respect to x and by using the boundary condition at $x = 0$ and $x = l$, stress $T_1 = 0$.

$$\frac{\omega}{v} B = d_{31} E_3 \quad \frac{\omega}{v} = \gamma \quad A = \frac{d_{31} E_3}{\gamma} \left[-\frac{1}{\sin \gamma l} + \frac{1}{\tan \gamma l} \right] \quad (2.19)$$

Therefore,

$$S_1 = d_{31}E_3 \left[\frac{\sin \gamma x}{\sin \gamma l} - \frac{\sin \gamma x}{\tan \gamma l} + \cos \gamma x \right] \quad (2.20)$$

Hence the strain in the piezo material depends on d , E , l , ω , ν and the dynamic value of x .

The admittance and impedance of the PT plays an important role in determining the resonant frequency for that PT. The current in the piezoelectric device is the rate of change of the surface charge with respect to time and is given by,

$$I = j\omega \iint D_3 dS \quad (2.21)$$

Therefore from (2.12), (2.20) and integrating over the length l ,

$$I = j\omega l \left[\epsilon_{33}^T - \frac{d_{31}^2}{s_{11}^E} + \frac{d_{31}^2}{s_{11}^E} \left(\frac{\tan \gamma \frac{l}{2}}{\gamma \frac{l}{2}} \right) \right] E_3 \quad (2.22)$$

Let $\epsilon_{33}^{LS} = \epsilon_{33}^T - \frac{d_{31}^2}{s_{11}^E}$. The admittance of the crystal is therefore,

$$Y = \frac{I}{V} = \frac{I}{E_3 l} = \frac{j\omega l \epsilon_{33}^{LS}}{t} \left[1 + \frac{d_{31}^2}{s_{11}^E \epsilon_{33}^{LS}} \left(\frac{\tan \gamma \frac{l}{2}}{\gamma \frac{l}{2}} \right) \right] \quad (2.23)$$

At resonant frequency, the admittance is infinite; i.e. with reference to (2.23), if $\tan \gamma \frac{l}{2} = \infty$ or $\gamma \frac{l}{2} = \frac{\omega}{\nu} \frac{l}{2} = \frac{n\pi}{2}$ where $n = 2m - 1$ and $m = 1, 2, \dots$. Hence the resonant frequency is given by,

$$f_R = \frac{n}{2l \sqrt{\rho s_{11}^E}} \quad (2.24)$$

At very low frequencies, admittance in (2.23) reduces to the capacitance,

$$\frac{j\omega l}{t} \left[\epsilon_{33}^{LS} + \frac{d_{31}^2}{s_{11}^E} \right] = \frac{j\omega l \epsilon_{33}^T}{t} = j\omega C \quad (2.25)$$

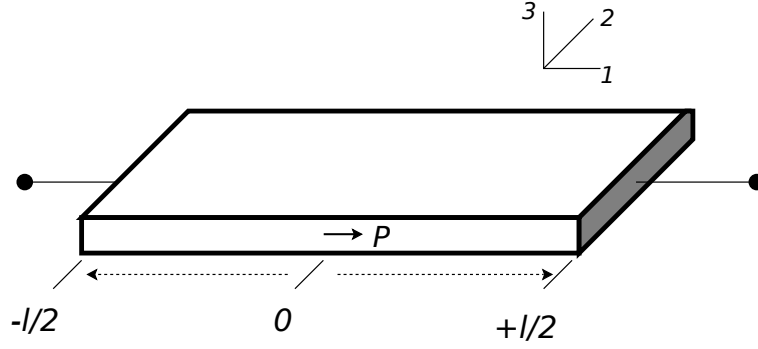


Figure 2.9: Output part of the Rosen PT vibrating in the longitudinal mode

And hence the capacitance is computed as,

$$C = \frac{wl}{t} \epsilon_{33}^T \quad (2.26)$$

When the capacitance is substituted in the admittance equation (2.23) and expanded further by partial fraction method, it represents piezoelectric impedance expressed in the form of a number of LC_n series circuits connected in parallel. This forms the basis of electrical equivalent of piezoelectric function. From the capacitances, inductance values for the electrical PT model are also computed. If an external mechanical variable is included in the analysis, it results in new impedance values. Mechanical losses are also incorporated in terms of an equivalent resistance R .

Analysis of the longitudinal vibration mode is similar to that of thickness vibration mode with different boundary conditions, Fig. 2.9, where electric field is along the length of the bar and the wave is assumed to propagate along the length axis with zero stress in the lateral direction. The PT as a whole is analysed by combining the individual sections, which applies to sectional PTs, circular disc type PTs (based on cylindrical co-ordinate system), multi-layered PTs, etc.

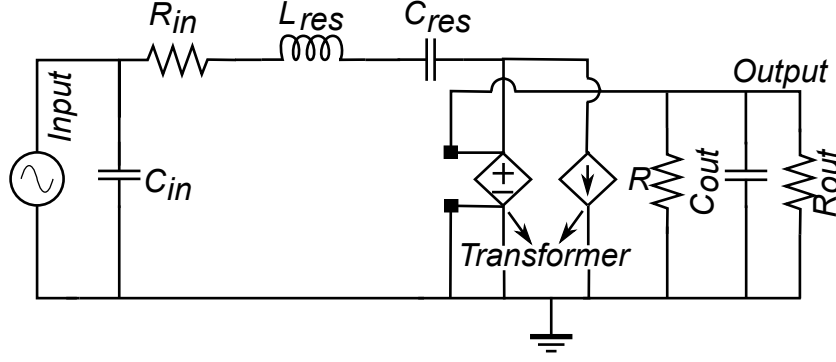


Figure 2.10: Simplified schematic diagram of electrical model of PT

2.3.2 Electrical equivalent model

Simplified approach of finding the electrical equivalent model of a PT that incorporates the operational conditions, results in a general equivalent circuit which operates around one of its mechanical resonant frequencies. For example, a model that assumes a specific bandwidth and a narrow load range is discussed in this work, [18].

Table 2.1: Circuit parameters in PT electrical equivalent

Parameter	Value
Input signal	5V, 162.5kHz
Gain	1V/V
C_{in}	210pF
R_{in}	50 Ω
L_{res}	3mH
C_{res}	319pF
R	980k Ω
C_{out}	4.16pF
R_{out}	1k Ω

In order to enable design of the supporting electronics, and to be able to simulate PT's behaviour under various operating conditions within the supporting electronics, we developed this equivalent circuit model, Fig. 2.10 in SPICE. With this electrical model, we verified earlier findings reported in [47], and also evaluated deviations in model behaviour in the low-frequency region of operation. In this model, the arm containing resistance, inductance and capacitance in series represents the mechanical behaviour of PT. L_{res} and C_{res} are series equiv-

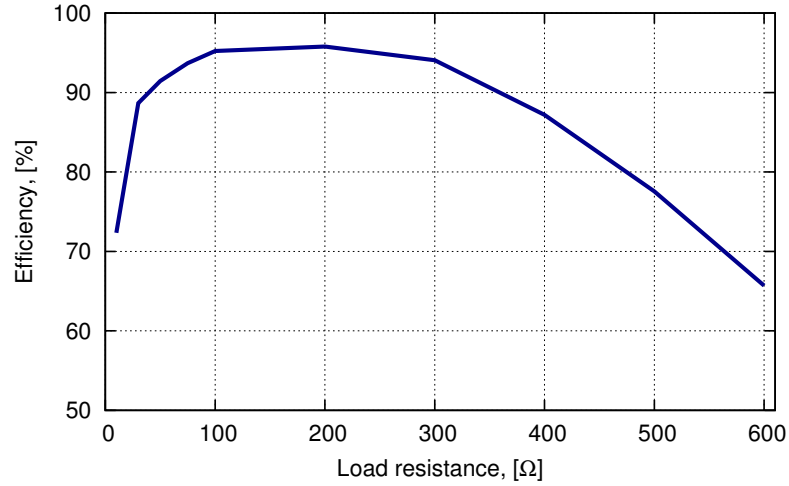


Figure 2.11: Simulated efficiency plot at resonance for varying load in electrical model.

alent inductance and capacitance respectively and R_{in} is the equivalent mechanical resistance. C_{in} and C_{out} are the input and output capacitances while R_{out} is the load resistance, Table 2.1. The transformer in conventional circuit equivalent is replaced by a combination of voltage controlled voltage source (VCVS) and current controlled current source (CCCS). One advantage of this transformer representation in the schematic apart from not having to design an electromagnetic transformer with accurate windings, is that it works well even for DC input waveforms. The electromagnetic transformer windings would act as a short circuit to DC voltage [41].

The equivalent circuit simulates successfully with an efficiency of over 90% in resonant frequency range. Figure 2.11 shows the efficiency observed at resonance for varying load in the electrical model. As input (and hence resonant) frequency decreases, the circuit consumes more power and efficiency drops. Circuit behaviour also deviates when it is driven at any frequency other than resonant frequency. The piezo circuit therefore cannot be mapped into an actual design unless frequency of operation is large. Voltage and frequency characteristics in different load conditions, at half and full wavelength resonant frequencies, are based on analysis discussed in [48].

2.4 Summary

The concept of piezoelectricity, crystalline structure of natural and man-made piezo materials and the physics behind the direct and inverse piezoelectric effect is discussed in this chapter. This physical principle forms the basis of a piezoelectric transformer. The first form of transformer, the ‘Rosen PT’, is introduced with details about the operational fundamentals of this energy-transfer device. Various modes of operation, size and structures of piezo transformers formed by variational poling methods and electrode configurations are discussed briefly in this section.

The general field and material PT properties are discussed and relations between them are established. These parameters help understand the work-energy flow within the PT body and their effect on the resultant output potential. Depending on the piezo properties and specific poling conventions, a generalised set of equations depicting the sensor and the actuator portion of PT is arrived at. Based on these equations, the corresponding admittances are evaluated which can be compared to an *LC* network. Using *R* as an equivalent to mechanical losses in the PT body, the basic analytical model which represents the electromechanical behaviour of PT in form of an equivalent electrical circuit, is derived. This model is simple and easy to synthesize different behavioural patterns. However, to take into consideration the effect of factors such as stress, temperature, mechanical disturbances, electrode shapes, positions etc., finite element modelling techniques are used for an all round understanding of PT devices.

Chapter 3

Current sensor

In this chapter, we review some of the current sensing techniques used commercially. We discuss different underlying physical principles that form the basis for current sensing and we specifically elaborate on magnetic sensing. Hall-effect which forms the basis of the commercial sensor we propose is reviewed in detail. Supporting simulated and experimental results obtained using this sensor follow in the next chapters.

3.1 Current Sensing Techniques

Development of current sensing techniques for a wide variety of electrical and electronics applications has evolved based on the requirements of the application. The current information obtained is then made available in a digital form to the processor for control or monitoring purposes. At first, physical effects directly associated with flowing current were used for current measurement. This direct measurement method became inefficient with increasing magnitudes of measurable current. In the 19th century, the first transducer in the form of a galvanometer using the magnetic field induced by flowing current was introduced [49]. In the following years improvements were made to deal with effects of temperature, stray magnetic field, AC and DC components etc. on measured current.

Current sensing techniques can be classified based on their underlying fundamental physi-

cal principle. Broadly they are considered to be [11],

1. Ohm's law of resistance;
2. Faraday's law of induction and sensing of static magnetic fields;
3. Faraday's effect or optical current sensing.

3.1.1 Resistive current sensing

This technique is based on Ohm's law that states, current through a conductor is directly proportional to the potential drop across its resistance.

$$J = \sigma \cdot E \quad (3.1)$$

where J is the current density in a resistive material, E is the electric field and σ is the material dependent parameter called conductivity.

Use of a **shunt resistor** is one of the conventional and easier ways of current measurement. This method can be used to measure both AC and DC currents. Since a resistor is introduced in the current carrying path, this method incurs a power loss and reduces efficiency. Coaxial shunts have an intrinsic inductance which limits accuracy and bandwidth [50]. To avoid losses and to increase power efficiency, **MOSFETs** which are ohmic when biased in the non-saturated region can be used by sensing voltage across its drain and source. But this technique has low accuracy due to the inherent non-linearity of MOSFET's ohmic operation [51].

To increase integrability, more advanced techniques like **Surface Mount Device (SMD) shunt resistor** are commonly used. But the smaller size results in a substantial parasitic inductance. One another modified method is to use **trace resistive sensing** which uses the intrinsic resistance of the conducting element like a copper trace or busbar [11]. However, in these methods there is a need for hardware for signal isolation due to the unavoidable electrical connection between the current to be measured and the sensing circuit, and most times there is also

a need for transmission and amplification circuits.

3.1.2 Magnetic current sensing

This technique is based on Faraday's law of induction which is a quantitative relationship between variable magnetic field and the electric field created by the change. The Maxwell–Faraday equation is a generalisation of Faraday's law stated in its differential form as,

$$\nabla \times E = -\frac{\partial B}{\partial t} \quad (3.2)$$

where $\nabla \times$ is the curl operator, E is the electric field and B is the magnetic field.

Current transformer, based on the classical transformer principle, which couples a secondary coil to the variable flux created by the primary currents, is widely used. These transformers are robust and used for isolating and stepping down a larger primary alternating current to a secondary current that can easily be measured with a shunt. This technique provides electrical isolation, consumes low power, requires no additional driving circuits and the output voltage does not need any further amplification. They are commonly used in power system applications because of their low cost, and the ability to provide an output signal that is directly compatible with an ADC. This transformer however is not easily integrable and cannot transmit the DC portion of current. Other issues like core saturation, ageing and hysteresis of material affect the accuracy of measurement.

Rogowski coil is an air-cored coil transducer which is free from shortcomings introduced by the core magnetic material and is insensitive to external magnetic perturbations. The coil is uniformly wound on a non-magnetic core material which is placed around the current carrying conductor and the voltage induced in the coil is proportional to the rate of change of current in the conductor. The output of the Rogowski coil is then usually connected to an electrical integrator circuit to provide an output signal that is proportional to the current. Rogowski coils are inexpensive, simple and non-invasive. It does not exhibit saturation, is inherently

linear and can be integrated onto a PCB. However, the sensitivity of Rogowski coil is weak as compared to current transformer. It requires an additional integrator circuit and hence an external power source. Offset in the coil position can cause large measurement errors resulting in poor reliability and inaccuracies [11, 50].

Faraday's law takes into consideration only varying magnetic fields and hence cannot be used to measure static fields. Magnetic field sensors sense both static and dynamic fields around the current carrying conductor by measuring their transverse and longitudinal components. They are operated in both, open loop configuration, where the sensor is placed in vicinity of the conductor, or closed loop configuration where the output voltage is fed back to the measuring circuit for error compensation. The most commonly used sensor in this category is the **Hall effect sensor**. The working principle of this sensor will be detailed in the following section.

Sensors based on the **Fluxgate** technology are one of the most accurate sensors. These sensors utilize the non-linear relation between the magnetic field, and magnetic flux density within a magnetic material. For instance, it employs a 'saturable inductor', value of which depends on the permeability of the core [50].

GMR current sensors are based on the Giant Magnetoresistive (GMR) effect which is the effect of magnetic field on electrical resistance. Today, many commercial magnetic sensors based on these principles are used in a wide variety of applications [52, 53, 54]. Due to high sensitivity of these sensors to the magnetic field, they can be effectively used to sense the current by measurement of the magnetic field generated by the current. These sensors are cost-effective and can easily be mass-produced using semiconductor technology. However, the main issues associated with these sensors are distinct thermal drift and high non-linearity.

3.1.3 Optical current sensing

Optical sensors are based on Faraday's effect which is a magneto-optical phenomenon that relates light polarization and magnetic field in a medium. The Faraday effect causes a rotation of the plane of polarization of a light beam in an optical material, under the influence of a

magnetic field generated by the electrical current to be measured [55]. For an optical material, where the optical path forms a closed loop, the rotation of plane of polarization (θ) is given by,

$$\theta = \mathcal{V} \oint \vec{H} \cdot d\vec{l} \quad (3.3)$$

where \mathcal{V} is the Verdet constant, H is the magnetic field and l is the interaction length.

In a **basic polarimeter detection method**, light is fed to a fibre optic coil around the current carrying conductor. The detection circuit consists of a 45° polarizer with respect to original polarization direction so that the output light intensity (I_{out}) is proportional to the input light intensity (I_{in}) [11] by,

$$I_{out} = \frac{I_{in}}{2}(1 + \sin 2\theta) \quad (3.4)$$

The use of fibre optic eliminates effect of stray magnetic fields and makes the system independent of position of current carrying conductor within the fibre optic coil which makes it more accurate. Advancements in this basic method have been done with respect to better stability, increased measurement range and sensitivity. But the sensitivity increases at the cost of increased thermal drift. The optical installations are expensive and parameters like the bending stress within the fibre may deteriorate its performance with time.

Certain modern cost-effective designs combine two or more current sensing principles. For example, [56] describes an optically powered current measurement system that involves a hybrid two-stage current transformer optically isolated for operation under HV conditions by connection of the HV module and ground module by a fibre optic link. Another such sensor discussed in [57], utilizes advantages of both electronic and optical technologies. It involves a low power consumption electro-optic hybrid instrument which measures not just current, but frequency, phase differences and temperature.

3.2 Hall-effect based current sensing

In our problem definition, an auxiliary transformer is used at the secondary of CT in power systems to transform the current values to standard relay rated values. During fault times when the secondary current becomes large and may contain high frequency components, use of a shunt could result in increased losses and high inefficiency. Techniques have been proposed to increase the overall efficiency of the transformer-resistor combination by use of an active load at the secondary of the transformer with incorporation of an op-amp and class B amplifier [58]. Losses within the resistor at secondary can be kept low by increasing number of windings in the transformer [11]. But such designs increase the size and complexity of the metering mechanism due to additional circuitry. In this set-up, the transformer provides with an electrical isolation and the resistor proves to be the simplest way to obtain an output voltage equivalent. Hall-effect based magnetic sensors comply with both these requirements and hence was chosen as an alternative current sensor in this study.

3.2.1 Hall effect principle

Hall effect is a galvanomagnetic effect that arises in matter carrying electric current in the presence of a magnetic field and was first discovered by Edwin Hall in 1879 [59]. When a current carrying conductor is placed in a magnetic field, a potential difference will be generated

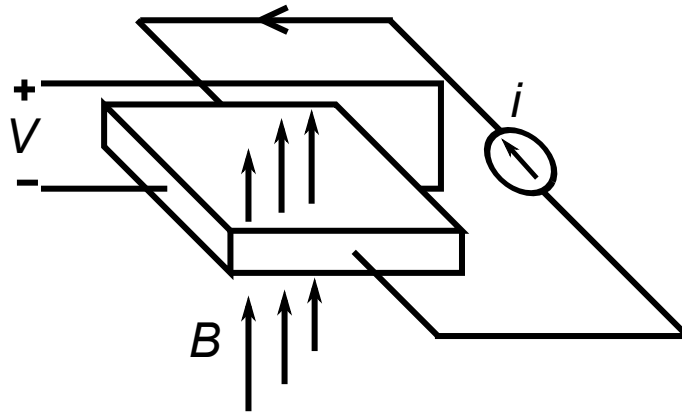


Figure 3.1: Simplified diagram of Hall-effect operational principle.

perpendicular to both the current and the field direction. This principle is known as the Hall effect [60]. Figure 3.1 shows a thin sheet of conductor or semiconductor material carrying current. When a magnetic field B is applied to this sheet in the direction perpendicular to that of the current flow, a *Lorentz force* is exerted on the current. This force disturbs the current distribution and results in a small voltage V across the sheet. The polarity of voltage produced changes when the direction of the magnetic field is reversed. The standard equation for the Hall electric field (E_H) is written as,

$$E_H \sim [\nu \times B] \quad (3.5)$$

where ν is the drift velocity of charge carriers in the conductor which depends on the current and B is the strength of magnetic field applied.

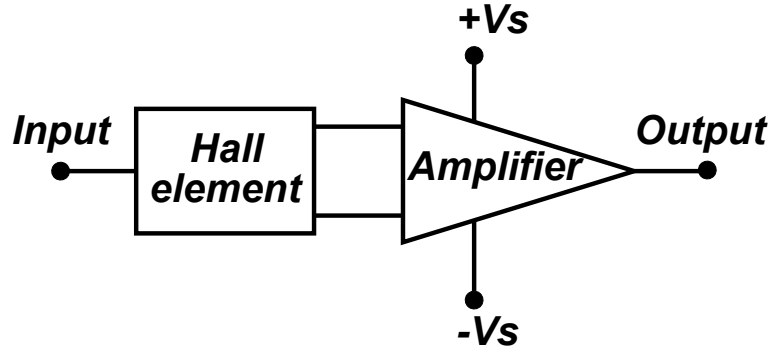


Figure 3.2: Simple configuration of a basic Hall-effect sensor

The carrier velocity ν mathematically is directly proportional to the current but inversely proportional to the number of carriers per unit volume of a material of constant cross-sectional area also referred to as its carrier density. Hence a material with lower carrier density will exhibit the Hall effect more strongly for a given current and dimension. Therefore semiconductor materials are preferred over metals to realize a practical Hall based transducer [61]. The ratio of the Hall voltage to the input current is called the Hall resistance and the ratio of the applied voltage to the input current is called the input resistance of a Hall element [62]. Hall voltage and Hall resistance increase linearly with magnetic field for a large range of applied field (10s

of kilogauss). These parameters also vary with temperature but this variation depends on the behaviour of the carriers in the material with respect to temperature.

Hall based sensors usually require additional electronics like amplification and compensation circuits depending on the application in which they are used. But a basic form of Hall sensor connection is as shown in Figure 3.2. The Hall element senses the magnetic field to be measured and produces a proportional voltage which has to be further amplified. The bias supply $\pm V_s$ imposes limits on the output of the amplifier stage, driving it to saturation if this limit is exceeded. Hence large magnetic fields, do not damage the Hall sensor, rather drive the sensor into saturation [60].

One of the main advantages of Hall-effect sensors over conventional techniques is that they measure magnetic field strength without actual contact with the conductor and hence provide an electrical isolation of several volts or kilovolts. The other important requirements in industrial applications that these sensors fulfil, are low threshold magnetic field or sensitivity for DC and low frequency magnetic fields and stable magnetic sensitivity over a broad range of temperatures [59]. The basic Hall sensors used are low cost, discrete devices. However, advances in semiconductor technologies have led to an increased proportion of Hall sensors in integrated forms [63]. Their compatibility with microelectronics technology has led to an expansion of design enhancements and as a result led to steady performance improvement in Hall sensors, over the last fifty years.

3.2.2 Integrated magnetic concentrator based Hall-effect sensing

Standard CMOS processes are used to realize an integrated Hall sensor and its interface electronics on a single chip. Integrated Hall sensors have found place in applications like the electronic compass [64], battery management, solar converters and also in the automotive and computer industries. Basic Hall cells have limitations when it comes to larger distances from the current carrying conductor, they do not operate accurately unless a strong magnetic field is produced. Temperature and stress also affect the electrical resistance and carrier mobility in the

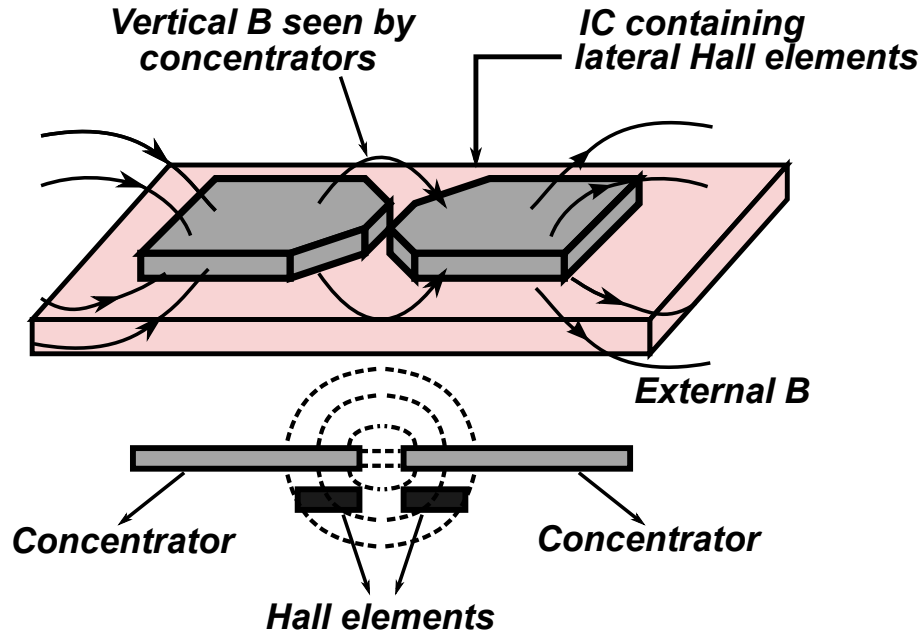


Figure 3.3: Hall-effect based sensing using Integrated Magnetic flux Concentrators.

Hall element which affect its sensitivity. Another problem is the presence of an offset voltage, that is, the presence of a small output even in the absence of a magnetic field, due to physical inaccuracies and material non-uniformities. Integration technology allows improvement in the sensor performance in spite of these limitations by enabling incorporation of circuits for biasing, offset reduction, temperature compensation, signal amplification and so on [59].

One such integrated design which consists of flux concentrators in the vicinity of Hall elements to strengthen the magnetic field seen by the element was first introduced in 1999 [65]. This configuration makes the Hall sensor suitable for measurements of even weak magnetic fields. Such a sensor is less sensitive to external interference fields too. As in Figure 3.3, the two flux concentrators are placed close to each other and the Hall elements are placed below in the air gap of the concentrators. Conventional Hall ICs are made of CMOS integrated circuits that contain lateral Hall elements at their surface. These elements by principle are only sensitive to a magnetic field perpendicular to the chip surface. By adding Integrated Magnetic Concentrators (IMC) made of highly permeable, low coercive field, amorphous ferromagnetic material, directly on the chip surface, an additional field component is introduced. The two

parts of the IMC collect and amplify the small magnetic flux generated around the current carrying conductor parallel to the chip surface and locally rotate the in-plane component into a magnetic field perpendicular to the chip surface. Therefore the Hall elements see an additional vertical magnetic field going down on one side and going up on the other side. The sensor output voltage is then generated by subtracting the output voltages of the two Hall elements. This architecture of an integrated sensor can increase the flux density seen by the Hall elements by a factor of six or more [66].

This combination of Hall-effect sensor, flux concentrator and a conductor, into a single assembly opens up applications alternative to existing conventional current sensing methods. This architecture decreases package size, prevents external connection of the sensor and reduces insertion losses [12]. The MLX sensor is one such commercially available sensor which produces an analogue, linear, ratiometric output voltage proportional to applied magnetic field.

3.3 Summary

This chapter provides a discussion about various current sensing principles, and techniques based on those principles that have been used in the past century and that are currently used in commercial applications. We focus on magnetic current sensing in this chapter, more specifically on the Hall-effect based current sensing technique. Basic Hall sensing is based on *Lorentz force* exerted on the current carriers within the conductor in presence of a magnetic field. A more modern approach discussed in this chapter is the integrated magnetic concentrator based Hall-effect sensing. We use one such commercial sensor based on the IMC principle in our model and for our experimental measurements.

Chapter 4

Modelling and Experimental Analysis – Piezoelectric Transformer

A fault in a power system causes changes in properties of both voltage and current signals, for instance, resulting in an under-voltage or over-current condition. Although majority of the faults occur due to deviation in the nature of current flow, voltage signals are preferred for frequency estimation and fault analysis, mainly since it involves a lesser amount of risk. This is because, during fault times, voltages can reach up to twice the maximum ratings in the protective mechanism whereas current levels may go as high as 50 times the maximum ratings. Consequently, there are scenarios when both voltage and current information is required for an accurate fault analysis, for example to calculate quantities such as impedances at a point as seen from the relay. These quantities are then compared to pre-set thresholds to estimate if the system is operating under normal conditions. In this chapter we discuss voltage sensing using piezoelectric transformer through actual experimental measurements and simulation results.

4.1 Finite Element Modelling and Simulation

In order to understand the piezoelectric effect and the principle of operation of a composite piezoelectric transducer, it is necessary to analyse the piezo mathematically. Finite Element

Modelling (FEM) of PTs is based on theory of piezoelectricity defined by mathematical equations discussed in Chapter 2. Representation of PT by the equivalent circuit method is useful but restrictive in terms of taking into consideration effects of PT shape, size, electrode shape, position, etc. The electrical circuit models are usually insufficient to study these PT design aspects and their effect on PT's performance. Hence using FEM techniques for the representation and study of PT behaviour is useful for an overall and thorough understanding of the device properties. The other motivation for the development of model-based analysis of PT, is the presence of different vibrational modes with very different physical characteristics. Incorporating these characteristics completely is only possible in a 3D analysis. Optimization of PT design by simulations without actual time-consuming experiments and ability to evaluate new design materials without actual manufacturing are other main advantages of FEM analysis [67].

4.1.1 Evolution of FEM analysis

A finite element analysis discussed in [67] was one of the first methods used to handle different two-dimensional (2D) and three-dimensional (3D) piezoelectric elements for static, eigenfrequency, harmonic and transient analysis. 3D FEM using commercially available software like *PIEZO3D* and *ANSYS* [68] have facilitated understanding of PT behaviour for a wide variety of electrical boundary conditions, operating frequency ranges and polarizations. A more modernistic approach was adopted in [69] based on 3D FEM that also incorporated effect of external loading conditions. The electrical input admittance, output voltage and efficiency under effect of output loading were demonstrated at resonant and half-resonant frequencies.

In a more recent study [70], owing to its simple structure and ease of fabrication, an electromechanical model for a ring type PT was presented. Based on Hamilton's principle, a theoretical analysis of vibrational characteristics of piezoelectric ring was carried out in this work. In a later work [71], a piezoelectric FEM solver employing parabolic element formulation was developed. Rosen-modal type and unipoled-disk type PTs were studied in this work. Since

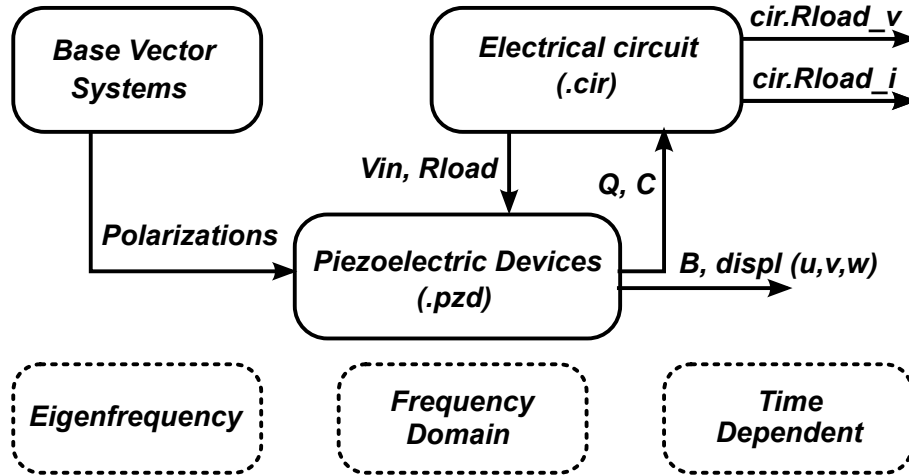


Figure 4.1: Block diagram showing key steps involved in PT modelling with *COMSOL* Multiphysics software and *MEMS* modules.

the FEM PT model has been established and improved with modifications over the years, more recently, this concept has been extended to analyse transformers with varying cross sections [72]. This work establishes that effects of variation of cross-sectional area of a Rosen transformer are significant on the location of the nodal point of operating mode, transformer ratio and input impedance of the transformer. A more recent approach has been towards the introduction of new parameters in the design of PTs; for example the introduction of alloy and metal based electrodes [73]. Analytical method to model PT taking into account its significant non-linearities like dielectric, piezoelectric and elastic non-linearities has been developed in [74] based on classical piezoelectric equations.

4.1.2 Modelling using COMSOL

The PT under test is modelled as a simplified Rosen type rectangular piezoelectric transformer. In this work, we have used *COMSOL* numerical solver [75] for FEM analysis of PT. The logical diagram, Fig. 4.1, shows the modelling steps involved in modelling. The ‘Piezoelectric Devices Interface’ within *COMSOL* combines mechanical and electrical characteristics for modelling of piezoelectric devices. The displacement field and electric potential variables are discretized by quadratic polynomials in our analysis. The ‘Piezoelectric Material Model’ is

used to define the piezoelectric material properties. The mathematical equations corresponding to our model are in stress charge form in which stress and electric displacement are expressed in terms of strain and electric field applied. The mechanical and electrical properties of PT are coupled using the following equations based on the fundamental piezoelectric relations discussed in chapter 2, taking initial conditions into consideration.

$$(T - T_0) = c^E \cdot (S - S_0) - e^T \cdot E \quad (4.1)$$

$$(D - D_0) = e \cdot (S - S_0) + \varepsilon^S \cdot E \quad (4.2)$$

where, T_0 , S_0 and D_0 are initial values assumed zero, c is elasticity and e is coupling coefficient. The strain and electric field are defined as,

$$S = \frac{1}{2} \cdot [(\nabla u)^T + \nabla u] \quad E = -\nabla V \quad (4.3)$$

where, u is displacement, V is electric potential. The elastic behaviour of piezoelectric media is governed by Newton's law and electric behaviour by Maxwell's equation:

$$\nabla \cdot T = \rho \frac{\partial^2 u}{\partial t^2} \quad \nabla \cdot D = 0 \quad (4.4)$$

where, ρ is density of piezoelectric medium. Equations (4.1) to (4.4) form a complete set of differential equations which are solved with appropriate mechanical and electrical boundary conditions [67]. The mechanical and electrical quantities are computed for each discrete element in the model and then solved for the entire media by interpolation. This is based on the generalized Hamilton's variational principle applicable to piezoelectric media which combines differential equation of motion and charge equation of electrostatics with suitable boundary

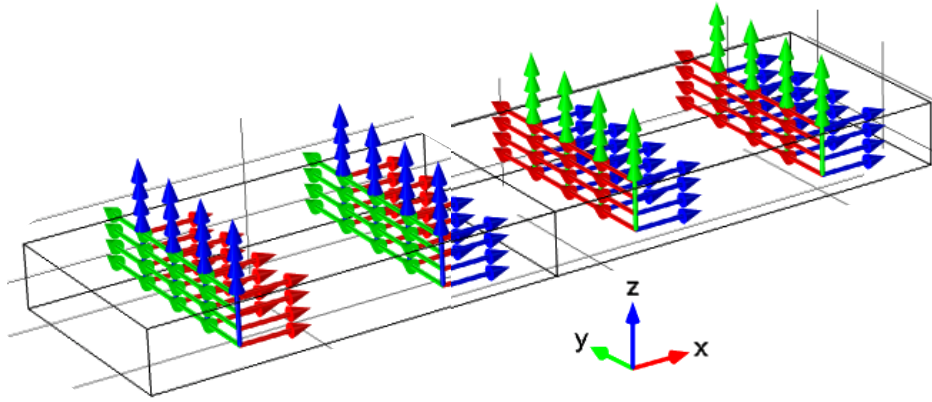


Figure 4.2: Orthogonal polarizations in input and output sections of PT.

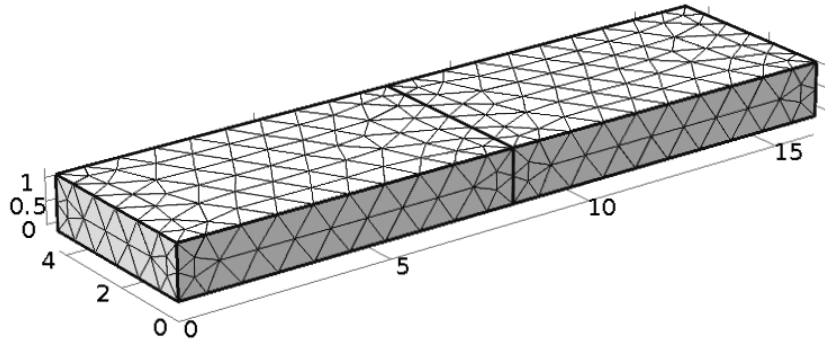


Figure 4.3: Free tetrahedral meshing applied to *COMSOL* PT model.

conditions [76]:

$$\delta \int_{t_1}^{t_2} L dt + \int_{t_1}^{t_2} \delta W dt = 0 \quad (4.5)$$

where, L is a combination of kinetic energy and potential energy available in the media or the *Lagrangian* of the system, and W is the energy generated by external mechanical or electrical excitation.

In order to verify the proposed methodologies, we created 3D model of a Rosen type PT, which consists of input and output sections with the actual dimensions of PT used in our exper-

Table 4.1: Properties of PT type C-205 used in modelling

Property	Value
Density (kg/m ³)	7800
Elasticity matrix (Pa)	$\begin{bmatrix} 15.1 & 5 & 8.7 & 0 & 0 & 0 \\ 5 & 15.1 & 8.7 & 0 & 0 & 0 \\ 8.7 & 8.7 & 13.2 & 0 & 0 & 0 \\ 0 & 0 & 0 & 2.76 & 0 & 0 \\ 0 & 0 & 0 & 0 & 2.76 & 0 \\ 0 & 0 & 0 & 0 & 0 & 3.1 \end{bmatrix} \times 10^{10}$
Coupling matrix (C/m ³)	$\begin{bmatrix} 0 & 0 & 0 & 0 & 13.6 & 0 \\ 0 & 0 & 0 & 13.6 & 0 & 0 \\ -4.26 & -4.26 & 18.5 & 0 & 0 & 0 \end{bmatrix}$
Relative permittivity	$\begin{bmatrix} 1650 & 0 & 0 \\ 0 & 1650 & 0 \\ 0 & 0 & 1580 \end{bmatrix}$

iments. The default polarization direction of piezoelectric material in *COMSOL* is along the z axis. To associate both input and output sections of PT with orthogonal co-ordinate systems, a new base vector co-ordinate system is introduced in the design. This method enables representation of perpendicular polarizations in both sections with respect to each other [77], [78], Fig. 4.2. In addition, we introduced an user defined piezoelectric material to define this model with properties corresponding to PT under test of type C-205 [79], as shown in Table 4.1 in the stress charge form [80]. The meshing applied is an unstructured tetrahedral mesh with size of elements adjusted for the solution to converge with the solver employed, Fig. 4.3.

Our analysis includes three numerical experiments: 1) eigenfrequency analysis, to determine natural resonant modes of PT; 2) frequency domain analysis, to study the behaviour of PT at various frequencies with respect to its mechanical displacement and electrical outputs; and, 3) time dependent analysis, to observe the effects of time varying excitation on PT and transient effects of PT.

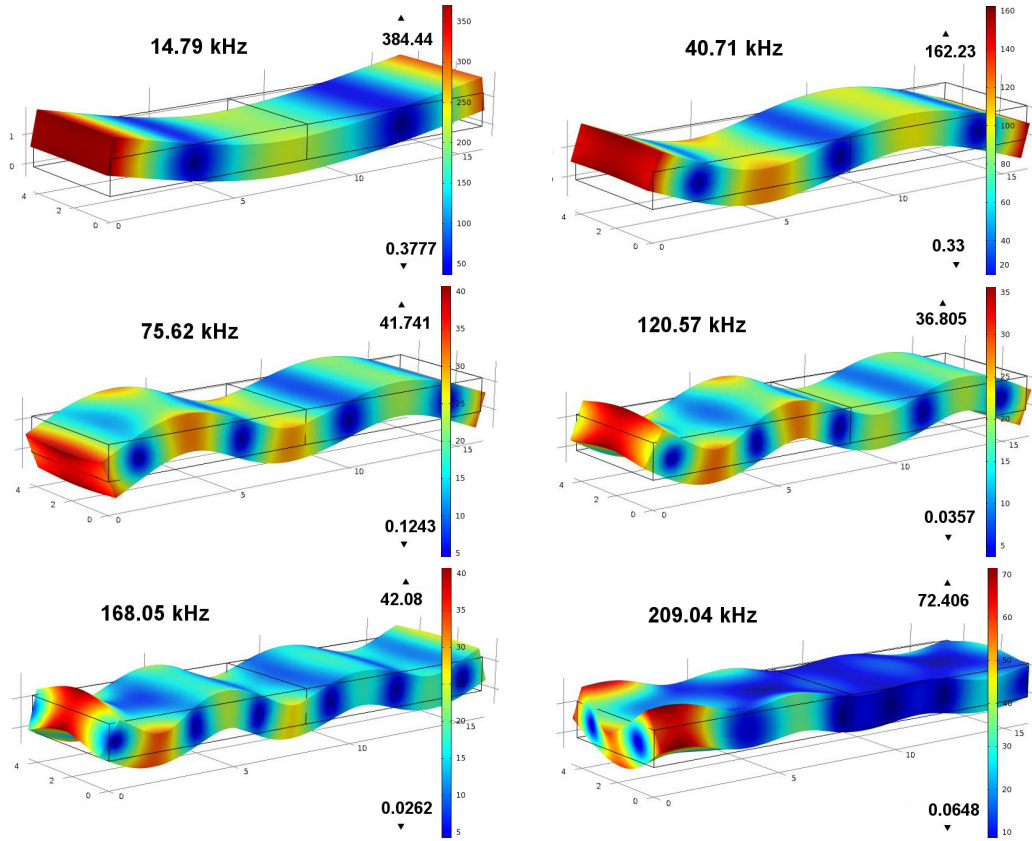


Figure 4.4: 3D plots for PT displacement (volume deformation) in nm at eigen frequencies 14.79kHz, 40.71kHz, 75.62kHz, 120.57kHz, 168.05kHz and 209.04kHz

Natural Resonant Modes

For eigen analysis, the input electrodes are set to type *Terminal* with a nominal voltage, and *Ground* conditions respectively. The output electrode is set to *Floating Potential* with an initial terminal charge of zero. The 3D mechanical displacement plots, Fig. 4.4, depict a mechanical vibration behaviour pattern for every harmonic eigen frequency. The actual resonant frequency that corresponds to lengths and widths of PT model, results for which are reported in the following sections, is 201kHz. We found the peak resonant behaviour in modelling to be very close to the experimentally observed resonance of 209.04kHz. The eigen frequencies that result from eigen analysis and cause the PT to vibrate, also have a small imaginary component that represents a slight phase difference in the signal, caused by the propagation delay through the PT. This is the result of the fact that signals passing through PT are susceptible to a group

delay. This delay can be clearly seen in time–domain waveforms in the following explanation, Figs. 4.12, 4.13.

When excited at harmonic frequencies, standing waves are developed and the strain distribution in the piezo changes and results in volume deformation. The harmonic eigen frequencies which result in a pattern of increasing number of troughs and crests as the input frequency approaches actual resonant frequency are 14.79kHz, 40.71kHz, 75.62kHz, 120.57kHz, 168.05kHz and resonant frequency 209.04kHz. Here with increase in the multiple of harmonic, the strain distribution and hence shape of PT changes. This deformation is in the range of a few nanometres and, as illustrated in Fig. 4.4, is scaled up and exaggerated for visual legibility.

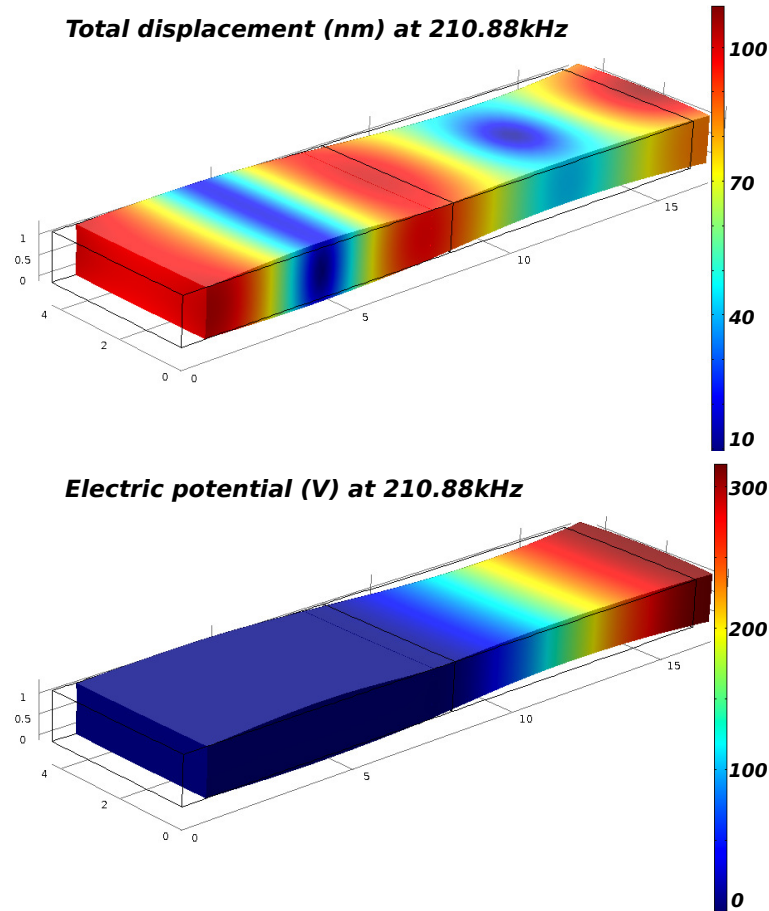


Figure 4.5: 3D plots for PT displacement in nm (top) and output potential in V (bottom) at resonance

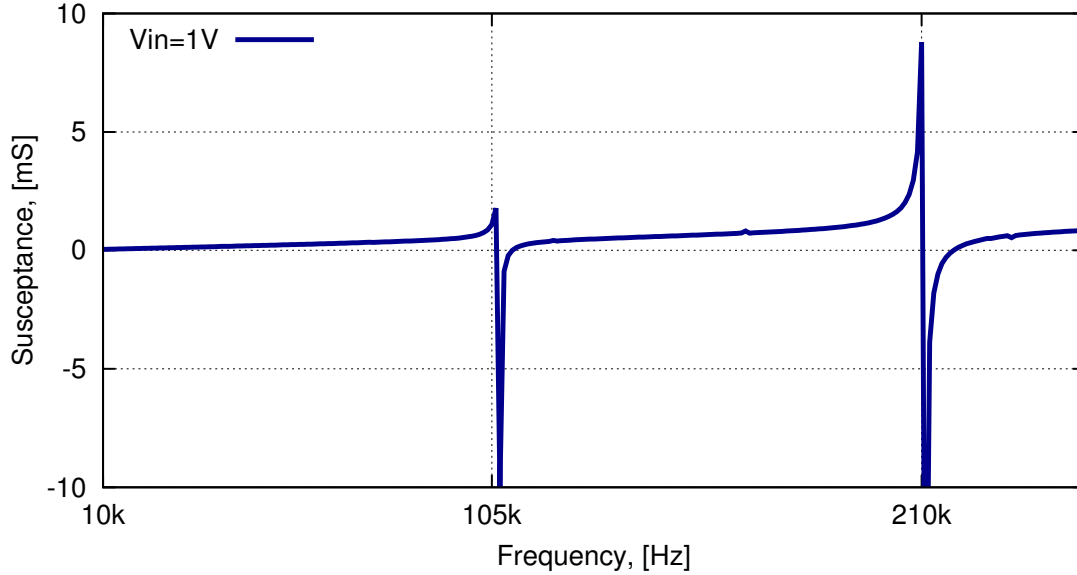


Figure 4.6: Simulated susceptance at the output terminal of PT model at main resonant frequency and at second harmonic frequency.

Frequency Domain Behaviour

For frequency domain analysis, a nominal voltage is applied to the input terminal through an external voltage source whereas the output is terminated by a load resistance of $10\text{M}\Omega$. This is done by adding the ‘Electrical Circuit Interface’. This interface introduces equations to model electrical circuit connections coupled to the distributed field model, to solve for voltages, currents and charges associated with circuit elements. By adding this interface, a default *Ground node* feature is added and is associated with node zero in the electrical circuit. The input and output electrodes are linked to terminal type *Circuit*. The ‘Electrical Circuit Interface’ parameters that couple model terminals to circuit elements are added accordingly. This set-up is most useful for the ‘Time Dependent Study’.

Since the resonant frequency was found to be around 210kHz , a fine frequency resolution simulation from 200kHz to 220kHz was carried out with an interval of 10Hz . This model being a step-up transformer at resonance, the exact frequency at which the highest voltage transformation was recorded, was found to be 210.88kHz . We also observed maximum displacement field and electric potential at the output electrode at this resonant frequency, Fig. 4.5.

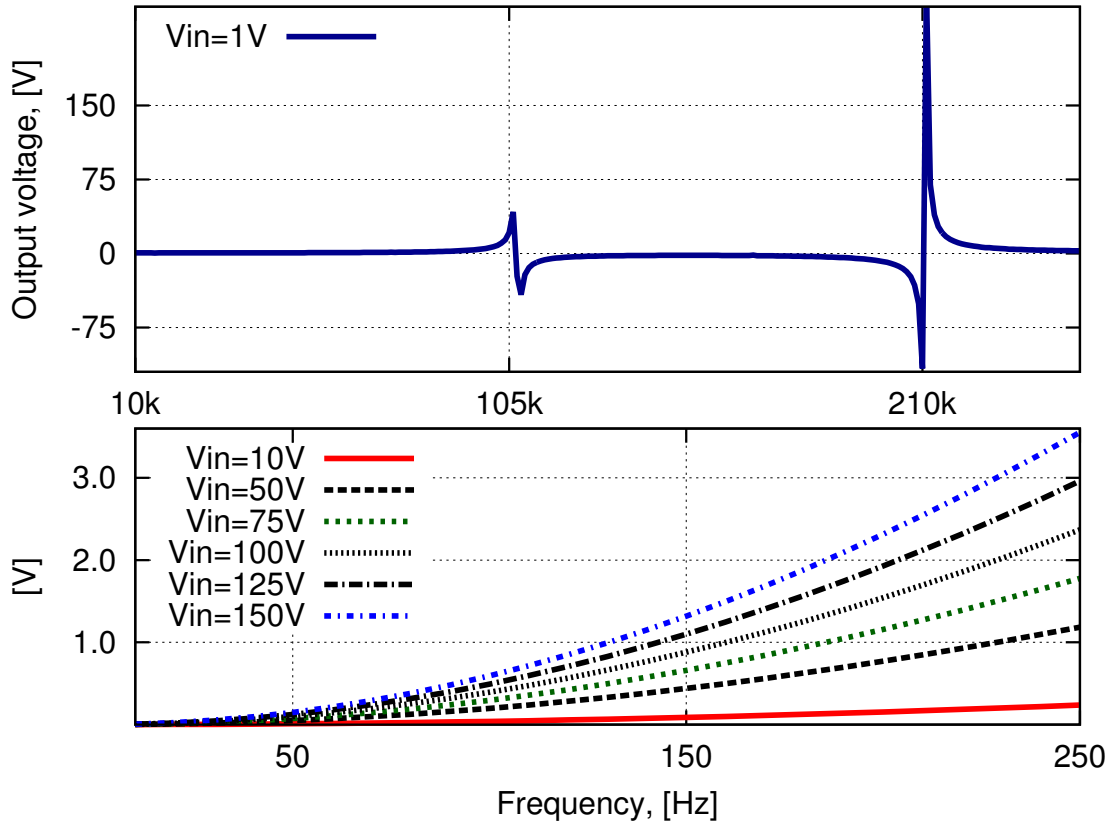


Figure 4.7: Simulated frequency response of PT model showing main resonance and second harmonic frequency (top), low frequency response (bottom) with $10M\Omega$ load termination for varying input voltage.

In frequency domain analysis, for a fixed input voltage magnitude, as the frequency increases, susceptance of PT increases with peaks at eigen frequencies, with highest magnitude at the resonant frequency, Fig. 4.6. Susceptance measurement in *COMSOL* is not inherent and a variable B was introduced defined as the imaginary part of piezo admittance Y_{11} . At resonance, the susceptance increases to approximately $10mS$. As a result of this, with increasing frequency, potential recorded at the output edge also steps up at resonant frequency, Fig. 4.7 (top). In order to analyse low-frequency behaviour of PT model, we ran the frequency sweep in the range of $10Hz$ to $250Hz$. In this range, there was a step-down behaviour and a linear increase in potential, increase in output potential was observed to be in order of few volts with no significant peak at any frequency as was observed in the resonant frequency region. Even

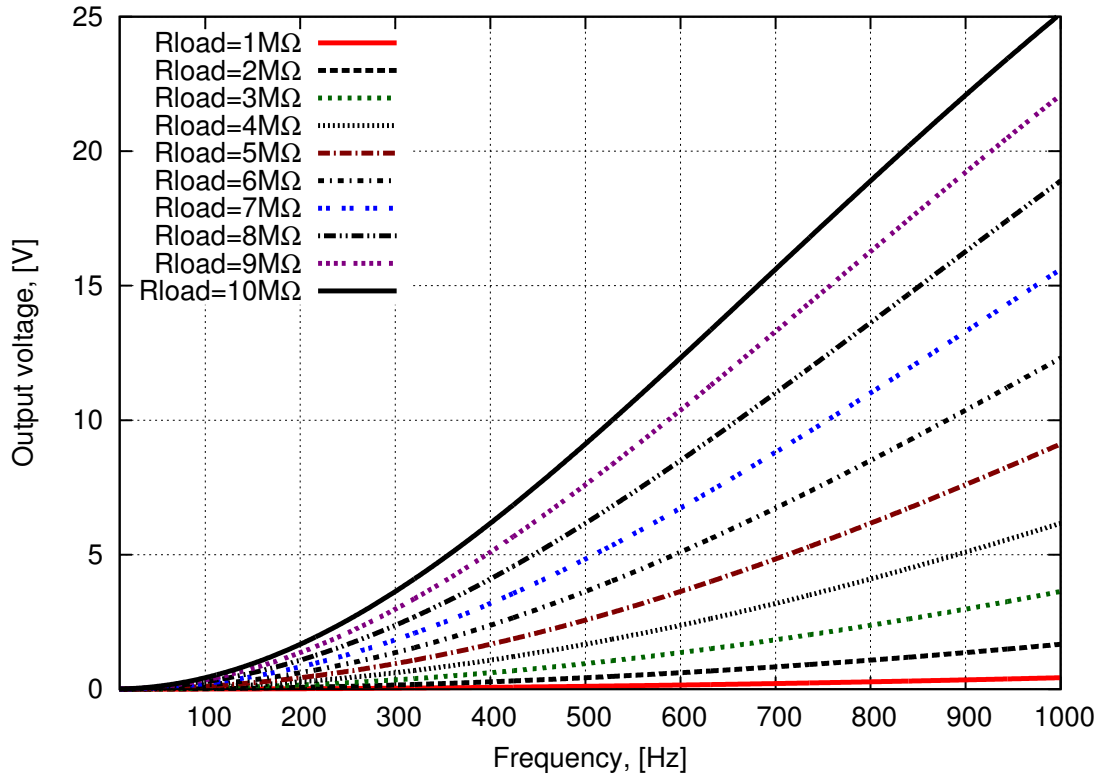


Figure 4.8: Simulated effect of resistive loading on PT model output behaviour in *COMSOL* at varying frequencies.

as the applied input voltage increases from 10V to 150V, the output voltage increases at each frequency, Fig. 4.7 (bottom).

Behaviour of PT for varying load was also observed in the frequency domain analysis using the ‘Electrical Circuit Interface’ and a parametric sweep with load resistance in circuit interface as the varying parameter. For a resistive load variation of $1\text{M}\Omega$ to $10\text{M}\Omega$, the PT output varies linearly with frequency as well as with increasing load. The model response for varying load for a frequency range of 10Hz to 1kHz is as plotted in Figure 4.8.

Time Domain Analysis

The most significant analysis carried out is the ‘Time Domain Analysis’, to test the PT model with real-time power signals. Using this study within COMSOL it is possible to expose the model to power-line single-tone signals as well as multi-tone faulty signals.

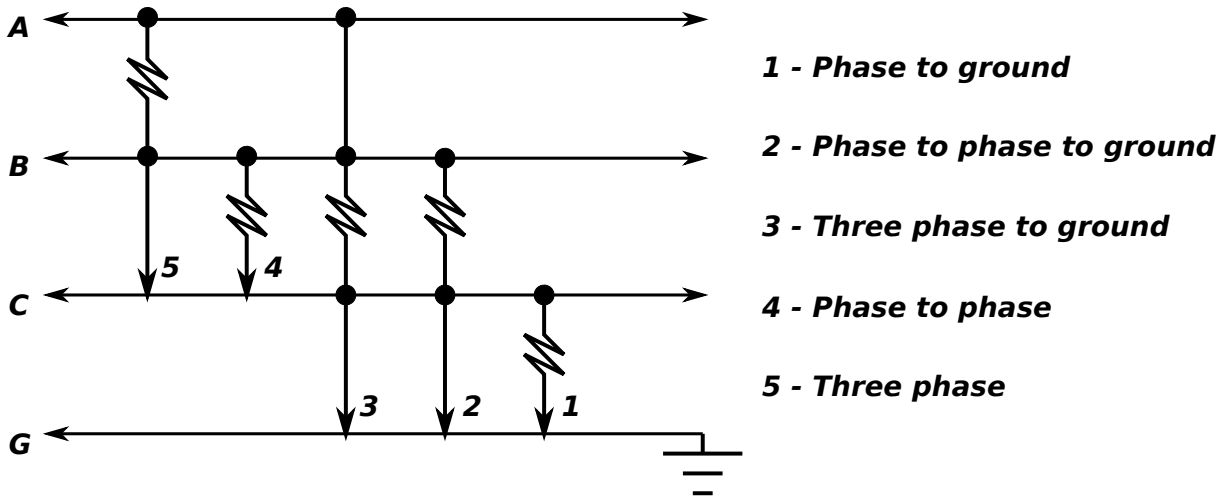


Figure 4.9: Typical types of faults in a 3 Φ power system.

In faulty conditions, the real-time simulated signal consists of a 60Hz tone intruded by high-frequency glitches. In power systems, a *fault* is any aberration in a normal current flow. In 3 Φ power systems, a fault may occur either between one or more phases and ground or only in between phases [81]. Figure 4.9 shows the typical faults in a 3 Φ system.

We generated realistic time domain signals using the ‘Power System Computer Aided Design’ (*PSCAD*) software. *PSCAD/EMTDC*, developed by the Manitoba HVDC Research Centre, is an electromagnetic transient analysis program that uses a graphical user interface for constructing input data files. This gives flexibility to work with voltage and current values out of normal range for purpose of experimentation [82]. A power system was simulated within this software to generate secondary voltage signals. We then performed a time domain analysis using these exported power voltage signals applied to primary of PT model for fault type ‘phase to phase to ground’. The ‘Interpolation’ function within *COMSOL* enables this generation of input functions by exporting a data file which contains values of the voltage signals in discrete points in time.

The primary section of PT vibrates in accord with the applied time varying input, Fig. 4.10. At the moment when the PT encounters a high frequency glitch (here at $t = 1$ s), its vibration frequency also increases, and in turn increases the relative output potential generated, Fig. 4.11.

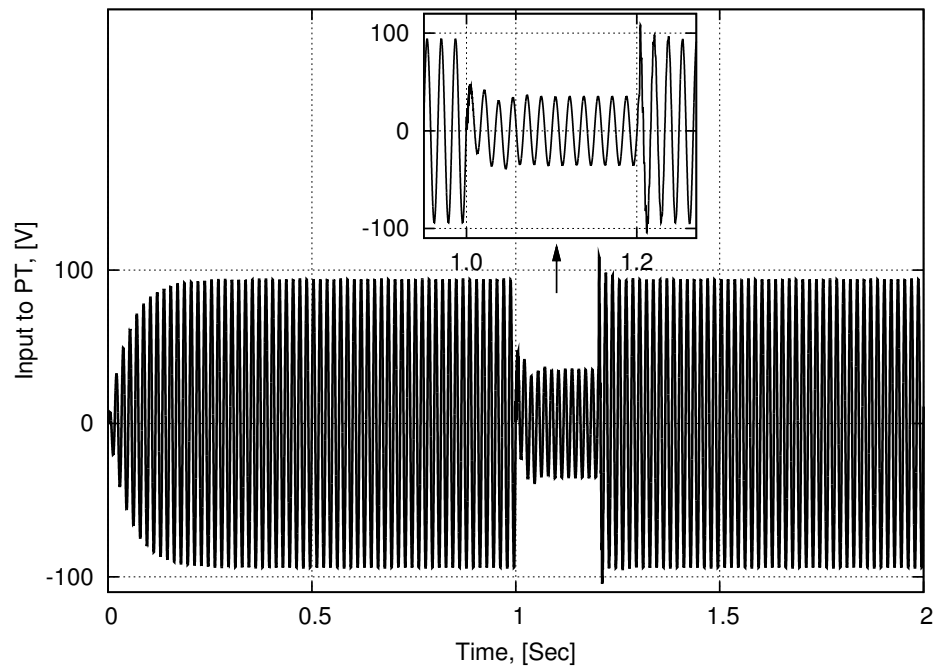


Figure 4.10: Time-domain *PSCAD* generated voltage signal applied to PT model as input.

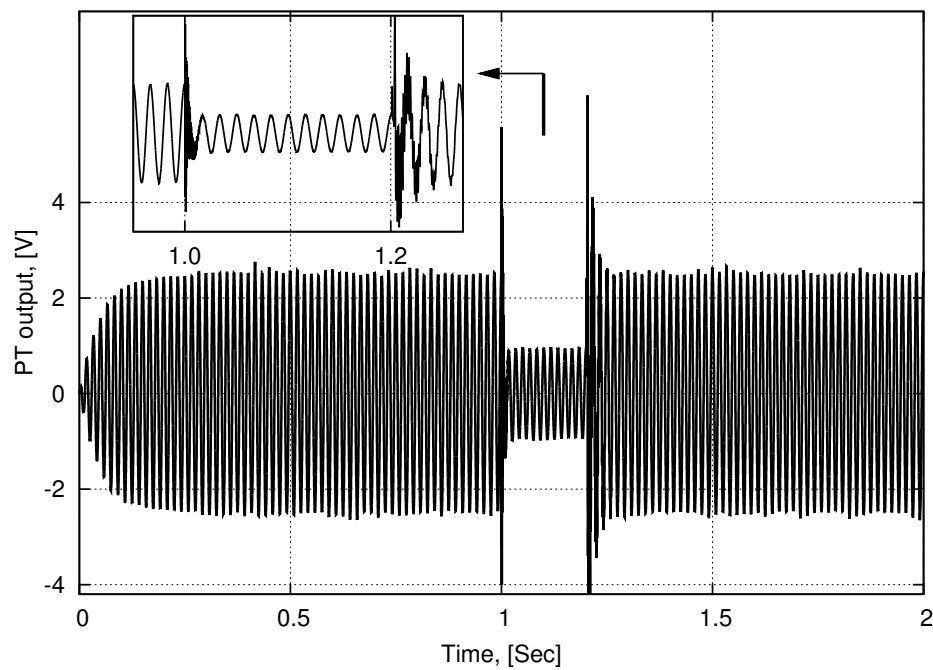


Figure 4.11: Stepped down output voltage of PT model for high voltage time-domain input applied

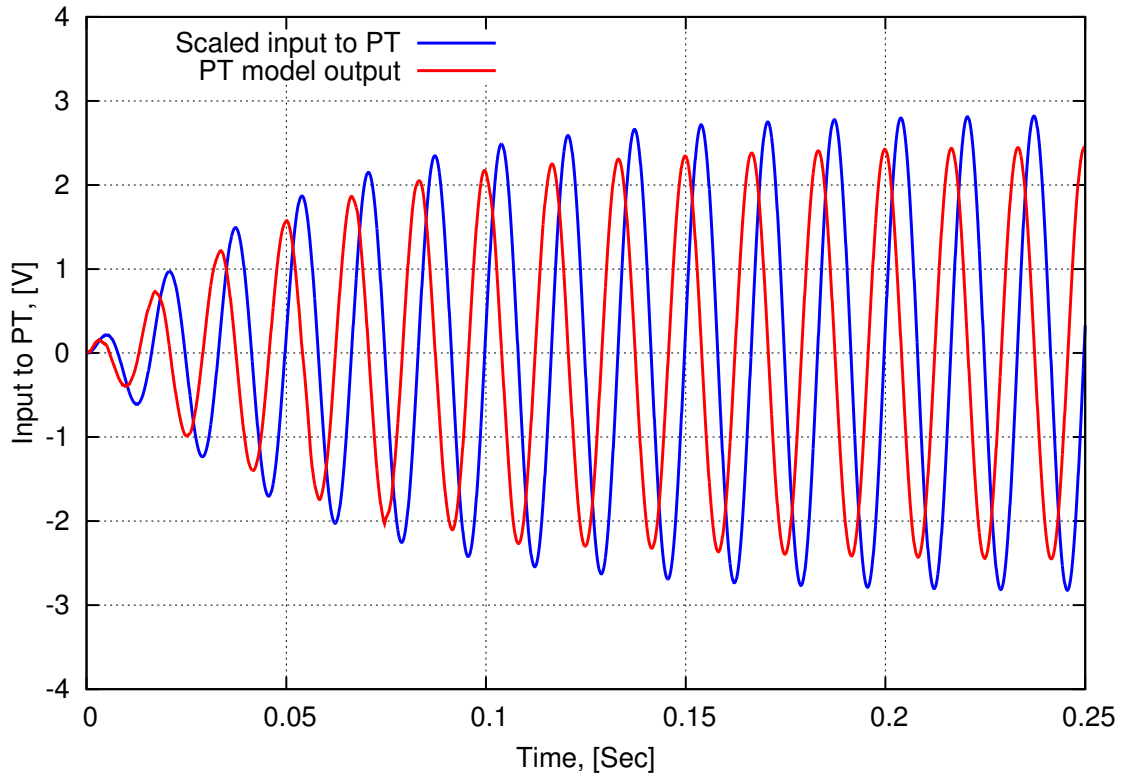


Figure 4.12: Simulated phase delay between input to PT model and output recorded for that input for 60Hz component.

Although the high voltage sinusoidal input is stepped down by the PT, the high frequency components in this input are amplified relative to the 60Hz components of this input.

4.1.3 Other considerations

Group delay

Group delay is a measure of time delay of amplitude envelopes of various sinusoidal components of a signal through a device under test, PT in our case, and is a function of frequency of each component. When a signal composed of multiple frequency components passes through PT, it suffers distortion because these components are not delayed by the same amount of time at the output of the PT. This changes the shape of the signal in addition to any constant delay or scale change [83]. In *COMSOL*, during the ‘Time Dependent Study’, we observed that low frequency signals exhibit longer lags after passing through PT while, in comparison, higher

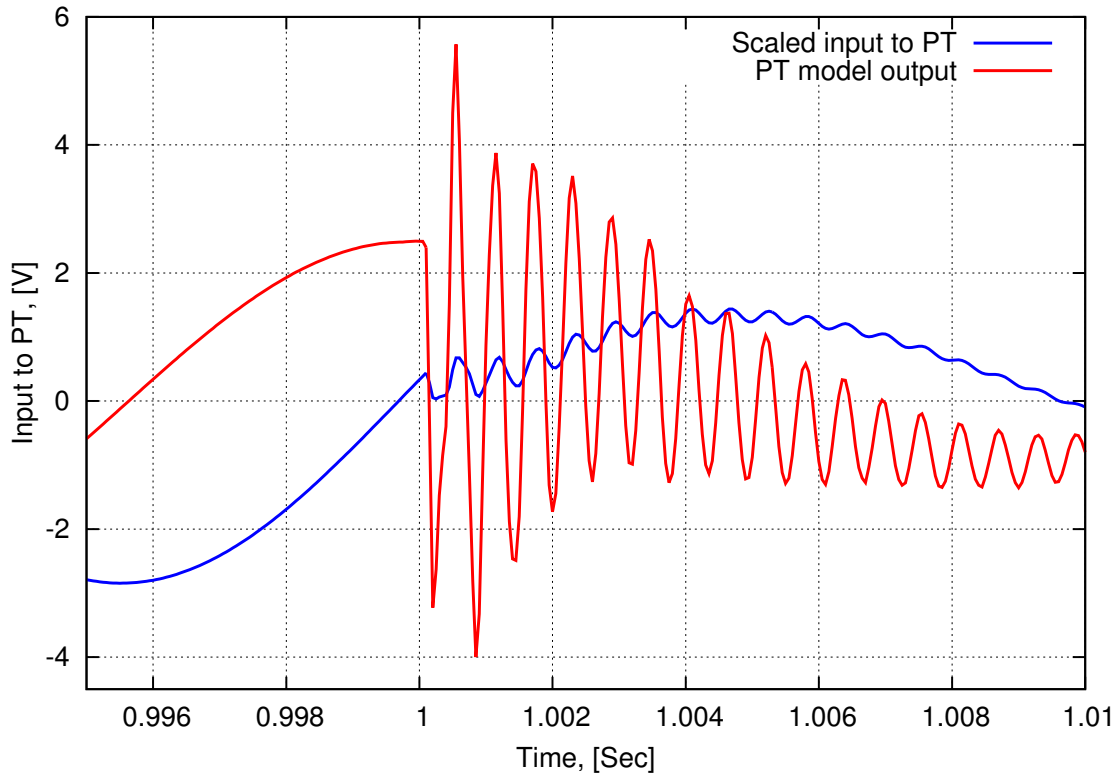


Figure 4.13: Simulated phase delay between input to PT model and output recorded for that input for high frequency component.

frequency tones exhibit progressively shorter delays. We found this delay to be less than 3ms consistently for the 60Hz component, Fig. 4.12. This delay was negligible for high frequency components and the signal appeared at PT output almost at the same time as it was applied to PT's input, Fig. 4.13.

Propagation velocity, PT dimension and resonant frequency

Another property demonstrated in our model is the dependence of the PT resonant frequency on its physical dimensions. The velocity of propagation v through piezoelectric ceramic also depends on its vibration mode. For a particular shape and vibration mode, the wavelength of vibration λ is related to its propagation length l at a resonant point by,

$$\frac{\lambda}{2} = l \quad (4.6)$$

Table 4.2: Effect of length of PT (l) on resonant frequency (f_r) and on low frequency output voltage

l (mm)	f_r <i>Comsol</i> (kHz)	<i>Actual</i> f_r (kHz)	<i>Peak output</i> (V)
10.07	315.54	325.5	0.156
16.07	209.04	201.4	0.26
20.06	161.63	161.0	0.265
37.19	73.32	88.4	0.348
50.07	62.271	66.46	0.438

The velocity of propagation through a piezo ceramic is therefore proportional to its propagation length and resonant frequency f_r [27],

$$f_r = \frac{v}{2 \cdot l} \quad (4.7)$$

As expected when we tested our model for increasing lengths, resonant frequency decreased, Table 4.2. When excited by a 100V, 60Hz input signal, this increase in the PT length dimension, results in an increase in stepped-down output voltage measured at secondary terminal of the PT model. The recorded peak output voltages are as shown in Table 4.2. The resonant frequency for each length was evaluated in *COMSOL* using eigen analysis. Our model demonstrated, on average, a deviation of 4.5% from actual resonant frequencies.

Initial displacement and loss factors

In the low-frequency region, the piezo is very sensitive to vibration or any external perturbation, thus, in our model the initial stress and strain are assumed to be zero. In our model, all the boundaries have a default *free* boundary condition, i.e. no constraints or loads are assumed to be acting on the boundaries. In our future work, more detailed simulations for parameters such as initial stress and strain, damping and loss will be calculated to create a more practical modelling environment. That is, we will include a model of a suitable support structure such as a damping spring, where the loss and damping constants will be evaluated for optimum performance. The placement of these structures will be decided on the vibration operating mode

of PT to ensure that fixed constraints if any, coincide with the region of zero PT displacement. Consequently, depending on the performance of our model, we will propose an appropriate packaging design for our sensor configuration. The mechanical considerations involved in design of this package are discussed in the next section.

4.2 Experimental Results

In order to validate our model results, we carried out a few measurements on the PT presented in the previous section.

4.2.1 Device under test

Table 4.3: Specifications of PTs under test

Unit	f_r (kHz)	Length (mm)	Width (mm)	Thickness (mm)
1	201.4	16.07	4.29	1.21
2	162.5	20.05	5.39	1.219
3	161	20.06	5.39	1.212

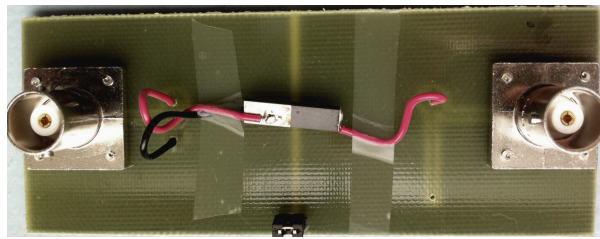


Figure 4.14: Photo of input and output connections for single-ended PT.

In our very first set of experiments, we observed a peculiar step-up behaviour at a low frequency of 40Hz for a PT manufactured to resonate at 161kHz. 161kHz happened to be a harmonic multiple of 40Hz and hence to be able to recreate this effect at a power-line frequency of 50Hz, we extrapolated the harmonic multiples for 50Hz and calculated the corresponding resonant frequency to be 201.4kHz. Customised PT that would resonate at 201.4kHz was commercially manufactured to order. We therefore experimented with three Rosen piezoelectric

transformers from ‘Fuji Ceramics’ made of lead zirconate titanate material, with specifications summarized in Table 4.3 [84].

Primary side of the PT is a side-plated bar and the secondary side is an end-plated bar, Fig. 4.14. It typically operates in the length extensional vibration mode at its first harmonic frequency such that a full one-half standing wave exists on the body [85]. This PT structure has a common ground between input and output. Along with the physical dielectric capacitances formed by PT input and output electrodes, stray capacitances also appear between the PT input and output. These factors play a significant role in deteriorating the Common Mode Rejection Ratio (CMRR) of the device. This further worsens the signal to noise ratio at the output terminal [86].

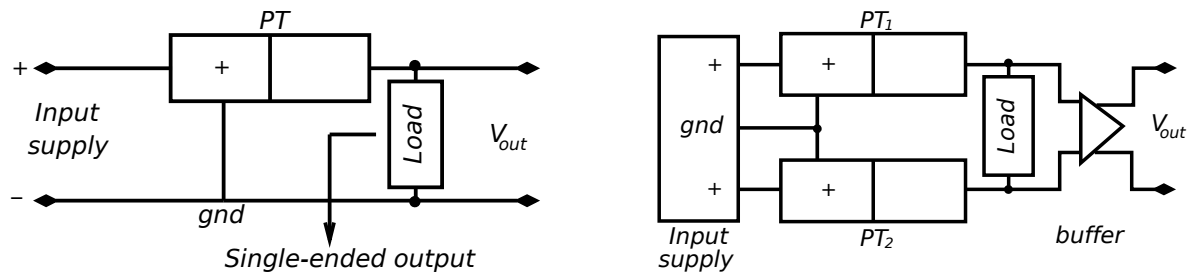


Figure 4.15: PT configurations: Single ended connection (left), differential connection (right)

Although a PT proves to be a good isolation transformer as compared to conventional electromagnetic transformers, when used in power systems, occasional sudden surges may cause damage if propagated from input to the output. Isolation of high power input side from low power control circuitry is important for prevention of damage due to these sudden surges in power systems. One way to achieve ground decoupling, is to connect two PTs in a differential configuration [87], Fig. 4.15. Another method to deal with these spurious high frequency surges is to use excessive filtering and signal processing at the input of transformer. One such efficient actuating circuit, small in size but with a wide input voltage range is developed in [88].

6. *Tektronix DMM4040* 6.5 Digit Precision Multimeter for metering and recording the output;
7. *Tektronix DPO7354C* Digital Phosphor Oscilloscope for output signal monitoring and measurements.

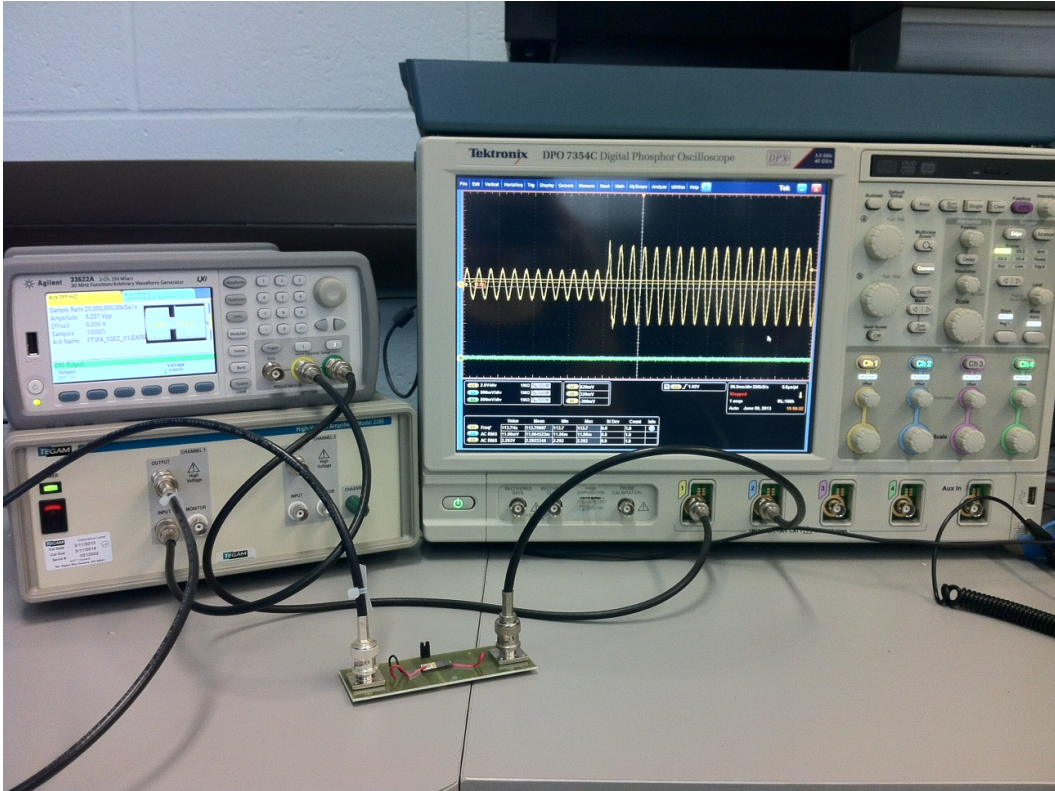


Figure 4.17: Most recent experimental set-up for measurements with real-time input signals.

To test the PT with realistic power signals, like in the simulations, we used the *PSCAD* software to generate real-time fault-free and faulty signals. *PSCAD* on a computer interface is used in combination with an *RTP* simulator to physically recreate these signals. The *RTP* suite of tools is a computer based testing environment useful for testing power systems. It is an analogue/digital arbitrary waveform generator, specifically designed to harness the power of *PSCAD* simulation software. The *PLAYBACK* program within *RTP* allows display, configuration and complete control of the waveforms to be played back [89, 90]. Since the *RTP* simulator has a voltage limit for playback, these waveforms are then amplified by use of the

OMICRON amplifier to the level of actual secondary voltage signals before being applied to PT input terminal. This complete set-up is shown in Figure 4.16.

The later part of experiments were done using a new set-up, Fig. 4.17, for which a combination of the arbitrary function of the signal generator and the high-voltage amplifier was used to generate input signals applied to the PT.

4.2.3 Single-tone results

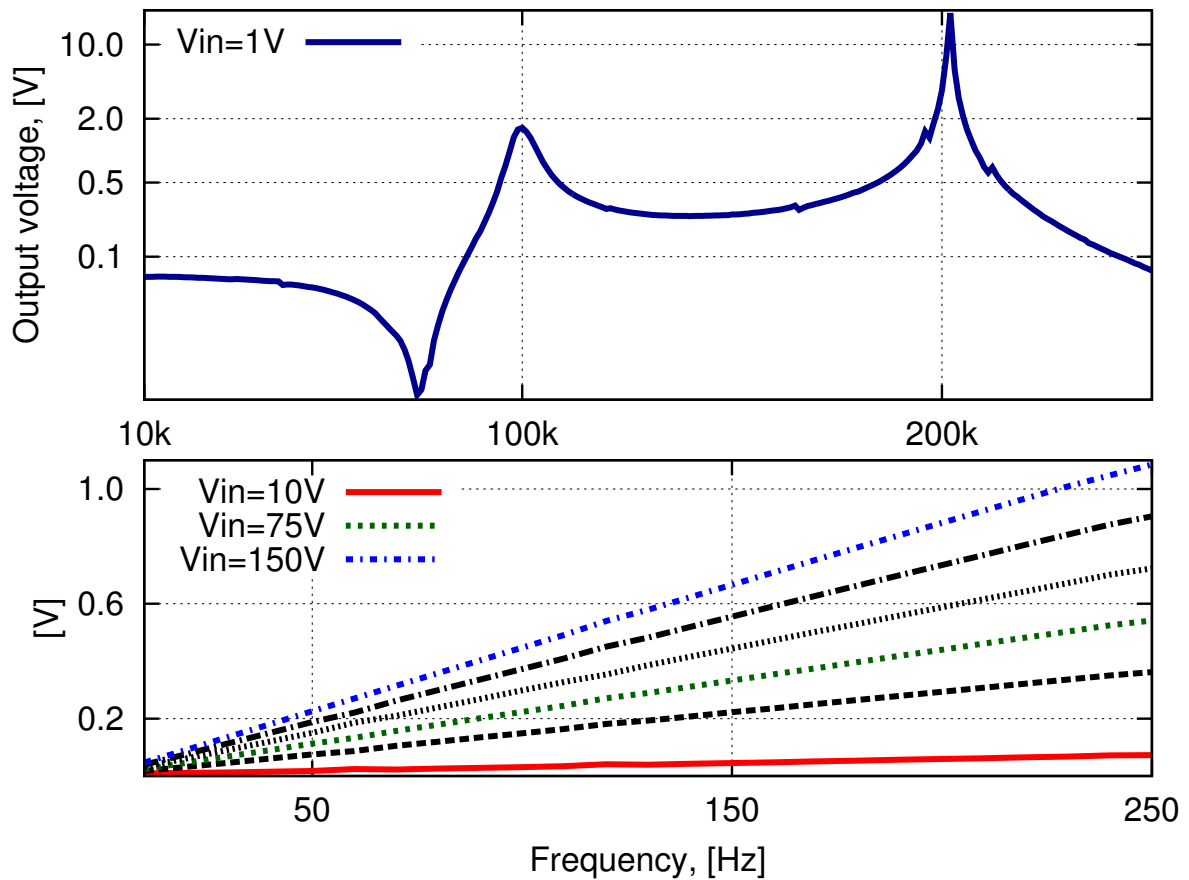


Figure 4.18: Experimentally recorded frequency response showing main resonance and second harmonic frequency (top), low frequency response (bottom) with no load condition for varying input voltage.

Results for the 201.4kHz resonant frequency PT are presented and discussed in this section.

For an AC input signal of amplitude $1V_{rms}$ and near the PT's fundamental resonance, in its single-ended mode, it behaves as a step-up transformer with peak responses of about 20V and 2V respectively at resonant and half-resonant frequencies, Fig. 4.18 (top). However at lower input signal frequencies, ranging from 10Hz to 250Hz, the transformer steps down input voltage as high as 150V, Fig. 4.18 (bottom). For an input ranging from 10V to 150V, we found that the output voltage increases linearly with no significant peak at any frequency, Fig. 4.18 (bottom).

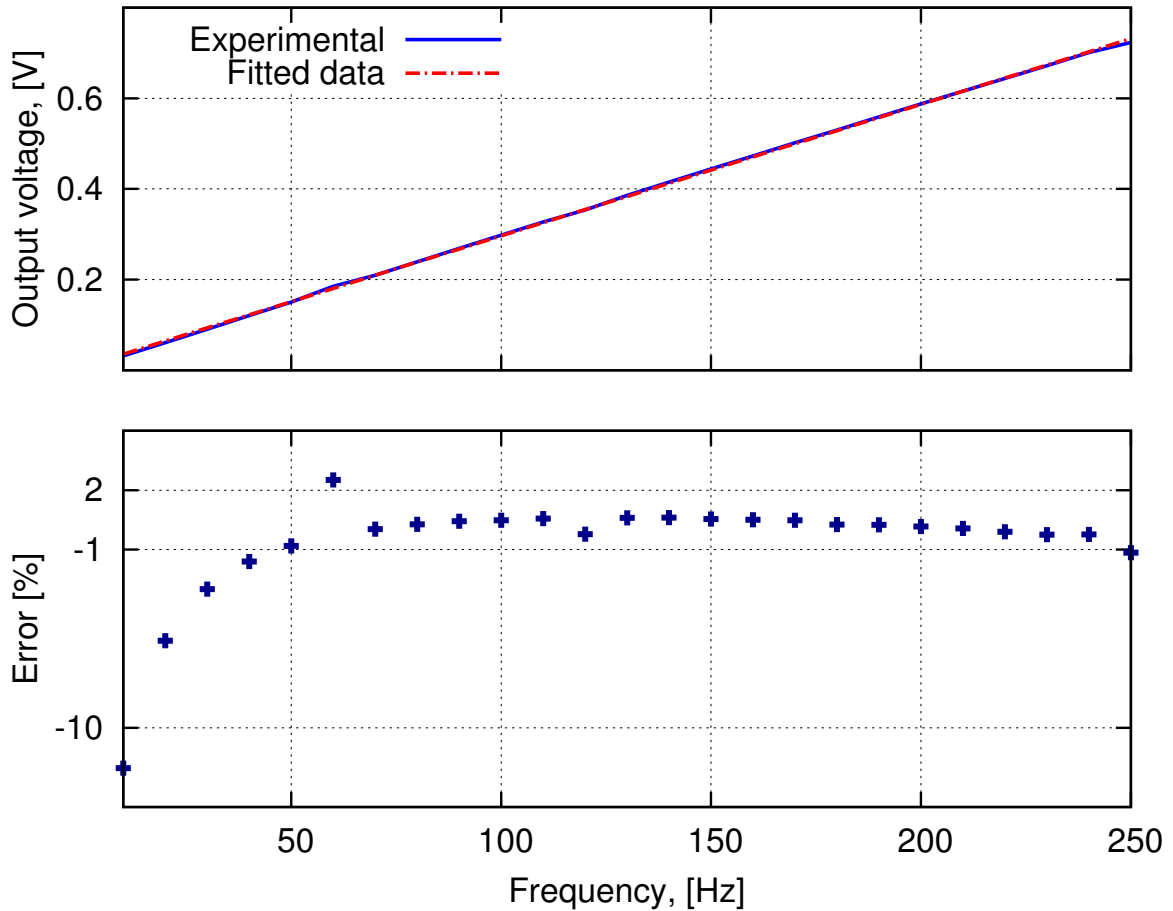


Figure 4.19: Experimentally recorded low frequency response for $100V_{rms}$ input overlapped with results of the fitting linear function of the form $y = ax + b$ (top), percentage error between measured output and fitted data (bottom).

We therefore found this step-down behaviour of PT in low frequency region to be linear

with respect to both frequency and the applied input voltage. To demonstrate this, for an input of 100V to the PT, the output voltages measured from 10Hz to 250Hz signal frequency are mapped into a linear function of frequency. Using a simple curve fitting tool, this linear relation between input frequency and output voltage was found to be $y = 0.0029x + 0.0065$, which closely represents the recorded output voltages, Fig. 4.19 (top). The error percentages calculated between actual recorded output voltages and linearly fitted outputs lie within $\pm 1\%$ for the frequency range of interest. Similarly, the output voltages measured were also found to be linearly varying with respect to applied input voltages. This PT action was observed consistently up to approximately 2kHz. This property of consistent linear behaviour of PT in power-line frequency region makes it useful in low power consumption area of voltage transformation in power systems.

4.2.4 Loading Effect

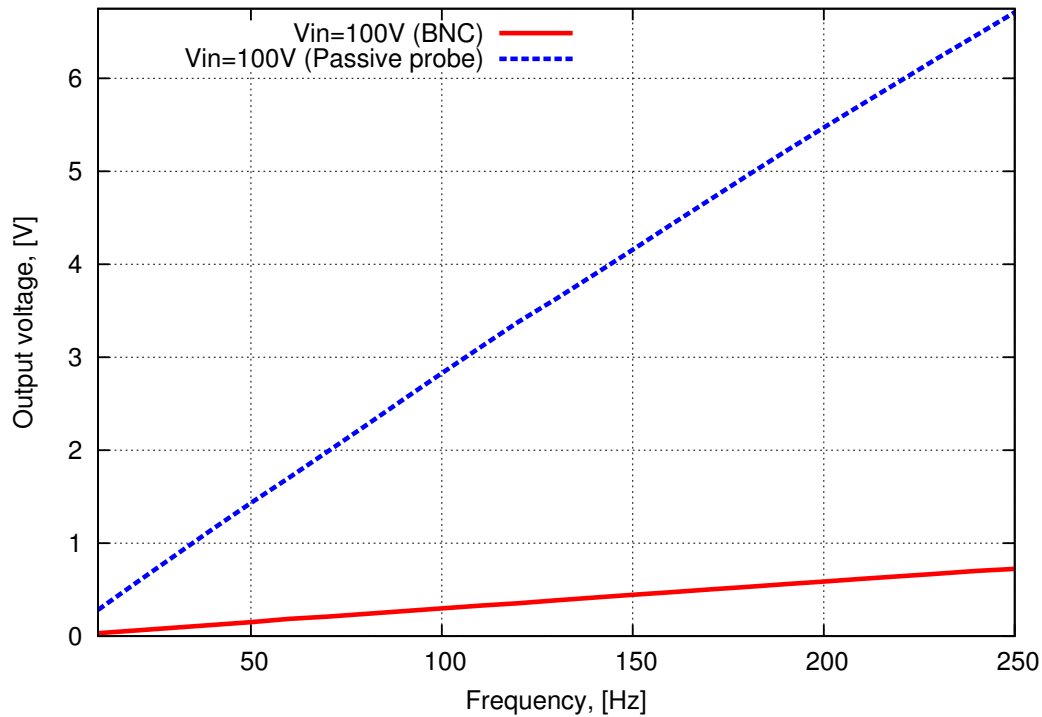


Figure 4.20: Experimentally recorded low frequency response for $100V_{rms}$ input using a regular BNC compared with passive probe demonstrating loading effect.

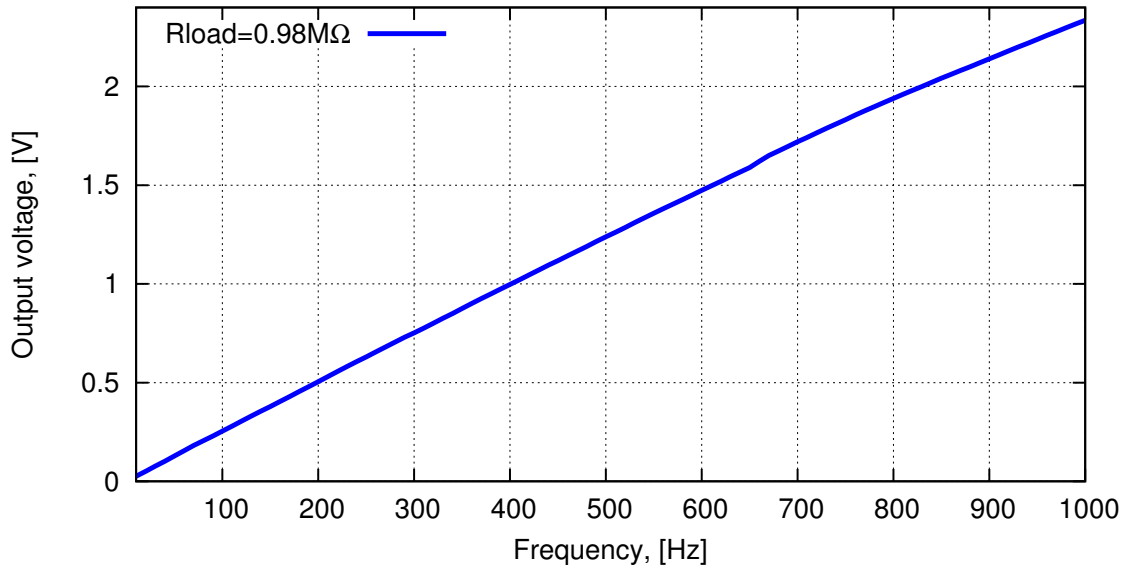


Figure 4.21: Experimentally recorded effect of resistive loading on PT output behaviour for varying frequency

As seen in the set-up, the PT output is connected directly to the oscilloscope using BNC. This causes the oscilloscope to load the PT circuit, since the input impedance of the scope becomes significant and affects the actual measurement. The oscilloscope used in the set-up has analogue channels that introduce $1\text{M}\Omega$, 13pF input impedance. The output impedance of PT in the low frequency region is high. With a normal BNC connection, the scope impedance becomes considerable in drawing signal current from signal source and hence attenuates the actual measured PT device output signal. To maintain maximum output signal fidelity, we used a frequency compensated passive (10X) probe, with a $10\text{M}\Omega$, 8pF impedance to compensate for the input impedance of the scope. With this probe, the output is almost exactly equal to the actual PT output that should be, without any loading effects. The amplitudes are higher as compared to those measured using normal BNC with a relatively higher slope linearity. An example with 100V_{rms} input is as seen in Figure 4.20 where the output voltages vary in amplitude when measured using the passive probe.

The current which contributes to mechanical vibration in piezo material, depends on load resistance. Hence resonant and higher harmonic voltages are functions of load resistance and

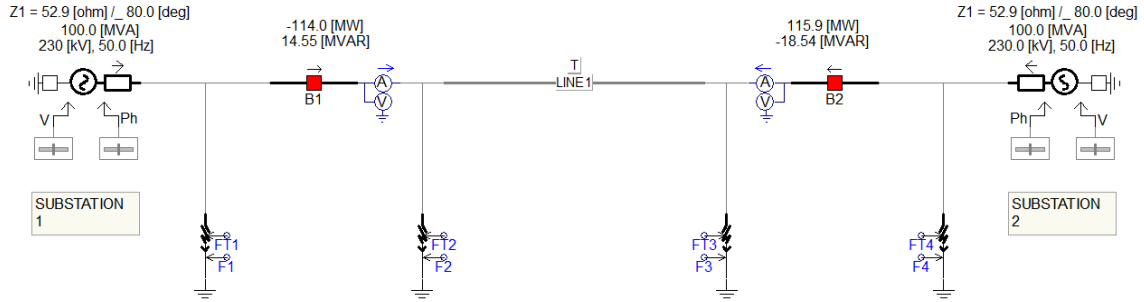
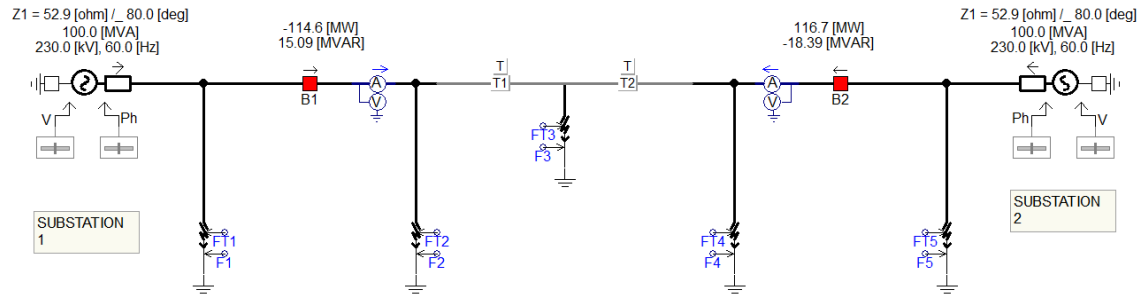
the effects are examined in [91]. Loading affects quality factor and the PT electrical impedance and hence affects resonant behaviour of PT. The PT's output static capacitance is characteristic of its output impedance. In the resonant frequency region, when load impedance becomes comparable to output impedance of PT, it sinks more mechanical power and the step-down/step-up ratio begins to drop [32]. This drop can be understood by considering the fact that the static output capacitance and the load impedance form a high pass filter. The real part of this high pass filter deviates the resonant frequency, while its imaginary part reduces the quality factor. PT voltage gain, power and efficiency are therefore load dependent; voltage gain increases with the load and reaches a maximum in open circuit condition (infinite load) [85]. A similar behaviour is observed in the low frequency region. Characterization of the PT with loads ranging from $1\text{k}\Omega$ to $1\text{M}\Omega$ yields a linear trend in output voltages.

Due to the practical limitations of low frequency measurements in our current set-up, highly accurate frequency response for variation in load impedance is difficult to obtain. Figure 4.21 shows PT response for an external resistive load of $0.98\text{M}\Omega$ at PT's output, for frequency variation in the range 10Hz to 1kHz . At 60Hz , the output is approximately 0.155V for $0.98\text{M}\Omega$ load, with an evaluated current value of $0.16\mu\text{A}$ which gives an approximate VA rating of $0.0245\mu\text{VA}$. It should be noted that these secondary signals obtained at piezo output only serve as the input signals to an ADC and/or other integrated circuits (ICs), and hence these low power signal levels are preferred.

4.2.5 Real-time analysis

The next set of results were obtained for realistic power system signals. An earlier work investigates time-domain characteristics of transient response of PT with open-circuit operation [92]. The results in this work are however obtained when a high voltage transient is induced at the input terminals of PT immediately after an AC voltage connected to the PT is switched off. Very little research has been done in the area of time-domain and transient response of PTs.

In our work, in order to analyse PT behaviour with real-time signals, we have considered

Figure 4.22: Schematic diagram for *PSCAD* case 1 power system simulation model example.Figure 4.23: Schematic diagram for *PSCAD* case 2 power system simulation model example.

two cases in *PSCAD* that simulate two 3 Φ substations connected via a single transmission line. The in-built power system model consists of two impedance sources connected via a 100km transmission line. It has a settable system voltage via source equivalents and full fault control panel with various fault combinations for different positions and types. A snapshot of the models used in *PSCAD* are demonstrated in Figures 4.22 and 4.23. In case 1, a fault occurs between source 1 and circuit breaker 1. In the case 2, a fault occurs at midpoint between two segments of transmission line $T1$ and $T2$. In both cases, we evaluated faults both between any two phases, and between phases and ground. These signals were recreated using the *RTP* simulator and applied to PT through the high-power amplifier. A fault-free power-line voltage signal contains only a pure 60Hz tone. But a faulty signal is intruded with higher frequency and glitches of varying amplitude.

The PT output demonstrated here is for case 2 and the fault type considered is the AB-g fault. The total duration of the signal applied to PT was 5s. The fault was controlled to occur at 2s and last for a duration of 0.5s using the timed fault logic within the power system model.

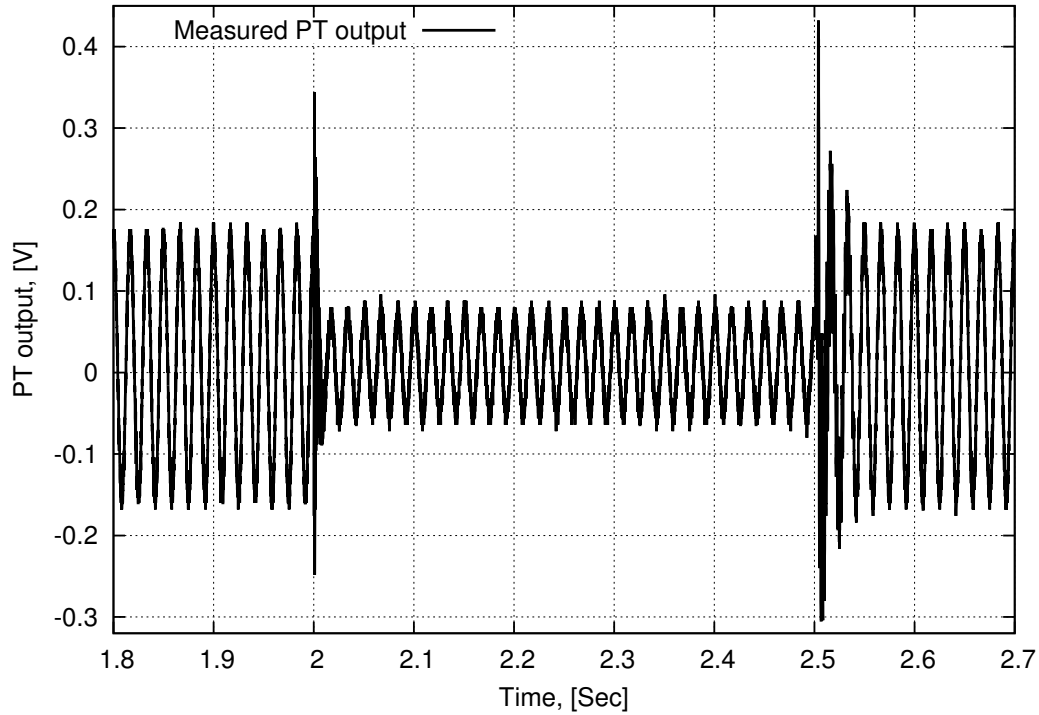


Figure 4.24: Stepped down PT output voltage for high power input applied experimentally

The breaker in this model, controlled by a timed breaker logic, is not used in our case since we want to apply the actual secondary fault voltage to PT, before any fault corrective action. For this applied input, the PT output is a stepped down sinusoidal output voltage. Here, similar to as observed in the model behaviour, although the high voltage sinusoidal input is stepped down, high frequency glitches are amplified relative to the 60Hz component, Fig. 4.24. The amplitude of these glitches is usually 10 – 20% of amplitude of power-line frequency component. Hence although these high frequency glitches are amplified to more than 10–20% of the stepped down output voltage, they still get attenuated. The same experimental set-up as in the single-tone measurement is used to record this output.

4.2.6 Experimental group delay measurement

In power systems, power line frequency sometimes is intruded by unwanted spurious high frequency transients, which if propagated may result in damage of the system. Usually high–

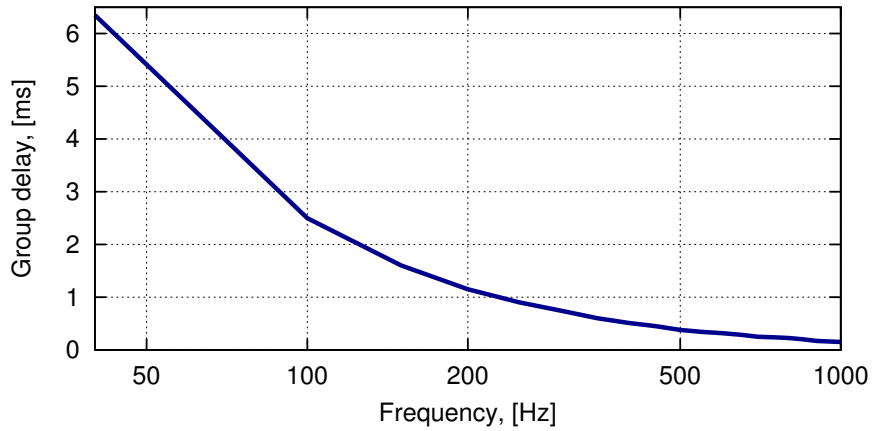


Figure 4.25: Experimentally measured group delay through PT sample for varying frequencies.

speed protective relays are used to detect faults which occur as a result of these noise frequencies which deviate in phase and magnitude with respect to power-line frequency. These noise frequencies vary from hundreds of Hz to a few kHz. The relays make a decision about the severity and location of fault based on the properties of the signal; such as phase, magnitude of voltage or current signals, impedance etc. The faster a fault is detected, lesser time it takes for the signal to restore its fault-free steady state [93].

Signals passing through PT are susceptible to group delay as discussed in the previous section. Measured group delay pattern for frequency range 40Hz to 1kHz shows an exponential decay, Fig. 4.25. For 60Hz signal, delay is approximately 5ms, which progressively decreases to less than 1ms for frequencies above 200Hz. Eventually, as we increase the transient frequency beyond 1kHz, the delay time reduces to few microseconds. This behaviour of the transformer enables fast and accurate detection of disturbances while operating at line frequency.

In our time domain simulations, we subjected the PT model to low frequency and high frequency signals, to demonstrate this lag. This delay was likewise observed when PT was treated with the real-time *PSCAD* signals just as shown for the simulated PT model. For a 5s long input with high frequency glitch occurrence at 2s, Figure 4.26 shows a noticeable lag between the scaled down input to PT and the PT output in the low frequency component. This

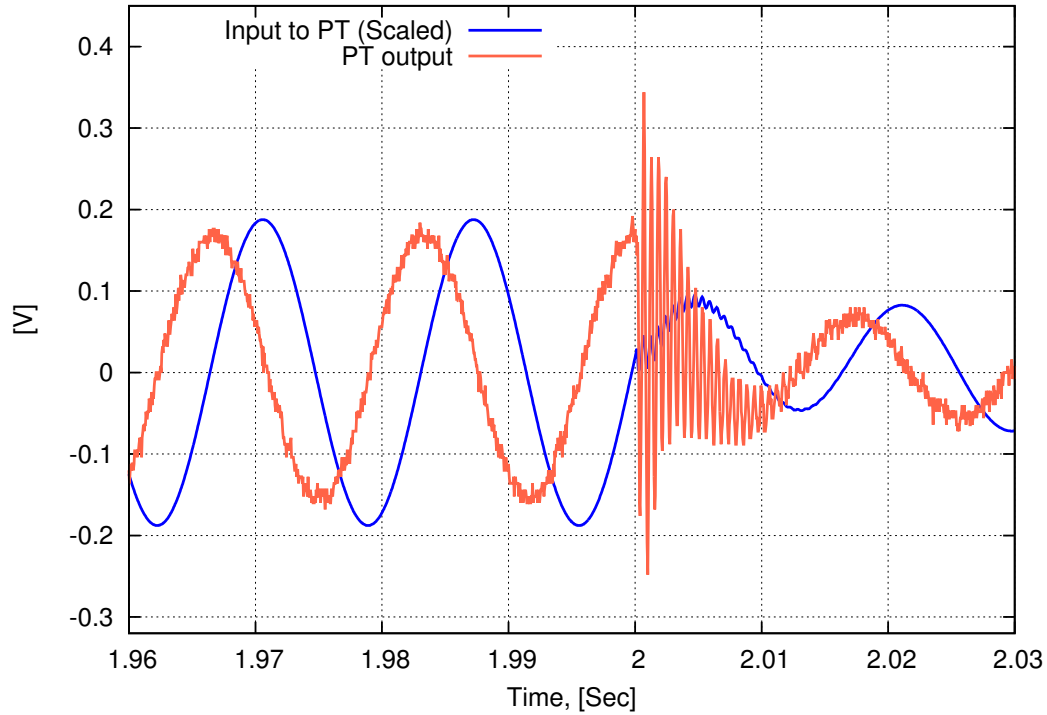


Figure 4.26: Experimentally observed group delay through PT sample for real-time faulty input signal.

lag is negligible when the PT encounters a high frequency glitch at 2s. Hence the glitch appears almost at the same time at the output terminal as it appears at PT's input terminal, making it instantaneously detectable.

4.3 Limitations of PT considering existing system conditions

The electrical equivalents and mathematical models established for PT are based on its operation at or near its resonant frequency. In our experimental work we noticed the following three important practical limitations related to PT operation that we need to keep in mind, since we use the PT in low frequency area of operation.

- Mechanical considerations
- Non-linearity and Hysteresis

- Material properties, ageing and effect of temperature

4.3.1 Mechanical considerations

A PT operates based on the principle of energy transfer through vibration. The vibrations in input and output sections may not necessarily follow the same patterns. Mechanical vibration has a non-uniform distribution over the dimension of PT [94]. The vibration pattern in the PT not only depends on factors like the frequency of operation and terminal load impedance but also on the structural constraints and device clamping that the PT might have been exposed to. We have observed noticeable differences in the PT performance when mounted on a test-bench table top and when held firmly onto a printed circuit board with a cable tie, Fig. 4.27.

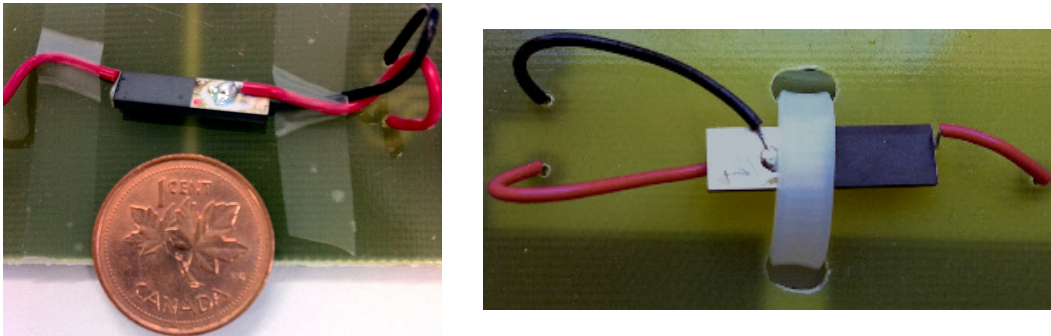


Figure 4.27: Photo of a PT size compared to a Canadian penny, held using cellophane tape (left), PT clamped on to a PCB using a cable tie (right).

Hence it is important to design an appropriate package and make electrical connections to PT without affecting its operation and efficiency. Having said that, considering one of the reasons of using a PT is lesser space occupancy, since its size is small as compared to a conventional board based electromagnetic transformer, Fig. 4.27, care must be taken to confine the size of the package used. There have been inventions related to PT device being packaged in moulded cases with conductive adhesive for external electrical connections, use of conductive sheets and spring terminals, latched upper and lower cases for piezo body etc. One improved armoured case has been discussed in [95], which comprises of a moulded package with reduced thickness and with projections to mechanically support the piezoelectric element. The

thickness reduced moulded package with projections is capable of applying an elastic force on the piezo element such that the element is confined within the package walls but still separated from them. These projections also provide an avenue for wirings to make electrical contact with the element.

Another method discussed in [96] suggests a mechanically compliant apparatus which relates to mounting PT onto a PCB with use of miniature conductive springs. It describes a configuration for Rosen-type PT operating in one-lambda length resonance mode as an example, with coil springs attached to at least one minimum displacement node of PT, to minimize mechanical stress on it. The output electrical connection is made at the maximum displacement point which is extremely sensitive to mechanical dampening.

A later invention [97], describes an integral construction of the housing and the lead frames for the PT which enables easy contact with PT and resilient support to PT at the same time. This design is suitable as an alternative to the simple PCB design with soldered wires that we used in our experiments, especially for mass production to avoid repetitive wire connections and breakage of wire contacts at solder points. The housing consists of an upper and lower section with a protrusion to support PT, and lead frames made of conductive elastic material to be in contact with PT electrodes. These sections couple with each other with a hook and snap arrangement.

Designing a system taking into account all these factors will be a significant step towards integration of sensing devices. Since we only harness the low frequency properties of PT, we need not take into consideration the wavelength vibration modes while designing a clamping structure. Nevertheless, the sensitivity of PT with respect to mechanical vibration is higher in the low frequency region, which is our area of application and hence a resilient housing that resists external unwanted vibrations, which affect the PT performance, is essential.

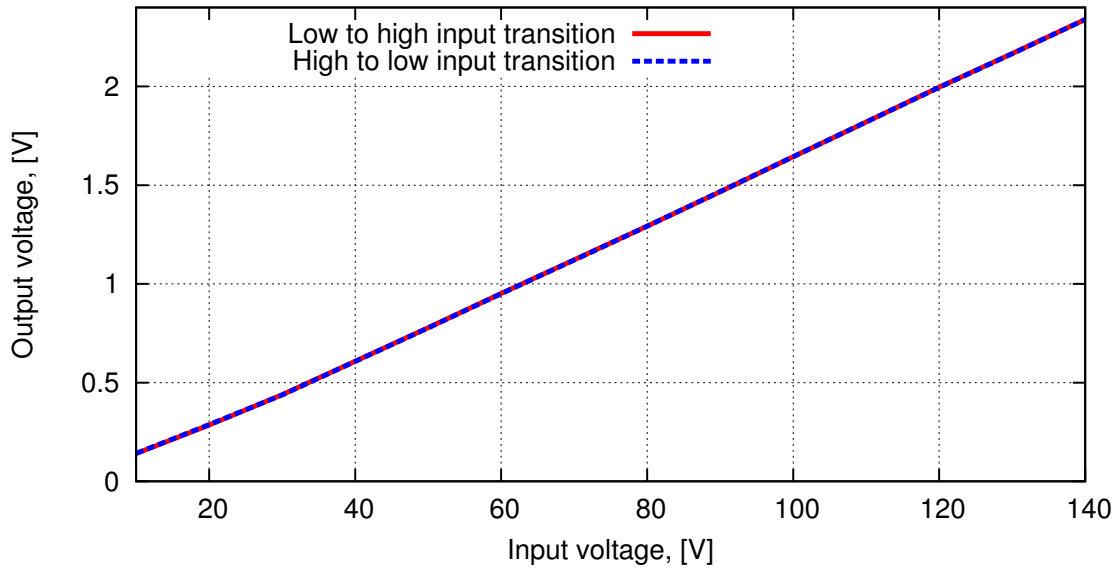


Figure 4.28: Negligible hysteresis observed during experimental measurements at power-line frequency.

4.3.2 Non-linearity and Hysteresis

Piezo material is inherently non-linear mainly due to the domain orientations in the piezo materials which cause the dielectric non-linearities. The piezoelectric non-linearities are attributed to the dependence of piezoelectric constants on polarizations, electric field components and mechanical pressure. The elastic non-linearities originate from the fact that excessive mechanical stress on PT may cause depolarization of its material and may alter its dielectric and piezoelectric properties [74]. In low frequency mode, we demonstrate the PT linear behaviour and hence incorporating a correction factor for non-linearity is not required. However, in the higher frequency and high input voltage region, hysteresis at the PT output becomes visible.

Hysteresis is a common phenomenon in smart actuators like piezoelectric transducers, which may act as an additive disruption in the dynamics of the device. The effect of hysteresis is considered to be a combination of both amplitude and phase distortion [98]. We observed a hysteresis specifically with respect to PT output magnitudes for input variation from low to high voltage and from high to low voltage. Although the difference in magnitudes is almost negligible, Fig. 4.28, it could be measurable at high frequencies. We partially eliminated this

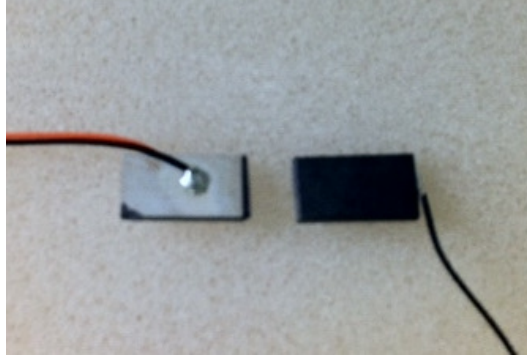


Figure 4.29: Photo of PT with mechanical defect.

effect by using two PTs in a differential configuration.

4.3.3 Material properties, ageing and effect of temperature

The PT's performance is fundamentally limited by the material itself, by its mechanical strength and depolarization due to heating and constant exposure to stress and strain [33]. The material's thermal limitations and maximum capacity to withstand stress and strain may limit the PT functionalities. During the energy transformation process between primary and secondary sections of the PT, the PT undergoes mechanical and electrical losses that generate heat within the device. The equivalent PT losses are proportional to the quantity of heat produced in the PT body. The PT can dissipate some amount of heat produced in its body which reduces the increase in temperature. This ability of heat radiation is proportional to PT's ratio of surface area to volume. This makes the rectangular cross section more efficient with respect to heat dissipation than a circular cross section for a PT.

Due to low thermal conductivity of PT material, constant exposure to high voltages may cause overheating of the material which eventually leads to depolarization effects if the temperature inside the PT exceeds a critical level. This critical temperature determines the operational limit as the PT must be operated below the Curie Temperature (T_C) to prevent permanent damage to the device. This temperature limit is typically between 150°C to 250°C for most PZT ceramics, at which point domain rotation begins, long before the actual T_C of about 300°C,

due to the combined effect of high temperature and electric field [99]. Typically at resonance, the piezo operating parameters remain almost constant in the -40 to $+150^{\circ}\text{C}$ range. Since we are operating at low frequencies, this range will almost never be exceeded but cannot be ruled out in case of faulty signals that cause power-line frequency signal to be intruded by high frequency transients. Practically, this can be confirmed only with use of devices like the thermographic cameras.

Temperature change may also lead to thermal stress, which causes the shift of the optimum operating point for the PT even below the threshold for mechanical failure and T_C , making it sensitive to the slightest change in operating conditions [77]. Exposing our experimental PT to high voltages constantly especially near resonance, made it mechanically sensitive near the junction of input and output sections and caused it to break into two with just a single tap, Fig. 4.29. This was one case of mechanical defect observed during our experiments. Although the exact cause of this breakage could not be established conclusively, since the PT broke exactly at the centre, the reason can be attributed to degraded sensitivity at the point of maximum stress within the piezo.

Device degradation due to natural time evolution, called ageing, which causes a drastic decline in the functional performance of the material with time, is another factor we have to take into consideration. This is caused by the constant realignments of domains within the material to form more stable configurations [100]. Hence, it is important to quantify variations in performance of a PT in the application field over longer periods of time.

4.4 Summary

Evolution of FEM techniques used for PT design has led to experimentation with varied structures without actual manufacture processes. We discuss one such simple model in *COMSOL* in this chapter, which incorporates both electrical and mechanical properties. We recorded simulation results using this model for eigenfrequency analysis, frequency response of the PT

for different applied inputs and time-based PT responses. Based on these preliminary studies, we demonstrate the effects of PT dimension, material, frequency of operation and amplitude of stimulating voltage input on its electrical output.

Following the simulation results, we present an experimental analysis in this chapter. Rosen-type piezo ceramic transformers from ‘Fuji Ceramics’, with different dimensions and made to resonate at different frequencies, were used for experimental purposes. All the devices, instruments and methods used for actual PT measurements are illustrated in this section. The two connection types used, single-ended and differential, are discussed along with their characteristics.

In order to test the PT with real-time faulty signals, it is important to have an elementary understanding about types of faults. We discuss faults specific to 3Φ power systems to identify nature of these faults. Single tone PT measurements with predefined signal frequency and amplitude are recorded. Response of the PT to varying signal frequency with a constant amplitude both in power-line frequency region and near resonance is observed. These responses were found to be in agreement with the simulated results. The PT behaviour in the low frequency region can be mapped into a linear relation between input frequency and output voltage. Similarly, for a fixed signal frequency, the PT outputs for a varying signal amplitude were noted to observe effect of high voltages on the PT.

Being a high output impedance device at low frequencies, it was concluded that the PT does not yield accurate results without an impedance matching network or an intermediate buffer circuit between the PT and loading circuit. The loading effect deteriorates the PT’s resonant as well as low frequency behaviour. With corrective measures, the effect of externally connected load values on the PT output was observed and plotted.

To be able to use PT seamlessly as an alternative to existing magnetic sensing technique, it is necessary to test it with real-time power signals. This real-time analysis with actual power system signals, was possible with use of signal generators in combination with power simulation software programs like *PSCAD* and *PLAYBACK*. Effect of time varying voltage

signals for the considered cases during normal and faulty conditions was recorded. The group delay measurements led to the idea of fast detection of high frequency glitches using PT while stepping them down.

Finally, certain drawbacks associated with using PT in our application are brought out in this chapter. Although the analytical and experimental results indicate promising future for piezo devices in power applications, effect of factors like external mechanical perturbations, temperature variations and material degradations pose some significant challenges in adopting these transformers. With suitable mounting designs and device manufacturing, taking into account the application environment, it is possible to employ PTs in high power systems.

Chapter 5

Modelling and Experimental Analysis – Hall sensor

Current sensing and measurement is required in relay systems to calculate quantities such as impedances. Current signals are also used for frequency estimation for protection and control functions performed by the relay. During 3 Φ solid faults, when all three phases are shorted to ground with zero impedance, pre-fault voltage values in combination with current values recorded at that time, help in fault diagnosis.

In power systems, large line currents in order of kA are scaled down to few amperes, by current transformers (CT). During normal operation, secondary rating of connected CT is matched to relay's nominal input current resulting in a stepped down value of 1A or 5A. This is mostly done by use of auxiliary electromagnetic transformers. Conventionally, this current is then converted to a voltage with use of sense resistors and further digitized for measurement purposes. The sensor chosen in this work as an alternative to resistive sensing for testing and analysis is Hall based MLX91205 integrated magnetic sensor. Whenever a fault occurs, changes in frequency and amplitude of voltage signals are accompanied by a spike in current signals. Therefore, the current signal corresponding to a fault condition simulated in *PSCAD* was recorded and treated with current sensor.

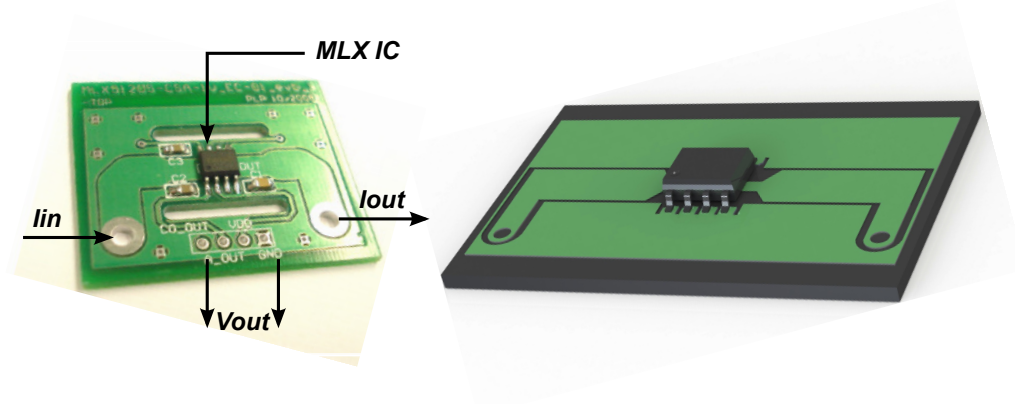


Figure 5.1: Photo of development kit used for measurements based on IMC MLX91205 IC and its 3D rendering showing narrow conductor width under the IC

5.1 Device under test

We experimented with the low field MLX91205 IMC sensor for our application. The IMC 91205 Hall sensor is fabricated with conventional CMOS technology with an additional ferromagnetic layer. This IMC layer is used as a magnetic flux concentrator which provides a magnetic gain of about 3 to 6, to increase the output signal without an increase in the inherent sensor electrical noise. The MLX91205 is a SOIC8 packaged device suitable for surface mount PCB construction and miniaturization. In this structure, the measured current is passed either directly through a current track of the PCB located under the sensor, or the sensor is mounted at a given distance from a larger current conductor like a busbar. It is a simple device and provides an analogue output voltage proportional to the magnetic field generated by this current carrying path [101].

The set-up used in our experimental measurements is a development kit from *Melexis* [102], Fig. 5.1. It includes the IC mounted on a PCB with signal tracks for current measurement. It has slots on either sides of the IC to insert an U-shaped magnetic shield to concentrate the magnetic flux density seen by the IC. This sensor is sensitive and linear in the frequency band of DC to 100kHz, and has a response time of 8 μ s. It has an operating range from -40°C to 125°C and requires a DC power supply of 5V. It is possible to increase the magnetic field

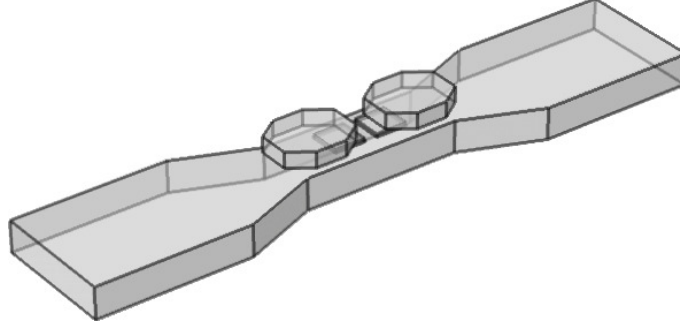


Figure 5.2: 3D *COMSOL* model representing the Hall-effect based IMC concept showing the conductor with lateral Hall elements and two hexagonal magnetic concentrators.

density with the same current magnitude by narrowing part of conductor that passes right below the chip surface. This action increases the current density in the narrow portion underneath the IC and generates higher magnetic flux density around it, thus it increases the field magnitude as seen by concentrators. The IMC sensor makes use of this concept, and therefore further increases the sensitivity of the sensor.

This device, along with the Hall elements, also incorporates offset cancellation circuitry, current source, chopper stabilized amplification circuitry and parameter programming capability [103]. The inherent drawbacks of IMC technology related to process and material are overcome by an appropriate sensor architecture which varies with the requirements of the application [104] making it a highly accurate technology. Along with the actual measurements using this IC, we also modelled the IMC principle in *COMSOL*. Using the model we demonstrate the effects of current magnitudes, direction and dimension of the device on the output result.

5.2 *COMSOL* model and effect of real-time *PSCAD* current signals

We use a Copper conductor in the model to represent the current carrying path with Hall elements and two hexagonal highly permeable structures (we used Iron from the in-built Materials

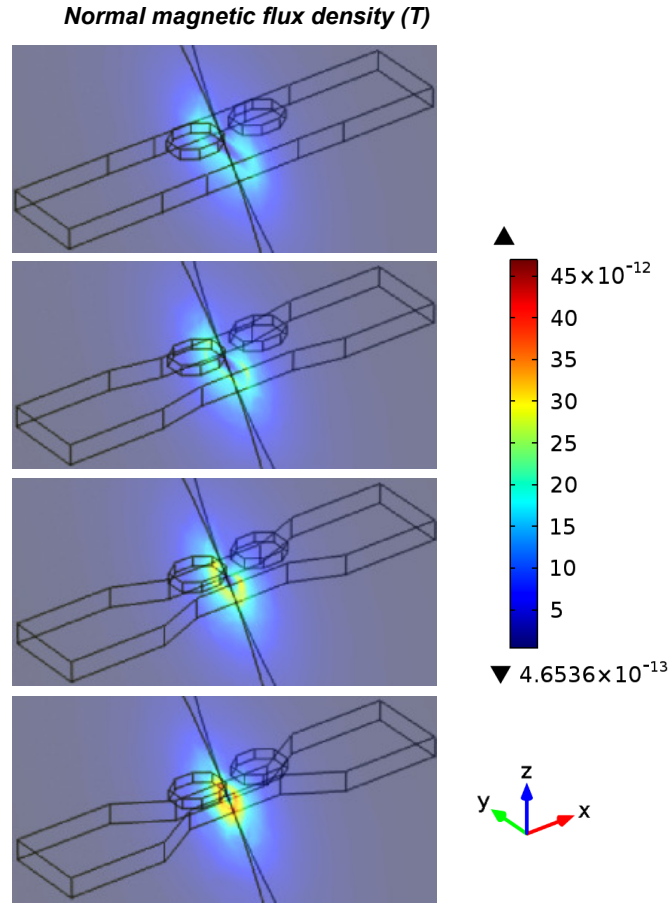


Figure 5.3: Simulated effect of varying width of the part of the conductor under the Hall elements, on normal magnetic flux density distribution in the *COMSOL* model.

library in *COMSOL*) to represent the concentrators, Fig. 5.2. This assembly is modelled to be placed in an air surrounding. The ‘Magnetic Fields’ (mf) physics module was used for the simulations. Effect of 5A current through the conductor was first observed in terms of flux distribution in the assembly.

The effect of current flow through the conductor path under the IC and dimension of this conducting path has an effect on the magnetic field seen by the Hall elements within this IC. As mentioned in the previous section, the IMC sensor makes use of this principle to increase its sensitivity to low fields. We demonstrate this effect by varying the width of the part of conductor which lies below the concentrators and Hall elements in our *COMSOL* model using a parametric sweep function and 3D plots. Although the output recorded is not in form of

an output potential, the magnetic fields observed in the model are evidence to this effect. For the same current passing through the conductor, the normal magnetic flux density observed in the narrow region between the concentrators around the conductor increases with decrease in width of that conductor in this narrow region, Fig. 5.3. Increase in the width also increases power dissipation and self-heating of the conductor.

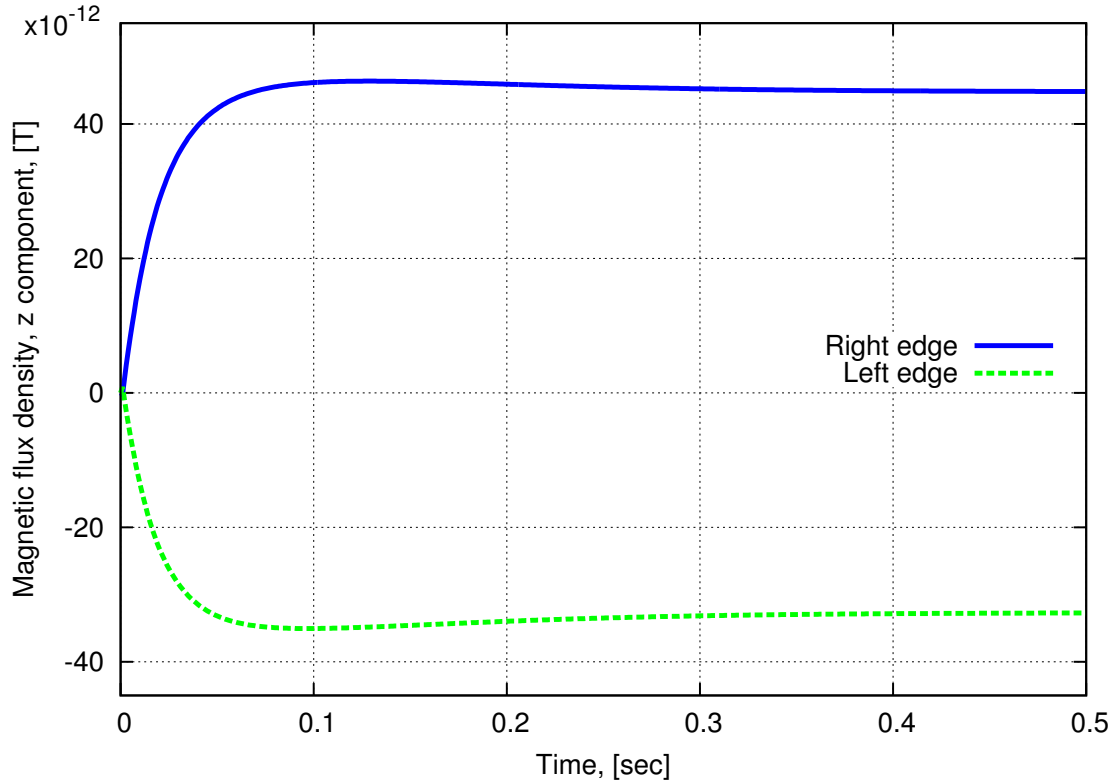


Figure 5.4: Simulated z component of magnetic flux density variation observed between the hexagonal concentrators along the two facing boundaries in the model.

Since the material used for the concentrators in the IMCs and in our model has a high permeability, the concentrator collects all the flux lines in its vicinity and focuses them on the Hall elements. Along with the flux around the conductor due to the current it carries, we also observe flux lines parallel to the conductor. The concentrators make part of these flux lines pass through the Hall elements underneath, as for these elements, flux appears to be going up on one side of the concentrator and going down on the other side of the concentrator. For a current of 5A through the conductor in our model, we observed the perpendicular component

of this magnetic field to be strongest near the gap between the concentrators. The flux recorded along both sides of the concentrators facing each other in the gap was opposite in polarity to each other, Fig. 5.4, which indicates that flux lines travel up on one side and down on the other side. In actual implementation, this field gives rise to a potential difference in the gap and hence a difference in magnetic field seen by two Hall elements. The sensor output voltage is now generated by difference in output voltages produced by these two Hall elements.

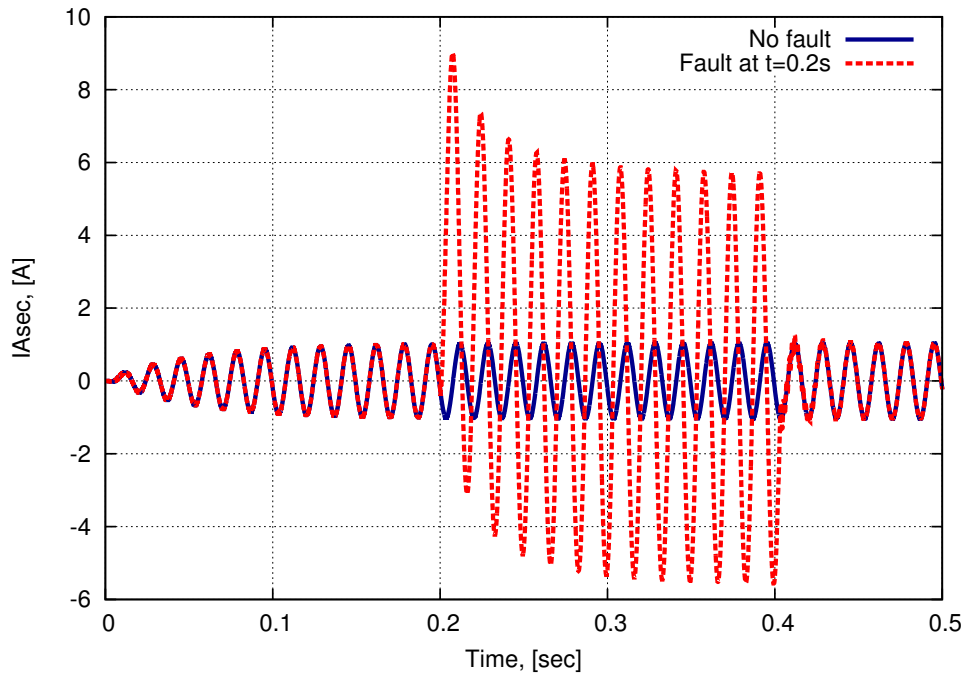


Figure 5.5: Time-domain plot of secondary current exported from *PSCAD* power system model applied to Hall model in *COMSOL*, for fault and no fault condition.

The sensor's upper limit for measurable current level is determined only by the physical construction of the device, since the output voltage is dependent on conductor size and its distance from sensor. This is a useful property in our application since, during fault conditions, continuous current levels may easily go up more than three times the normal levels. Lower currents up to ± 2 A can also be measured by increasing magnetic field via a coil around the sensor. The sensitivity is further increased by adding a shield around the coil and sensor set-up.

We observed the dependence of time varying current signal passing through the narrow

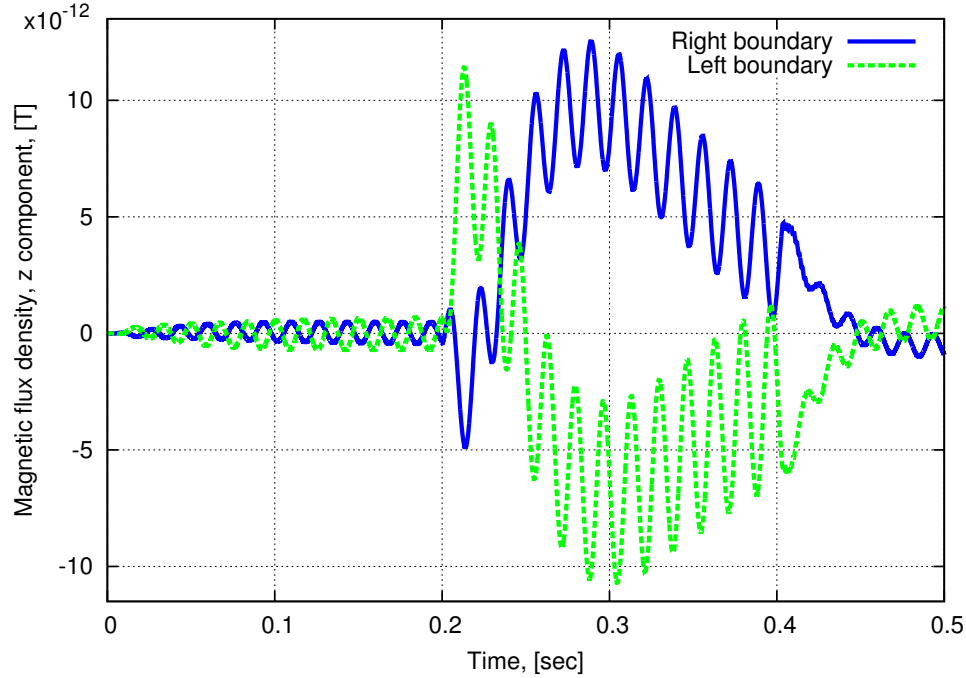


Figure 5.6: Time-domain plot of z component of magnetic flux density recorded on concentrator boundaries facing each other in the gap, for time varying input current.

conductor upon magnetic field density around the conductor in our model. Figure 5.5 shows the applied current input exported from *PSCAD* corresponding to case 2 AB-g fault condition compared with a no-fault condition current. The faulty signal shows fault occurrence time as 0.2s and duration of fault as 0.2s. During this time, magnitude of current rises more than four times as compared to no-fault current signal. We use ‘Time Dependent’ study in *COMSOL* to probe the gap boundaries of concentrators to observe magnetic field distribution. The perpendicular components of magnetic field recorded on the boundaries of concentrators facing the gap in which Hall elements are placed, follow a similar sinusoidal trend as that of current, and varies from minimum -5pT to maximum of approximately 13pT , Fig. 5.6. During the fault, magnetic field increases more than five times as compared to the normal fault-free conditions. The flux density on each of the faces is opposite in polarity to each other.

In the actual IMC circuit, this magnetic field is seen by Hall elements within the IC and corresponding output voltage is generated. Due to the increase in strength of magnetic field during fault times, an analogous potential which indicates presence of fault is generated. Based

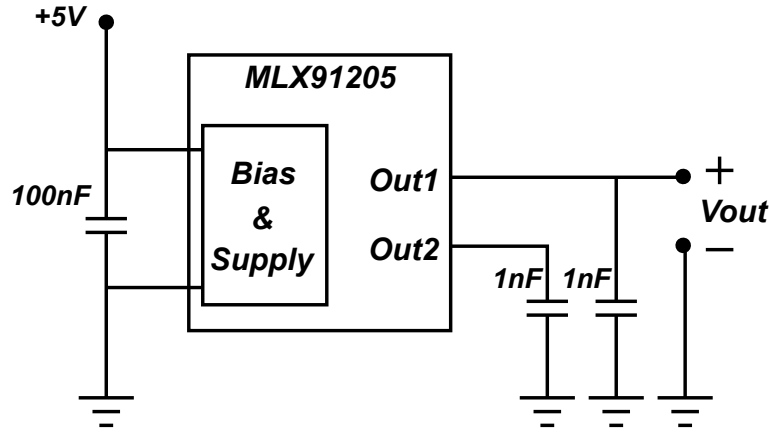


Figure 5.7: Schematic diagram of direct single-ended connection for the open loop MLX current sensor.

on the characteristics of this *Melexis* sensor and the output potential, the actual current values will be estimated in power system applications.

Due to experimental limitation, we could not test the actual IC with real-time *PSCAD* produced signals. However, we tested the MLX91205 sensor in its open loop configuration for a single-ended direct output with bypass capacitors connected for a reliable operation, Fig. 5.7. Our measurements with the MLX device for constant current inputs resulted in a set of plots that show effect of change in current amplitude and frequency on output voltage. We compared these results with the magnetic field trend observed in the *COMSOL* model. Figure 5.8 (top) shows increase in normalized output voltage with increase in current input for the MLX sensor. The magnetic field (z component) in *COMSOL* simulation follows a similar trend with increase in current. When tested for increasing frequency and for a constant current input of 1A and 5A, Fig. 5.8 (bottom), change in output voltage was relatively constant with a decrease of about 5mV for the MLX sensor. *COMSOL* plot of corresponding magnetic field shows a decreasing trend too with much lower magnitudes and a different scale of measurement.

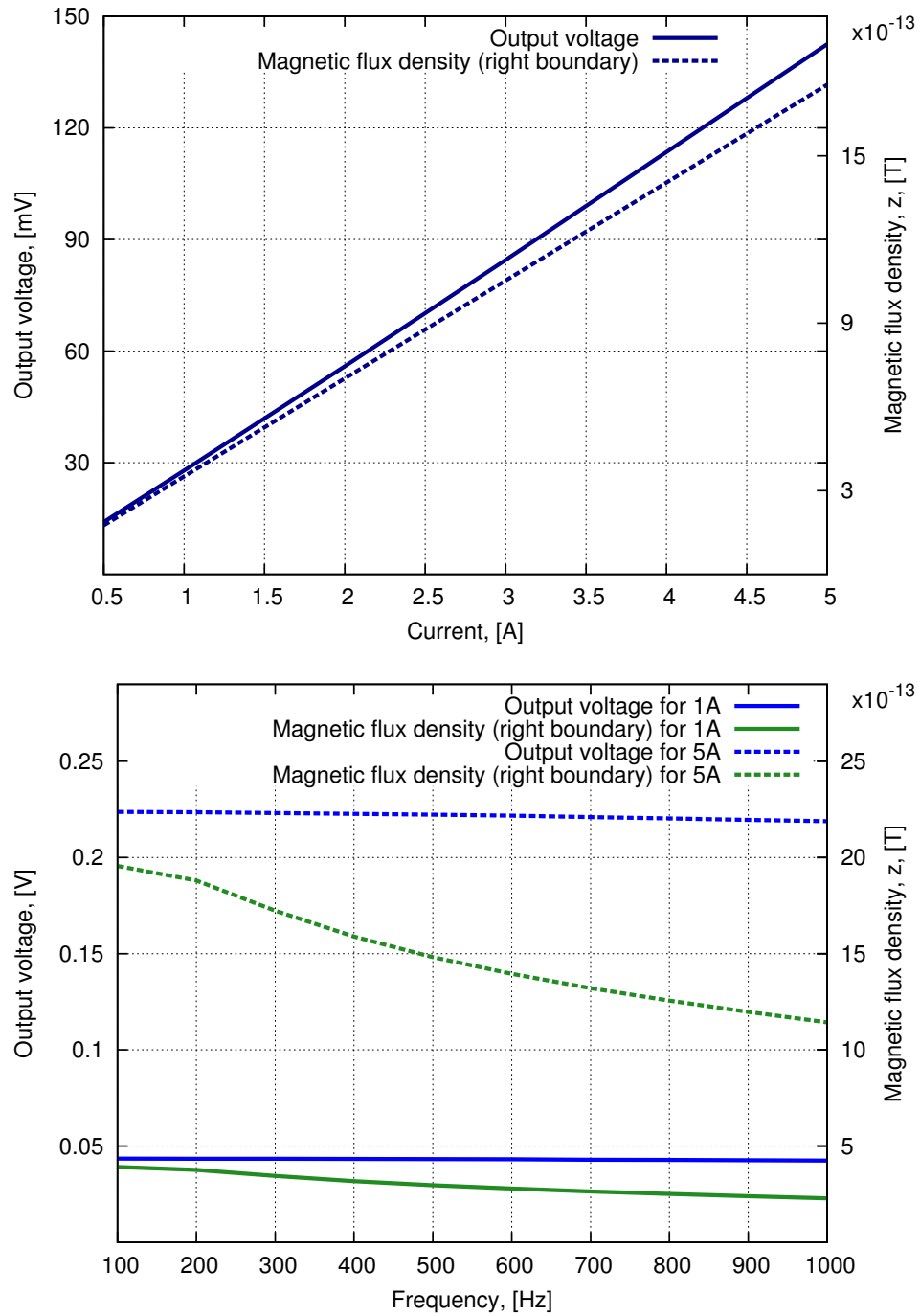


Figure 5.8: Experimentally recorded MLX output voltage for increasing current, flux variation with current in *COMSOL* model representation (top), Experimental MLX frequency response, recorded flux change with frequency in *COMSOL* Hall model representation, for 1A and 5A (bottom).

5.3 Other considerations in IMC based Hall sensing

Techniques like narrowing the conductor path below the current sensing IC discussed in the previous sections help increase the operational magnetic field range for the sensing IC. Using a shield around the sensing circuit helps to reduce effect of stray external fields and increase the signal to noise ratio of the sensor. Soft magnetic materials like Nickel and Iron alloys are usually used for shielding purposes. Another method to cancel out effect of stray fields is placement of two sensors very close to each other. Assuming that the field seen by both sensors is homogeneous, this set-up not only increases the output signal strength but also eliminates effect of noise-inducing external fields on both sensors [101].

Considering that application of this sensor is in a power system environment, there are certain parameters that have to be taken into account to make sure they do not prove to be drawbacks in the sensor's operation. Some of them are listed below;

1. The main drawback of this sensor as compared to the existing transformer and resistor combination is that it requires an external power supply. Although the supply requirements are usually small, typically $\pm 5V$, the external source has to be stable and regulated.
2. The modern Hall ICs consist of a DC offset cancellation circuitry. However, the dynamic stress and temperature variation in a high power environment usually demands need of a system calibration or a 'look-up' table [105]. Usually dynamic offset cancellation techniques incorporated in ICs help deal with thermal and mechanical stresses.
3. We have not experimented with real-time signals, but phase shift through the sensor at lower power-line frequency range may be distinctly noticeable and may cause errors in measurement. This aspect has to be verified and taken care of before actual field implementation.
4. The system temperature range and behaviour of the sensor in this range have to be clearly specified and understood to ensure no damage to the sensor and to maintain high accu-

racy levels.

Current sensing and metering is required in almost all the modern industrial and electronic applications. Depending on the application specifications such as the input current range, the desired steady state, dynamic accuracy and cost estimations, a number of different techniques for sensing current are available. By providing electrical isolation and an accurate and low cost solution, open loop Hall effect sensors prove to be an informed choice for use in many of these applications [12]. It certainly opens a new set of possibilities in our current sensing system.

5.4 Summary

This chapter begins with an introduction to the importance of current sensing in power systems as an integral part of sensing system. There are cases in relay operation when voltages at all phases become zero and the only alternative to gauge the power levels is to measure the phase currents. Current metering is also useful for impedance calculations, off-line fault analysis and records. These registered current values also have to be converted to suitable voltages to be applied as input to ADC and the following circuitry for real-time processing. Hence we incorporate current sensing in our design as a substitute to existing resistor-based method.

The principle of magnetic concentrators and variation in width of current carrying path under the concentrators, to increase seen magnetic flux density, is demonstrated using 3D modelling in *COMSOL*. We compare the behaviour of this model with the actual sensor measurements for factors like effect of varying current amplitudes and frequency response. We also see the effect of fault current on the model which results in increased field magnitudes.

Chapter 6

Signal processing system

In a typical relay system, as described in Chapter 1, the sensed analogue voltage and current signals are converted to their digital equivalent values. These signals are then treated with digital filters to reject unwanted frequencies and the fundamental frequency components are accurately made available to relaying algorithms. The algorithms that constitute most of the intelligence in the microprocessor use numerical methods to estimate magnitudes, phases, impedances, frequency etc. of the input signals. The estimated values are then compared with threshold settings of the relay to detect presence of faulty operating conditions or any deviation from normal behaviour. Depending on the decisions made, and on the digital inputs available to the relay that correspond to the existing status of circuit breakers and isolators, the relay sends commands to the circuit breaker to operate when isolation of the faulty zone in power system is required [3].

6.1 Background and introduction

The development of various types of relays and protective devices has led to reduction in occurrence of faults. However, often, complete elimination of these faults at the time of their occurrence, is not economical. Hence the system is designed in such a way that the faulted portion can be located quickly and isolated from the rest of the system with minimum loss of

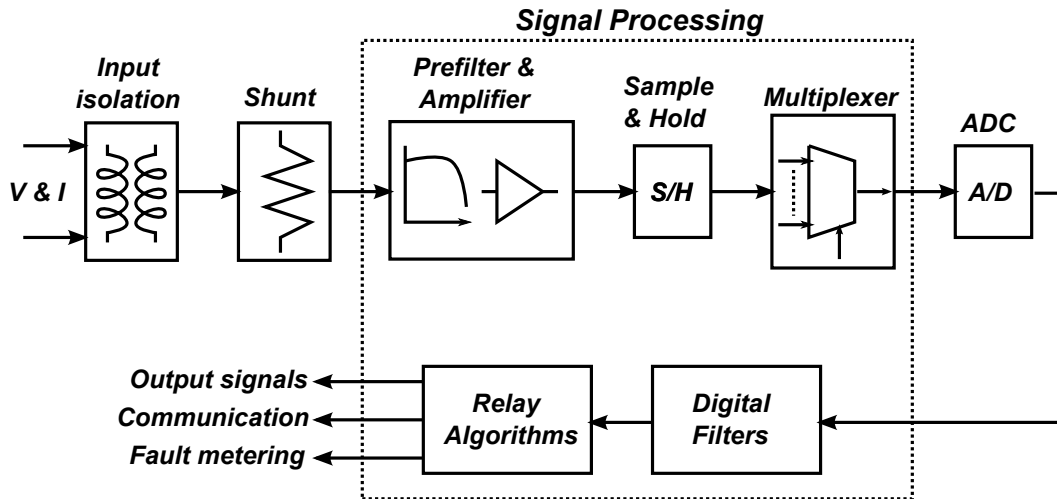


Figure 6.1: Block diagram of a signal flow representation showing steps involved in sensing, processing and decision making process in a digital relay.

power [106] for off-line diagnosis. Faults occur in power systems when insulation at the point of fault is momentarily subjected to voltage stress in excess of its dielectric strength which causes large currents to flow in unintended paths in the power system [107]. This can happen due to number of reasons, for example,

1. Failure in equipment due to insulation deterioration with age, accumulation of dust and dirt, design flaws, external hazards like fire and explosion etc.;
2. Human errors and mistakes in equipment handling;
3. Natural causes like wind, rain, lightening, floods, etc.;
4. Animals, birds, kites, air planes, rifles, etc.

Analysing the response of our sensing devices to faulty signals, to be able to detect these signals instantaneously, is a significant part of our work.

All the analogue input signals, healthy and faulty, are converted to their digital equivalents. Numerical signal processing techniques are applied to these digital equivalents before these signals are treated with relay algorithms. Similarly, various steps of analogue signal processing are involved even before input voltages and currents are converted to their digital forms. A

basic signal flow representation can be seen in Figure 6.1. After isolation and step down of voltages and currents and conversion of current values to their corresponding voltages with use of a shunt, these signals are passed through an anti-aliasing filter. This filter is essentially a low pass filter (LPF) used to restrict the bandwidth to avoid misinterpretation of high frequency components. These signals are then sampled and multiplexed to be fed to the ADC.

In this work, along with an alternative sensing and step-down device, we also introduce an integrated signal processing block which enables first hand, fast and accurate fault detection even before the information signals are subjected to relaying algorithms. For the voltage signal cases considered in this discussion, we are also able to broadly classify the fault causing conditions. The principles used in this discourse can be well expanded and an universal fault detection and fault categorization technique can be developed.

6.2 Fault detection technique

During a fault, redistribution of currents and voltages takes place and various properties of these signals like their magnitude, angle, frequency etc. undergo changes, sometimes momentary while sometimes persistent. The electrical transient, which may last for a very short duration but may cause extreme damage, is an outward indication of these changes in circuit conditions. These changes are characteristic to the type of abnormality in the system and in most cases form the basis of differentiation between types of faults which cause this abnormality. Even the relaying algorithms are extensively based on these changes and estimations are built. The different criteria based on which these faults can be detected and differentiated relative to pre-set normal condition thresholds are listed as follows:

1. Sudden change in magnitudes of the signals measured, overcurrent condition, undervoltage condition or a combination of both;
2. Phase shift between the measured signal and a reference quantity which is chosen to be a stable and reliable signal even during fault conditions [108];

3. Ratio between voltage and current signals, i.e. impedance, which is the electrical measure of distance of fault from the measuring point;
4. Comparison between quantities (especially current) at two ends of the equipment, e.g. transformer, bus bar, transmission line etc. where balance between incoming and outgoing values is examined;
5. Global comparison between signal phasors (vector with both magnitude and angle) measured at different locations across the power grid using a standard reference time signal from a GPS [109].

Most of the criteria discussed above is based on the real-time measurement of signals and their parameters. In our proposed fault detection scheme, presence of the electrical transient plays a significant role. Measurement of this transient has much in common with measurements of steady-state quantities except that its fleeting nature poses certain problems. Measurement of steady state voltages and currents also introduces errors but these usually can be made insignificant or can be compensated for; which often is more difficult to do in the transient environment. But these disturbances can be considered as periodic time functions with infinitely long period and hence can be evaluated using Fourier techniques [107]. In the following excerpt, we present one such system based on frequency analysis of real-time power signals.

6.3 Frequency spectrum of the input signals

A fault-free power-line voltage signal ideally contains only a pure 60Hz tone. In our work, in order to analyse PT behaviour with real-time signals, we used *PSCAD* software to synthesize, and an *RTP* simulator to experimentally recreate power signals. Thus, we have considered two cases in *PSCAD* as mentioned in Chapter 4. In each of the cases, we evaluated types of faults both between any two phases, and between phase and ground. When these signals travel

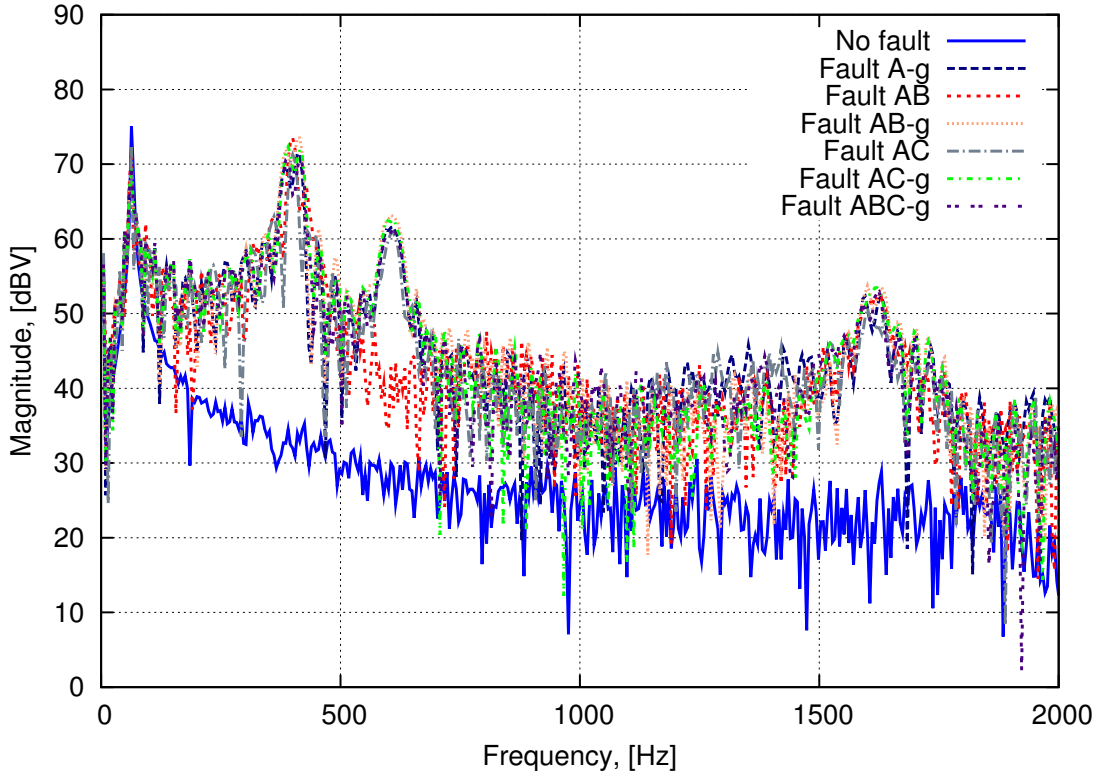


Figure 6.2: Frequency spectrum of experimentally recorded piezo outputs for case 1 fault condition.

through PT, they are stepped down and outputs are then treated with our signal processing system. The logic of our signal processing system is based on frequency analysis of the secondary piezo output signals, which enabled us to first, detect presence of a fault and then differentiate between no-fault and various other fault conditions.

For the analysis, we compare the Fourier spectrum of PT outputs in both cases. Figures 6.2 and 6.3 show a typical frequency spectra of piezo outputs for various fault combinations for the two cases. At each step we compare the experimental results with the simulated results obtained by processing PT model outputs. Here for case 2, Fig. 6.3 matches with the frequency spectra of piezo model outputs obtained in *COMSOL* simulation, Fig. 6.4.

Aside from the 60Hz fundamental tone, faulty signals additionally contain higher frequency components, which create frequency signatures that depend on type and location of fault in power systems. For instance, all case 1 fault signals contain a 400Hz frequency tone and ev-

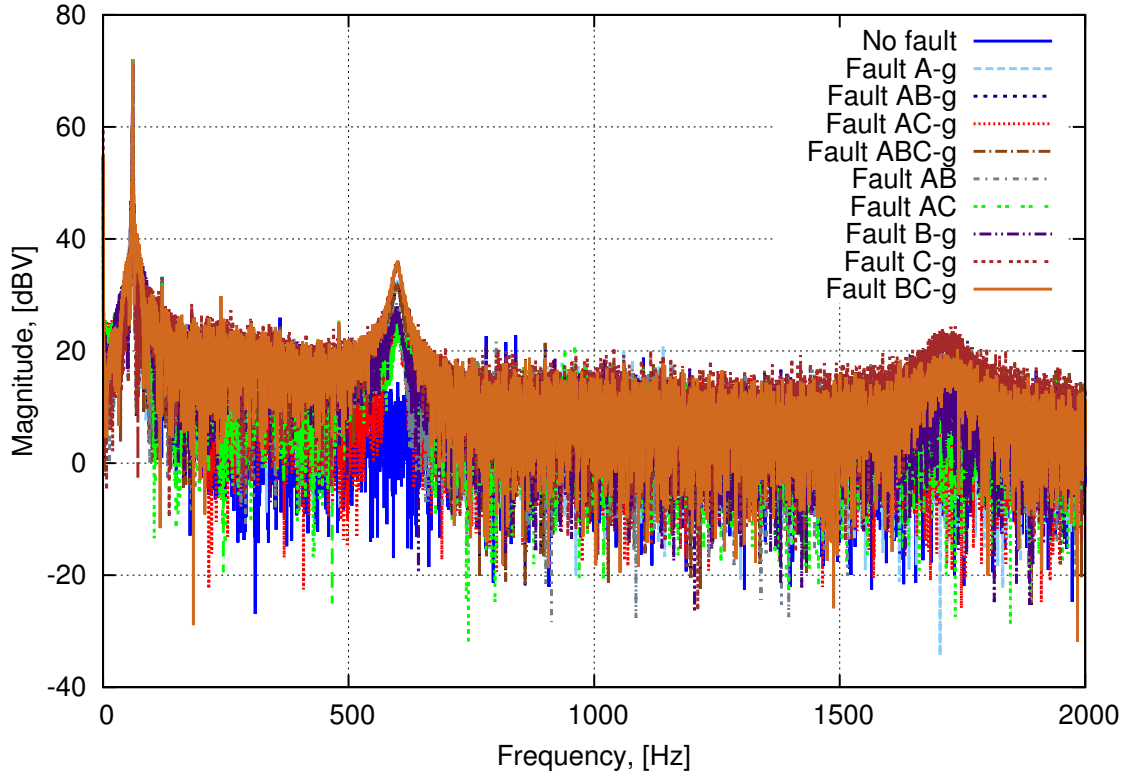


Figure 6.3: Frequency spectrum of experimentally recorded piezo outputs for case 2 fault condition.

ery fault, except fault AB, also contains a 610Hz tone, Fig. 6.2. Similarly, for case 2, each fault signal contains a 610Hz tone but this time the 400Hz tone is absent, Fig. 6.3. This aspect characteristic to the two frequency signatures is used to distinguish between case 1 and case 2 faults. Furthermore, there is a set of faults in case 2 which contains a 1710Hz tone. When zoomed around the 1710Hz tone, Fig. 6.5, three distinct magnitude levels are seen that correspond to three sub-sets of faults.

6.4 Signal processing and decision making system

Frequency composition of PT outputs decide the shape and magnitude of its time varying form. To be able to utilize distinct frequency characteristics corresponding to the faults, in order to discriminate between these faults, the time domain PT outputs have to be monitored and treated

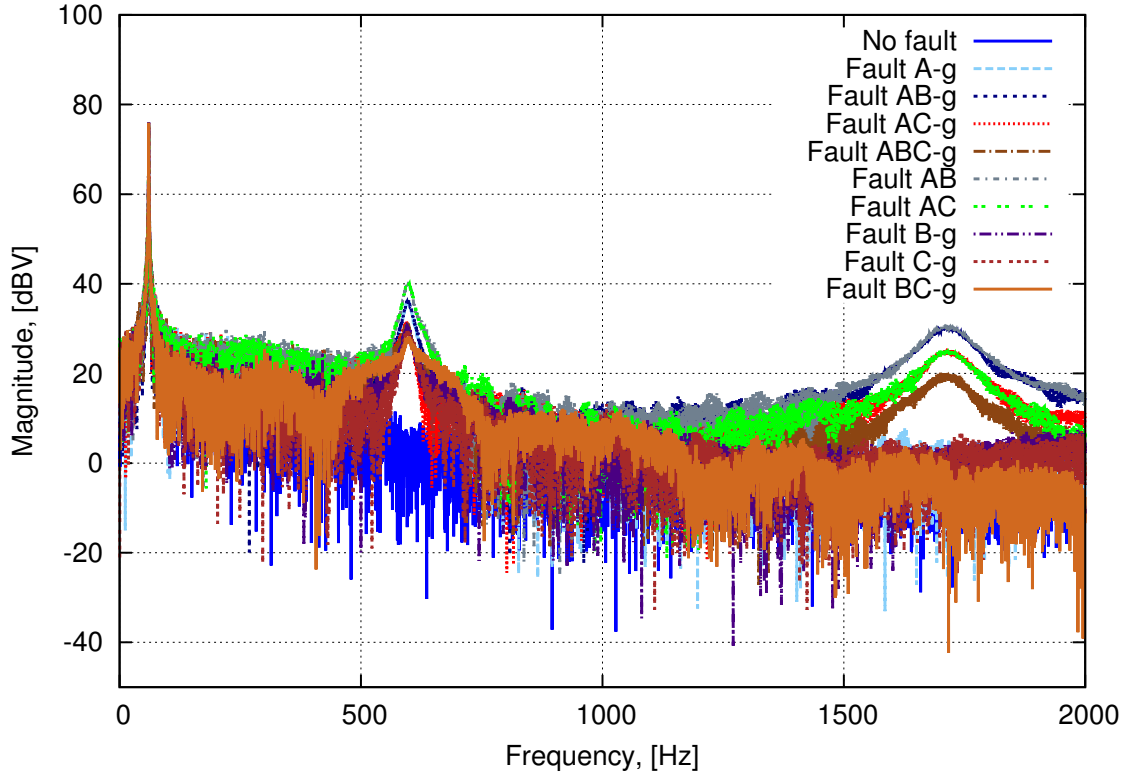


Figure 6.4: Frequency spectrum of simulated piezo outputs for case 2 fault condition.

with a signal processing system. Circuits like filters, comparators, amplifiers and logic gates are used to recognize deviating parameters in real time that facilitate detection of any kind of interruption in normal flow of operation.

6.4.1 Behavioural model and logic

In the description that follows, we present a behavioural circuit model of the signal processing and decision making method which forms a basic proof of concept prototype for our voltage sensing system, predominantly using SPICE and MATLAB. The processing steps were carried out on experimental PT outputs recorded by connecting the PT output terminal directly to the scope. As described in Chapter 4, this direct connection introduces a $1\text{M}\Omega$ load. Hence for purpose of one-to-one comparison with our simulated PT model, a load of $1\text{M}\Omega$ is added to the model before recording the model output signals.

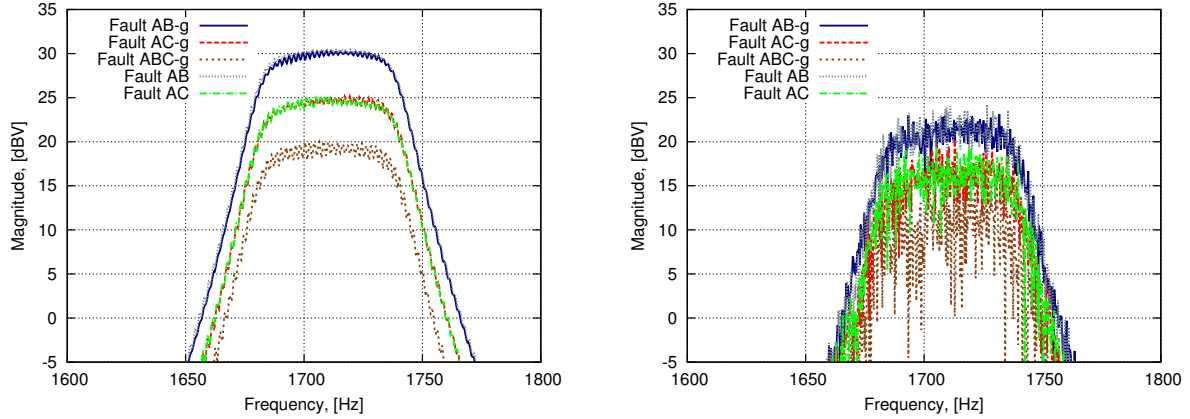


Figure 6.5: Zoom-in frequency spectrum of 1710Hz centred BP filter for case 2 fault condition, simulated (left) and experimentally recorded (right).

Since the capacitive load introduced by the scope becomes effective at higher frequencies, the experimental waveforms are distorted as compared to the simulated waveforms obtained from the model with a purely resistive load. For instance, the plot on the left in Figure 6.5 with simulated model results, clearly shows three distinct magnitude levels whereas the experimental plot on the right in Figure 6.5 does not have a well-defined separation between these levels. On the basis of modelling results, we suggest actual electronic devices, circuit elements and ICs for the final design.

The observed characteristics and frequency composition of piezo outputs for various fault combinations are thus translated into a fault detection logic which follows a truth table summarized in Figure 6.6. For the 2 cases considered, with this 6-bit logic information, we are able to,

1. detect occurrence of a fault;
2. discriminate if the fault belongs to case 1 type or case 2 type;
3. identify a particular phase-to-phase AB fault in the event of case 1 fault condition;
4. distinguish between four broad categories of faults, in the event of case 2 fault condition.

<i>MSB</i>			<i>LSB</i>			
6	5	4	3	2	1	Decision
X	X	X	X	X	0	No fault
X	X	X	X	X	1	Fault
X	X	X	X	1	1	Fault:Case1
X	X	X	X	0	1	Fault:Case2
X	X	X	0	1	1	Case1:AB
X	X	X	1	1	1	Case1:Others
X	X	1	X	0	1	Case2:ABC-g,AB AC,AC-g,AB-g
X	X	0	X	0	1	Case2:Others
X	1	1	X	0	1	Case2:AB,AB-g
1	0	1	X	0	1	Case2:AC,AC-g
0	0	1	X	0	1	Case2:ABC-g

Figure 6.6: Truth table of decision making system

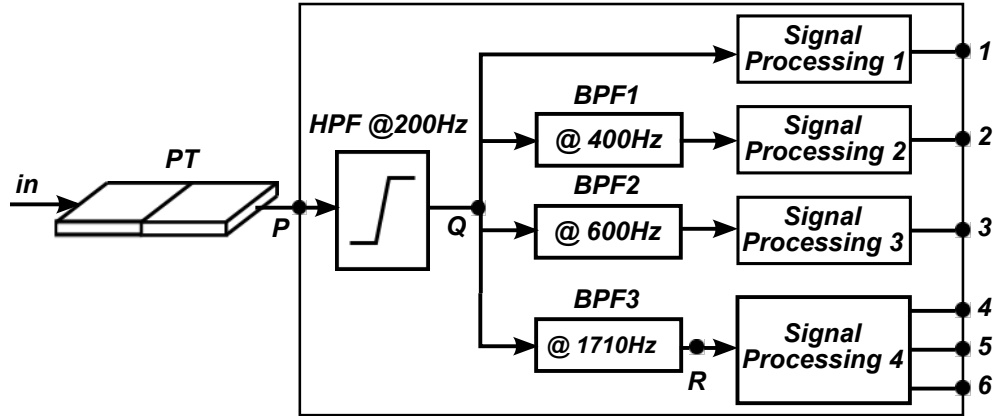


Figure 6.7: Behavioural block diagram of the decision making system.

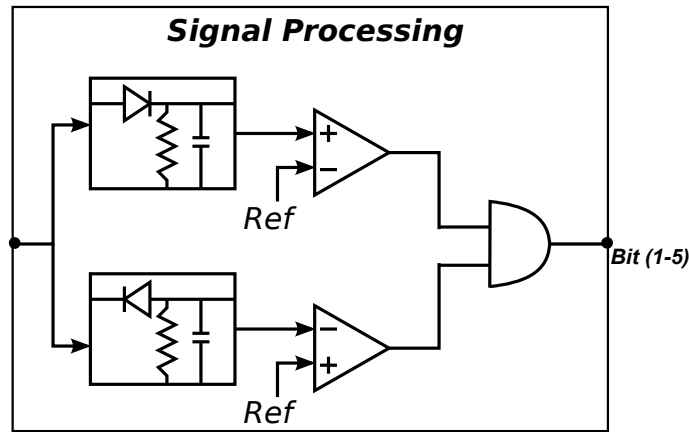


Figure 6.8: Behavioural block diagram of the signal processing system.

This logic forms the basis of our voltage sensing system as shown in Figure 6.7. Signal processing is a significant block in the sensing system, Fig. 6.8. For purpose of demonstration of this system flow, fault AB-g of case 2 is considered in the following explanation. We record and report results for phase A voltage signal in a typical 3 Φ power system.

6.4.2 PT output and High Pass Filter

Figure 6.9 shows PT output signal when it is subjected to a sinusoidal input with fault AB-g condition, node P in Figure 6.7. The overlapping simulated waveform is the output of PT *COMSOL* model subjected to the same fault combination and is slightly higher in magnitude as compared to the PT output recorded from the scope. The sinusoidal input is applied to PT

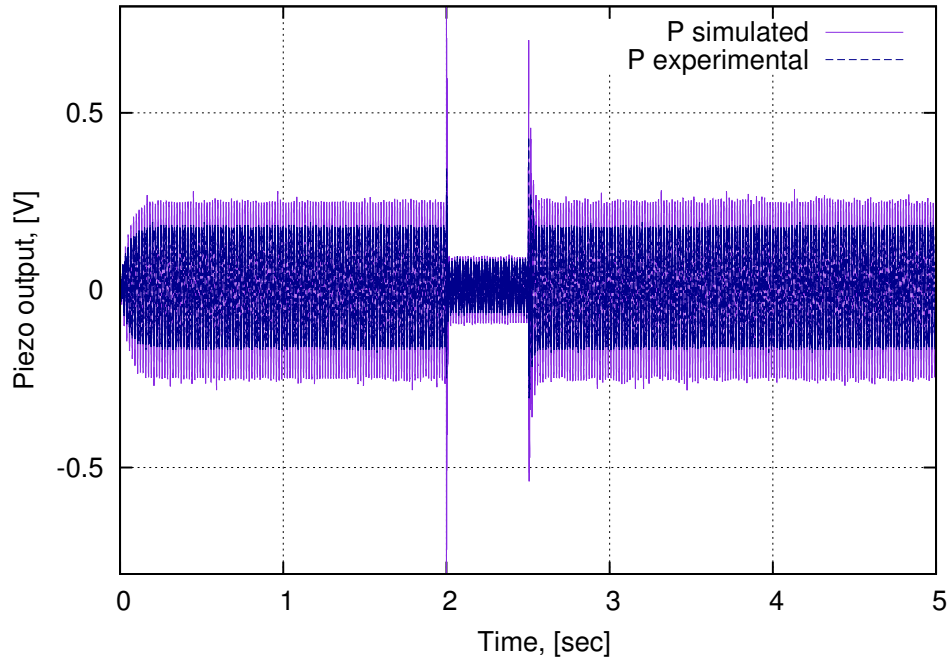


Figure 6.9: Simulated and experimental piezo output for case 2, fault AB-g condition.

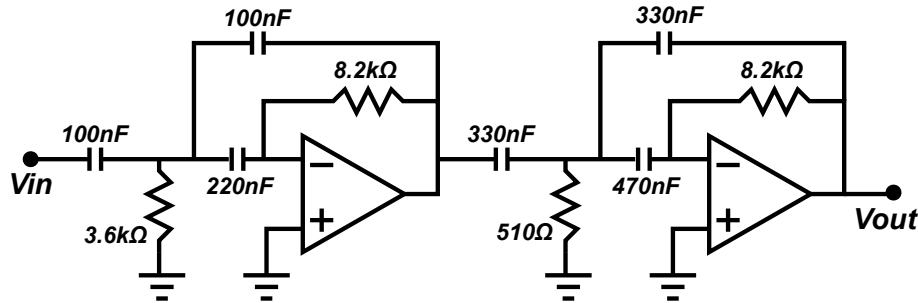


Figure 6.10: Schematic diagram of high-pass filter circuit representation.

for a duration of 5s. A fault between phases A and B is simulated using PSCAD and controlled to occur at 2s for a duration of 0.5s. During this period, the sinusoidal input and hence PT output is interrupted by high frequency glitches at the start and end times of fault and there is a dip in the overall voltage magnitude during the time of fault. The first bit of decision is based on presence or absence of the frequency components higher than 60Hz. Hence, to suppress the 60Hz component, PT output is first filtered by a high-pass (HP) filter.

To ensure suppression of the strong 60Hz component and hence to exaggerate the presence of higher frequency components, a model filter circuit with passband frequency of 200Hz was

designed. We used a two-stage filter circuit, with a passband gain of 0dB to develop a 4th order HP Butterworth filter, Fig. 6.10.

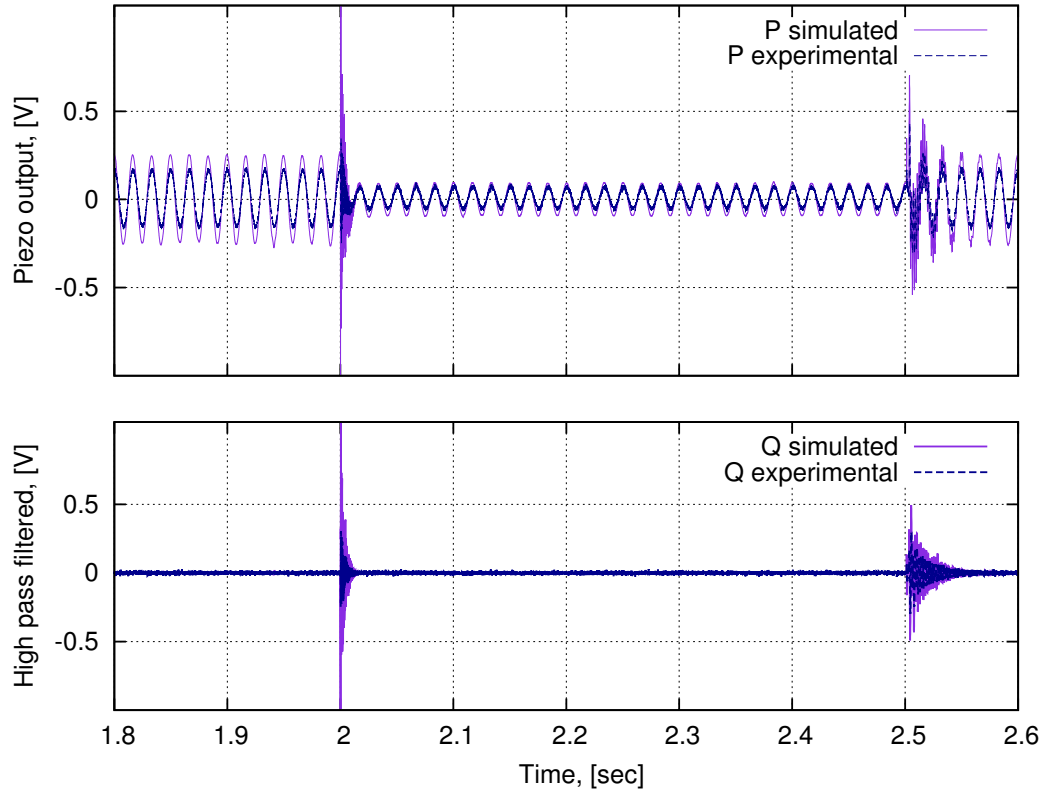


Figure 6.11: Simulated and experimental piezo output for case 2 (zoomed near fault region), fault AB-g condition (top), HP filtered output (bottom).

The time domain view of the filtered signal, Fig. 6.11, shows piezo output and the corresponding filtered output (node Q in Figure 6.7) for fault AB-g. The high frequency components pass through the HPF intact without any attenuation, with 60Hz component completely removed. The first bit of information in our logic is used to distinguish between a fault and a no-fault condition. Hence HP filtered piezo output is directly treated with ‘signal processing 1’ system to give bit 1 output.

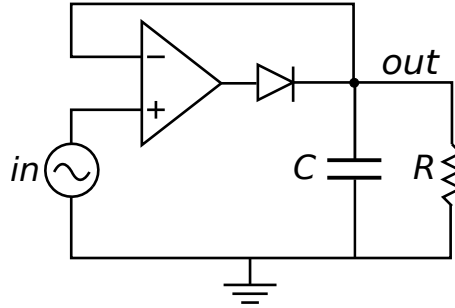


Figure 6.12: Schematic diagram of peak detector circuit based on the “ideal diode” circuit.

6.4.3 Envelope detection and comparator action

The first device that the HP filtered output encounters in the signal processing unit is a peak detector circuit, which primarily is used to extract the envelope of HP filtered signal. A peak detector is a circuit with a series connection between a diode and a capacitor wherein the capacitor retains the peak values of an AC signal, positive or negative, depending on the diode direction. With an RC combination, time constant can be varied for optimum tracking of the signal envelope based on the signal frequency.

Measured output voltage could be as low as a few millivolts, thus a standard diode is not a good choice for a peak detector. Therefore, in our circuit model we use an “active diode” circuit that effectively emulates an ideal diode [110]. A high gain buffer amplifier in combination with a simple diode is used to make the active peak detector circuit, Fig. 6.12. By placing a diode in the feedback loop of an amplifier, the diode drop voltage is divided by the ideally infinite open loop gain of the amplifier, which virtually eliminates this drop and makes it suitable for low voltages. The resistor and capacitor values of $R = 900\Omega$ and $C = 6\mu\text{F}$ enable optimum tracking of HP filtered output with a time constant of 5.4ms.

The peak detector circuit includes a low-pass (LP) filter to further remove high frequency ripple from the envelope waveform and for smoothing the final result. While doing so, the shape of the envelope needs to remain unchanged for accurate representation of transitions in the signal. Hence a filter with sharp frequency response with fast transition in gain between the passband and the stopband is needed. We use a 3rd order elliptic filter with a cut-off frequency

of 100Hz for this purpose.

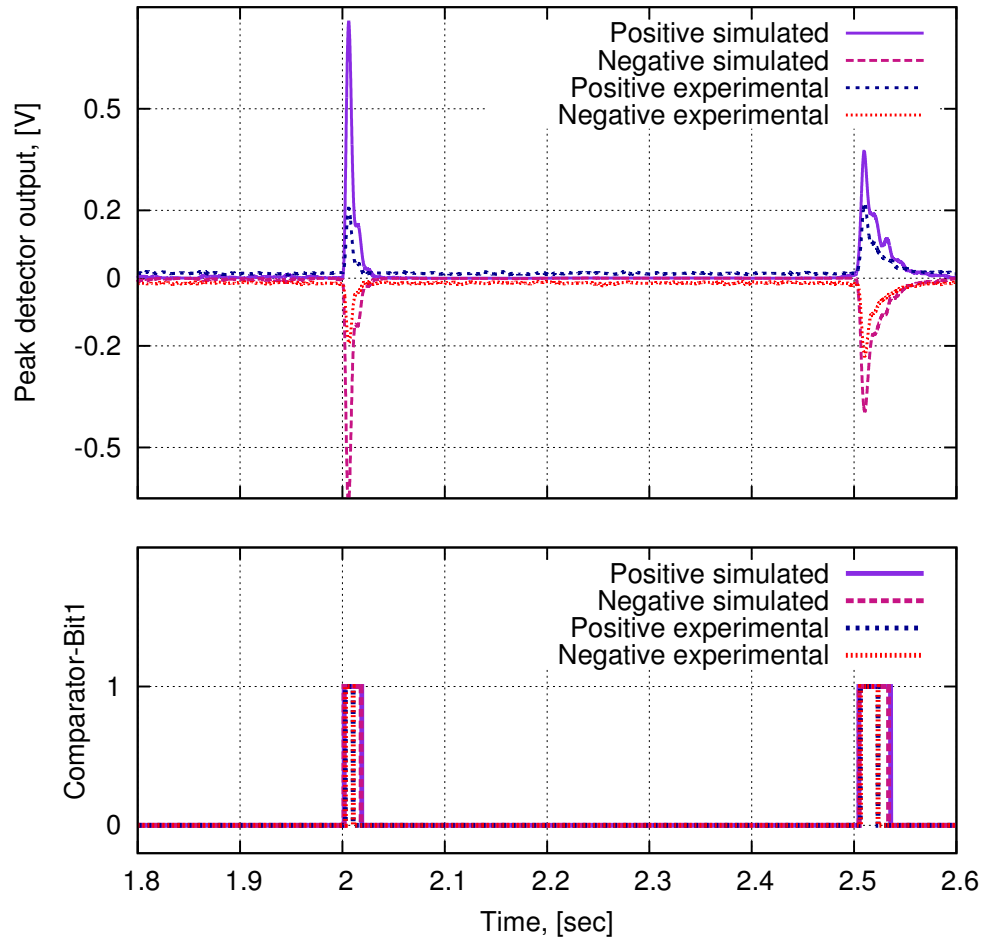


Figure 6.13: Time domain peak detector output signal (top), comparator output signal (bottom) for first bit of information (bit 1).

In order to detect both positive and negative voltage glitches, both positive and negative peak detector circuits are used. This signal operation results in waveform plotted in Figure 6.13 (top). Once both positive and negative envelopes are obtained, a simple comparator circuit is used to convert these envelopes to a digital form. The fact that the magnitude of PT output is higher during fault glitches as compared to its 60Hz component, is used to set the threshold reference voltage of the comparator. In an op-amp model of comparator, to detect higher amplitude in the positive envelope, the input signal is fed to the positive terminal with the reference signal applied to negative terminal.

Similarly a negative comparator is used for the negative envelope with the reference applied to positive terminal. For the initial step of fault detection, this set of comparators in ‘signal processing 1’ block is set to a reference threshold of $\pm 0.08\text{V}$. The duration for which the positive envelope is higher than 0.08V and the negative envelope is lower than -0.08V , is monitored. The corresponding comparators then give a digital logic 1 level output for these durations, Fig. 6.13 (bottom).

6.4.4 Digital output bit representation

Bit 1 output

Transients in power-line signals are potentially the most detrimental type of power disturbance [111]. These transients normally fall into two sub-categories,

1. Impulsive
2. Oscillatory

Impulsive transients are sudden high peak glitches that increase the voltage and/or current levels in either the positive or the negative direction. These transients last for a short while but may cause huge damage to the power system. But these impulsive glitches are most times taken care of in existing power systems because of advances in the MOV technology. MOVs allow for a consistent and reliable suppression of impulsive transients, swells, and other high voltage conditions. They are combined with tripping devices such as circuit breakers to interrupt the power flow if these conditions are beyond repair and prevail long enough to cause damage.

An **oscillatory** transient is a sudden change in the steady-state condition of a signal’s voltage and/or current, in both positive and negative directions, oscillating at the natural system frequency. This transient causes the power signal to alternate very rapidly in both directions high and low. Oscillatory transients that decay to zero within a cycle can usually be taken care of by use of chokes that dampen these oscillations to a tolerable, non-destructive level. But

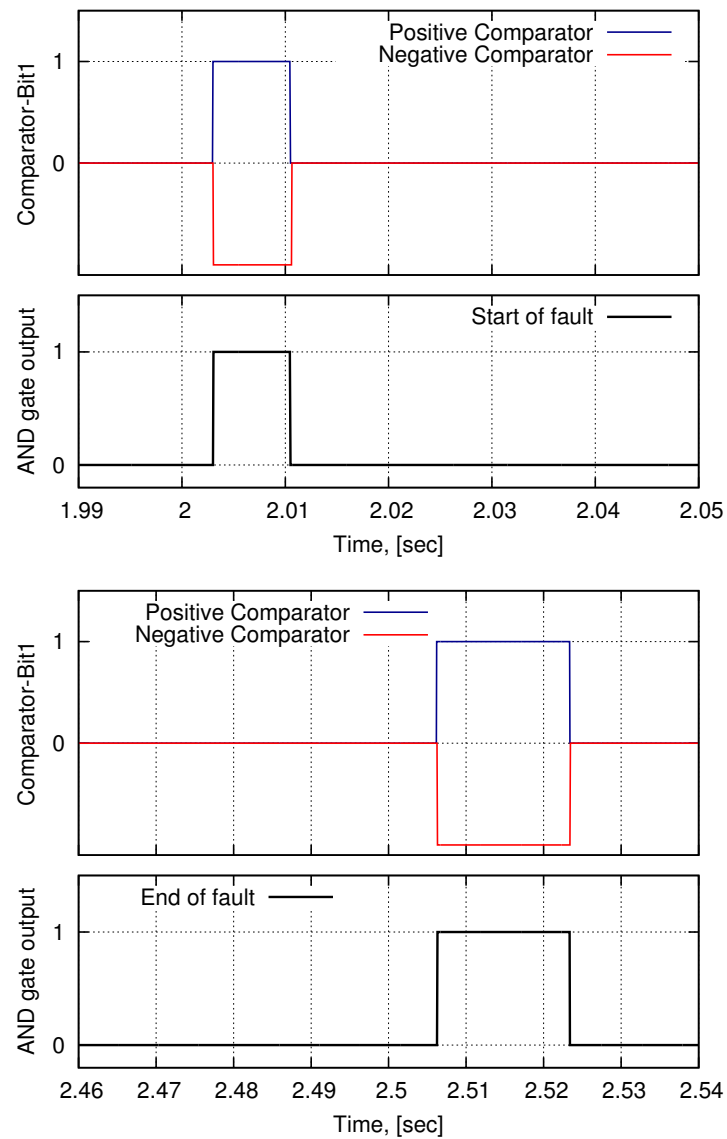


Figure 6.14: Time-domain plots of positive and negative comparator waveforms and corresponding AND gate decision signal during start of fault (top) and end of fault (bottom).

these oscillatory transients could be a start of a bigger persistent problem as in our considered case.

To rule out any mis-triggering of our decision making circuit on account of a brief non-harmful transient, it is necessary to monitor presence of high frequency disturbance for at least one whole cycle of operation of signal. Hence if a digital high output is obtained at positive comparator immediately followed by a high output at negative comparator, it proves that the glitch is oscillatory and continual enough to cause a fault. To ensure this, and to classify the glitch as a faulty signal, both comparator outputs are then applied to an AND gate. This makes sure that the AND gate output is high only when both comparator inputs are high, Fig. 6.14. This output then sets `bit 1` high or low depending on presence or absence of a fault.

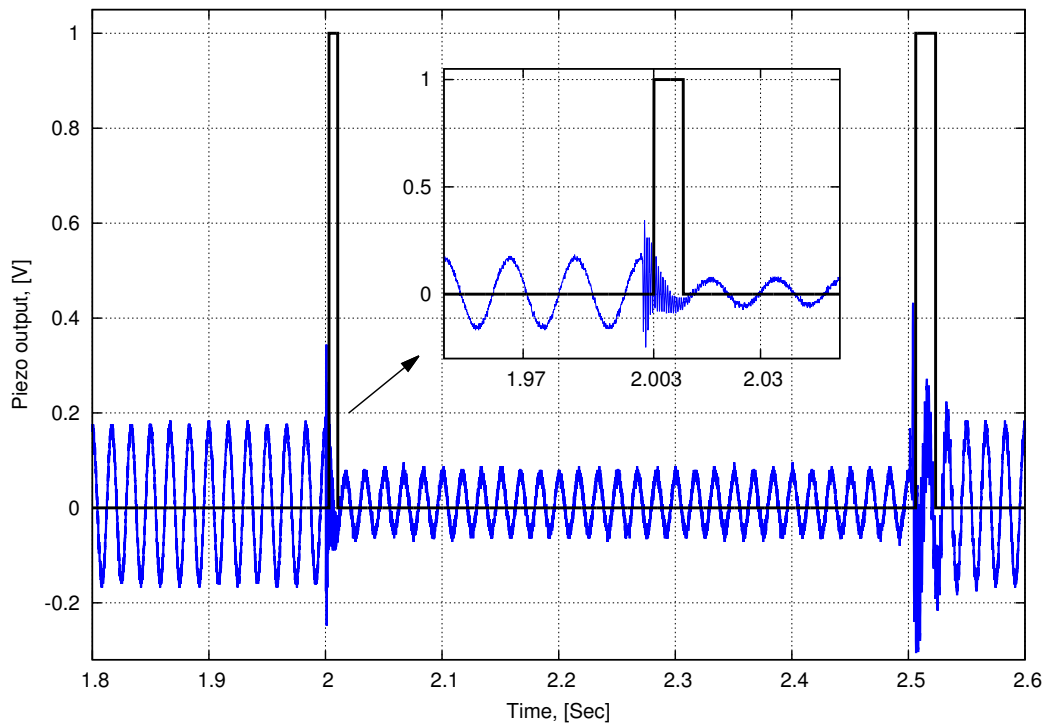


Figure 6.15: Experimentally recorded time-domain piezo output overlapped with comparator outputs for case 2, fault AB-g condition.

In this case, as comparator outputs are higher for more than one cycle of the oscillation, `bit 1` is set to 1. The occurrence of system fault at 2s causes a sag in the phase voltage resulting in an undervoltage condition. This sag is usually accompanied by an increase in the current, also

referred to as an overcurrent condition which was discussed briefly in Chapter 5. The fault lasts for 0.5s and results in another glitch and hence results in a high AND gate output at 2.5s. The undervoltage status of phase A voltage between these two AND gate signals is an indication of the start and end of fault. This duration could be shorter or longer depending on the severity of fault. The integrated circuits that will be used in signal processing system are high speed ICs and their internal propagation delay is negligible. Considering this delay in combination with group delay through PT, the system detects occurrence of fault in approximately 3ms, Fig. 6.15.

Bit 2 output

Once bit 1 categorizes the condition as a ‘fault’ condition, second bit of information is used to distinguish between case 1 and case 2 faults. For bit 2 logic, HP filtered piezo output is further passed through a 400Hz band-pass (BP) filter. To ensure a maximally flat response in the range that includes 400Hz tone, in order to isolate energy of the 400Hz tone with high efficiency, a Butterworth BP filter is used for this purpose. To obtain a steep response curve to ensure narrow roll-off outside of the desired band of frequencies, but at the same time not increasing the filter design complexity, we have chosen a 4th order Butterworth filter with a centre frequency of 400Hz and a bandwidth of 35Hz around it.

This BP filtered signal is then fed to the ‘signal processing 2’ unit. The peak detector output obtained at this stage is close to zero throughout the 5s duration. This output fed to the comparator circuit, causes its output too to be set to zero, which suggests that input to comparator is below its threshold and that the signal does not contain a 400Hz tone. Since the BP filter attenuates all other frequencies too, the signal fed to the comparator circuit has negligible energy at all frequencies. As a result, bit 2 is set to 0 and fault is categorized as case 2 fault. If bit 2 was set to 1, it would have indicated that the fault belongs to case 1 condition. Then in that case, third bit of data would be useful to categorize the fault either as AB fault or any other fault within case 1. But in this particular case, third bit data becomes

redundant.

Bits 4 and 5 output

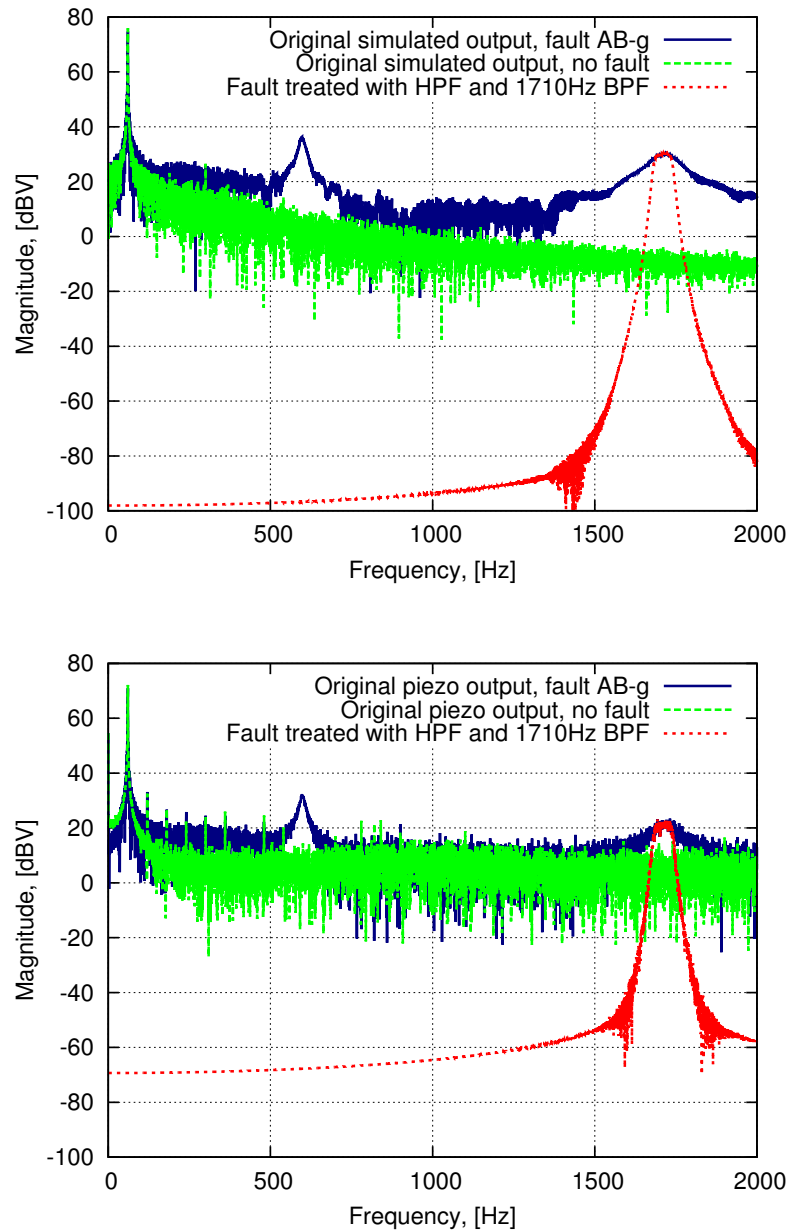


Figure 6.16: Frequency spectrum of original PT output for fault AB-g, case 2 and PT output for no-fault condition, overlapped with output after being treated with HP and 1710Hz BP filter, simulated (top) and experimentally recorded (bottom).

The logic devised for the cases considered here, consists of four rungs of processing. The

HP filtered PT output is fed to all these four levels simultaneously to assure fast detection of faults. As the third bit is redundant for this particular case, we will analyse the 4th level of processing in the following narrative.

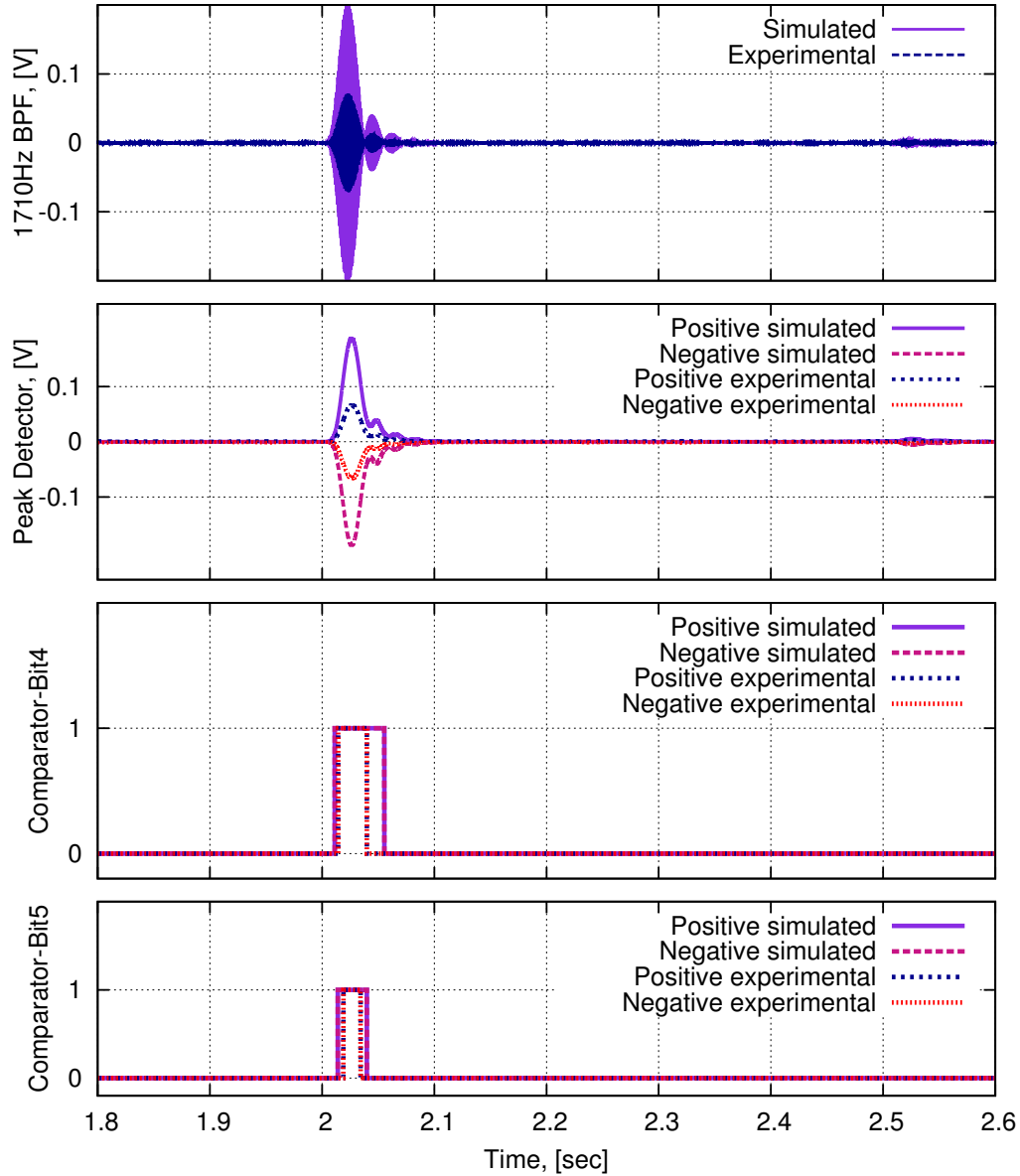


Figure 6.17: Output time-domain signals from the 1710Hz BP filter (top), peak detector output (second), comparator output for bit 4 (third), comparator output for bit 5 (bottom).

Similar to 400Hz band-pass (BP) filter, this level of detection logic consists of a 1710Hz BP filter and ‘signal processing 4’ unit. As seen from Figure 6.3, the frequency spread of voltage signals around 1710Hz is wider as compared to that around 400Hz in Figure 6.2. Hence a

lower order filter with comparatively smaller slope is used in this logic as compared to bit 2 logic. For a flat response in the desired band of frequencies, we use a 3rd order Butterworth filter with centre frequency of 1710Hz and a bandwidth of 60Hz. Figure 6.16 shows the effect of HP and BP filters on piezo output for the considered fault AB-g, for the PT model (top) and for actual experimental outputs (bottom).

The ‘signal processing 4’ block consists of three sets of comparators to provide information for bit 4 to bit 6. At node R in Figure 6.7, all other frequencies except 1710Hz are suppressed which makes the fault detectable for the next stages, Fig. 6.17 (top). This frequency component is characteristic of onset of a fault and hence can only be seen around 2s in time domain. The peak detector circuit traces the envelope of the filtered output to be applied as input to comparator stage, Fig. 6.17 (second).

First set of comparators is used to distinguish between faults within case 2 based on whether the signal contains a 1710Hz tone. This comparator is set to a low threshold of $\pm 0.01V$ to eliminate fault conditions that correspond to signals with no or lower strength of 1710Hz frequency tone. As shown in Figure 6.17 (third), for the considered fault case, peak detector output exceeds this threshold and bit 4 is set high. This fault is therefore categorized fault into ‘Case2:ABC-g,AB,AC,AC-g,AB-g’ condition as per the truth table.

There are three distinct dB levels that correspond to three separate sets of faults within the ‘Case2:ABC-g,AB,AC,AC-g,AB-g’ category, Fig. 6.5. In time domain this corresponds to three levels of magnitude of the envelope signal. Second set of comparators in ‘signal processing 4’ block is used to singularise the signal with highest magnitude out of these three levels. This comparator has a higher threshold set to $\pm 0.04V$. Due to the magnitude of positive input of over 0.06V and negative input of less than $-0.06V$, Fig. 6.17 (second), both positive and negative comparators give high outputs. Similar to as described in the previous section, these output signals are then applied to an AND gate and bit 5 is also set to 1, Fig. 6.17 (bottom).

For the third set of comparators, a window comparator is used. A window comparator

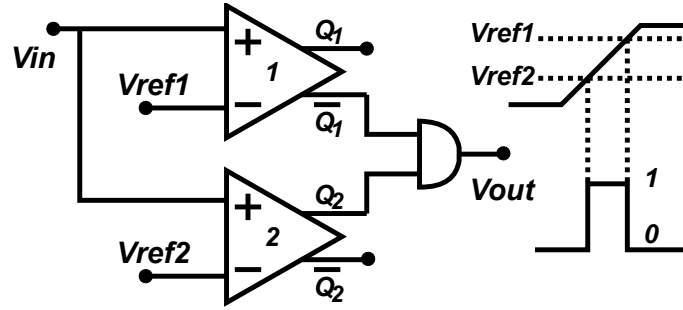


Figure 6.18: Simplified schematic diagram of two-level window comparator.

consists of two comparators in basic non-inverting configuration, with different reference voltages, typically a higher threshold and a lower threshold of a desirable range, and a common input voltage. For the time that V_{in} is less than V_{ref1} in comparator 1, Q_1 remains low, hence $\overline{Q_1}$ becomes high, Fig. 6.18. Similarly, when V_{in} is less than V_{ref2} in comparator 2, Q_2 is low. The moment V_{in} becomes greater than V_{ref2} , Q_2 becomes high. Hence by applying these two output signals, ($\overline{Q_1}$ and Q_2), to an AND gate, it is ensured that the final output logic level is asserted, that is V_{out} is high, only when the input signal falls between the two reference voltages, Fig. 6.18 [112].

A positive and negative window comparator is therefore used in ‘signal processing 4’ block in the 3rd set of comparators, with one reference voltage greater than the threshold of first comparator, $\pm 0.025V$, and the other reference voltage equal to the threshold of second comparator, $\pm 0.04V$.

The negative window comparator consists of comparators in their inverting configuration for the negative peak detector output. This is to detect signals that have magnitudes between $+0.025V$ and $+0.04V$ and between $-0.025V$ and $-0.04V$ corresponding to ‘Case2:AC,AC-g’ category for a high logic level bit 6 output. For a low logic level bit 6, with bit 1 and bit 4 set, it indicates a ‘Case2:ABC-g’ category fault.

However, in the case considered, with the 5th bit set, a conclusive bit combination of X11X01 is obtained which matches an entry in truth table and it can be inferred that fault considered belongs to ‘Case2:AB,AB-g’ category. It must be noted that bit 5 is set high af-

ter approximately 10ms delay of bit 1 setting high. This indicates that although the presence of fault is detected within 3ms, the categorization of fault happens only after a certain delay.

Hence each combination of these six bits as seen in truth table yields a result which denotes the presence, location and type of fault. In this example we have considered phase A voltage signals. A similar system is designed for phases B and C, and an universal decision making logic is then established to identify all fault types.

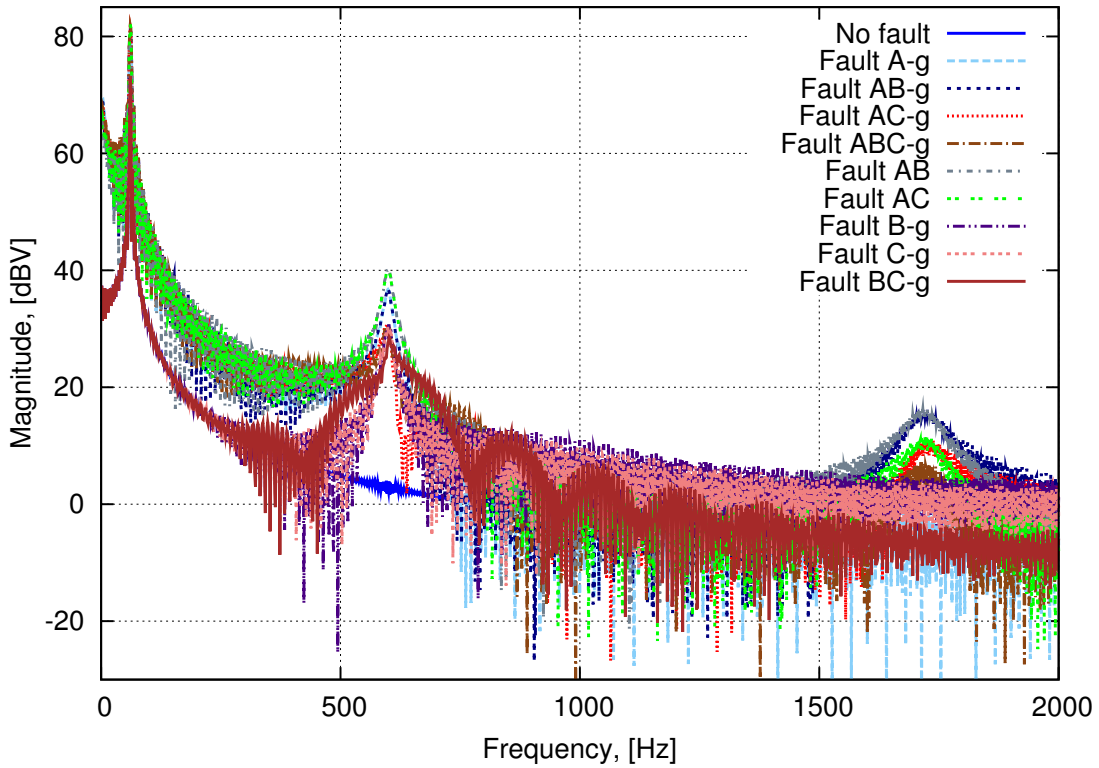


Figure 6.19: Frequency spectrum of simulated secondary current signals from *PSCAD*.

We also considered the frequency structure of secondary current signal in power systems that would serve as an input to our current sensor. Similar to voltage signals, current signals also have a deterministic frequency spectrum profile that corresponds to the fault type, Fig. 6.19. The current frequency spectrum is equivalent to the corresponding voltage frequency spectrum and gives the same fault information. As the proposed sensing IC has linear, ratio-metric characteristics, we expect the corresponding output voltages to have a similar frequency composition as the input current. Thus, in order to include cases when all measured phase

voltages are zero, similar signal processing system is used for analysis along with the MLX sensor circuit employed to sense the real-time current signals corresponding to these cases.

6.4.5 Actual circuit implementation

The model discussed in this chapter is based on the fact that the actual realization of the signal processing circuit will be with integrated circuits. In this section, we present some of the alternatives suitable for each function in processing steps with suggested electronics.

Buffer circuit

As discussed in Chapter 4, to avoid the loading effect due to oscilloscope, we used passive probes to record PT's output. In actual circuit implementation too, to avoid any amount of loading and distortion caused by the IC circuits to the original PT output, we will use a buffer circuit at the output electrode of PT. Use of a buffer circuit at PT output acts as an impedance matching network between the PT circuit and any kind of load and processing circuit that follows.

We suggest a high-speed, unity gain buffer IC to prevent interference with desired PT operation when connected to the output circuit. TLC1079 is one such ultra-low power dissipation device suitable for this purpose. TLC107x family incorporates internal ESD protection that prevents functional failures at voltages as high as 2000V and is made for high-density system applications [113]. It will be used in the buffer configuration with inverting input connected to the output.

Filters and Peak detector circuit

Commercial HP filters and BP filters are available for the desired ranges in processing. Preferred ICs are universal circuits in which both band pass and high pass functions can be incorporated to reduce space occupancy. An active diode IC will be used in the peak detector circuit with R and C values chosen for accurate envelope detection.

Comparator circuit

Every signal processing block in our system has at least two sets of comparators, one for positive envelope signal and one for negative envelope signal. Hence one suggestion is to use a commercial ‘quad comparator’ IC. TLV3404 is one such nanopower open drain output comparator. This IC is made for extended industrial temperature ranges and hence is suitable for our application. Both inverting and non-inverting configurations can be used in this quad IC [114]. AND gate ICs are used in combination with the comparator IC. Several comparator outputs can be applied to a combined AND gate depending on the number of channels available.

6.5 Summary

In modern diagnostic and protection systems, signal processing is a very crucial step, in order to make the sensed signals compatible with decision making logic used in the processor. In this chapter, we discuss the attributes of signal processing involved in a typical digital relay system and the function of each block.

In order to design a suitable signal processing function, the first step is to understand the nature of inputs fed to it. In relay systems, these inputs are usually analogue voltage and current signals and their magnitudes depend on the operating conditions. We also state the major causes of any kind of disruption in normal operating conditions that results in a fault in the relay system. Various detection and differentiation criteria are used in existing systems based on the type of faults. We present one such method based on unique frequency signatures of real-time signals depending on the conditions.

For the cases considered, depending on the frequency compositions of the phase voltages, we arrive at a logical truth table in this chapter. This truth table facilitates design of the signal processing and decision making behavioural model. The main functions involved in our design are high pass filtering, band pass filtering, peak detection or envelope creation, low pass filtering for smoothing, comparator circuits and finally a combinational AND gate for final digital

output. To demonstrate working of each block in our model, we have considered one particular fault case here and we compare actual experimental signal data with simulated outcomes.

The accuracy of this suggested system with respect to categorization of fault and response time can be seen through the output plots. Subject to required working ranges in actual scenarios and other considerations like power consumption, external supply limits and output levels, we suggest alternatives in form of integrated circuits for realising the described design for signal processing.

Chapter 7

Conclusions and Future Work

In this work, we propose a novel technique to create a sensing and disturbance monitoring methodology, which consists of a piezoelectric transformer in combination with a Hall-effect based sensor, for applications in power relay systems. We also present a signal processing model based on monitoring frequency spectrum signature of these sensed voltage and current signals for accurate and fast detection of faults in power systems.

7.1 Conclusions

As part of this research, the following tasks have been achieved in this thesis and are listed below:

- Basic understanding of a typical relay system and thorough background study of the existing low-power step-down and signal processing techniques being used.
- Establishment of mathematical relations that represent the electromechanical behaviour of a rectangular piezoelectric transformer in the Rosen-type configuration.
- Based on these established relations, we built a simple electrical model and tested the PT operation at resonance and in low frequency ranges. The results were compared with the existing results and behavioural deviations at low frequencies were recorded.

- The 3D PT model built in a numerical solver helped visualize the physical energy flow between input and output sections with set boundary conditions. Along with frequency and eigenfrequency studies, time-dependent study was performed to record PT transient responses.
- These simulated results were then compared with the actual experimental findings obtained, as PT was exposed to single-tone, multi-tone, variable frequency and real-time power signals.
- Various current sensing techniques used commercially were reviewed and a Hall-effect current sensor based on integrated magnetic concentrator concept was proposed and used for experimental measurements.
- The current sensor principle was analysed using a numerical solver and results were compared to the experimental records.
- The real-time secondary analogue relay outputs were found to consist frequencies with a distribution dependent on the type, location and intensity of fault. Based on this unique frequency structure, a fault detection and fault categorization method was established and demonstrated with an example. This technique is applicable for both voltage and current signals.

Based on the existing methodologies and our proposed techniques, the following design goals were met:

- As compared to the existing electromagnetic transformer, a voltage step-down device in form of PT offers a non-magnetic, high electrical isolation between the primary and secondary sides of a circuit.
- Issues like EMI, losses due to windings and size constraints were eliminated by using a compact PT. Due to absence of magnetic components in the device, magnetic shielding

is not necessary for PT circuits.

- PTs have high efficiency as compared to conventional transformers, especially in low power ranges and is easily integrable for miniaturisation of existing step-down circuit.
- The allowable signal delay through the sensing circuit in existing system is about 10ms. From the time of input application, the output digital signal in our system was obtained within 3ms.
- The frequency range of allowable voltage signal is wide in relay systems. It can contain up to 64 harmonics of power-line frequency. With a linear PT behaviour in this frequency range, characterisation of the harmonics is possible without any loss of signal.
- For existing current measurement system, the allowable current value is about 20% of normal range or 46 times the standard secondary current values (1A or 5A). The MLX sensor proposed in our work has a wide input current range which is limited only by the conductor size.
- The Hall based current sensor offers advantages like minimum losses, high accuracy and linear behaviour as compared to resistive sensing.
- IMC sensors are easily integrable and designed for use in integrated circuits.
- With an additional signal processing circuit along with the sensor and step-down devices, it was possible not only to detect a fault but to broadly classify it into the type and location of fault.

Experimental data for Rosen-type PT and MLX Hall-effect sensor are in agreement with numerical modelling analysis and indicate that the proposed methodology has sufficient advantages and potential to create a very low-power monitoring system. This work provides a platform to develop a complete integrated current and voltage measurement system which forms the basis of our future work.

7.2 Future Work

Some of the tasks that will be carried out as an extension to the work done are as follows:

- To make PT sustainable in high power environments and to avoid external mechanical disturbances to affect PT's performance, a mounting structure will be constructed. An optimum design will be chosen based on the model simulations by adding a 'Structural Mechanics' module to simulate mechanical deformations within *COMSOL*.
- Multilayering of PT laminations is equivalent to connection of PTs in parallel with each other [115]. Such a PT design will be explored and experimented with, to increase efficiency of PT.
- Phase shift in the signal at the output of the existing circuitry is about 1° . Hence a phase tracking and locking circuit will be incorporated to make sure the limits are not exceeded.
- It is also important for the phase shift between voltage and current signals to be consistent. This has to be particularly taken care of if two distinct, independent methods are used for voltage and current sensing. Hence a system incorporating both voltage and current sensing will be built with a phase detection circuit.
- In the full operating temperature range, the accuracy of the existing system is about 0.2%. Performance of our proposed system will be monitored on field over a period of time and additional sub-circuits for functions such as stress and temperature compensation will be designed for sustained highly accurate operation.

Bibliography

- [1] B. Lundqvist. 100 years of relay protection, the Swedish ABB relay history. Technical report, ABB Automation Products, Substation Automation Division, 2010.
- [2] J.S. Deliyannides and E.A. Udren. Design criteria for an integrated microprocessor-based substation protection and control system. *IEEE Transactions on Power Apparatus and Systems*, PAS-101(6):1664–1673, 1982.
- [3] M.S. Sachdev and R. Das. Understanding Microprocessor-based Technology Applied to Relaying. *IEEE Power System Relaying Committee*, 2004.
- [4] A.T. Johns and S.K. Salman. *Digital Protection for Power Systems*. Peter Peregrinus Ltd. on behalf of the Institution of Electrical Engineers, London, United Kingdom, 1995.
- [5] 2012 State of Reliability. Technical report, North American Electric Reliability Corporation, 2012.
- [6] A. G. Phadke and J. S. Thorp. *Computer Relaying for Power Systems*. Wiley, 2009.
- [7] M. Zadeh. Relay technologies and μ P-based relay hardware, 2011.
- [8] J. M. Kern, G. P. Koste, and et al. Current sensing system, US Patent 2005/0281560 A1.
- [9] Y. Tanaka, T. Shioda, and et al. Power line monitoring system using fiber optic power supply. *Optical Review*, 16:257–261, 2009.

- [10] D. G. Fletcher and G. P. Lavoie. Power line monitoring and interrupt method and apparatus, US Patent 2005/6,968,277 B2.
- [11] S. Ziegler, R.C. Woodward, and H. Iu. Current sensing techniques: A review. *Sensors Journal*, 9(4):354–376, 2009.
- [12] R. Dickinson and S. Milano. *Isolated Open Loop Current Sensing Using Hall Effect Technology in an Optimized Magnetic Circuit*. Allegro MicroSystems, Inc., 2002.
- [13] J.D.P. Hrabliuk. Interfacing optical current sensors in a substation. *2001 Power Engineering Society Summer Meeting. Conference Proceedings (Cat. No.01CH37262)*, pages 147–155, 2001.
- [14] Z. Gang, L. Shaohui, Z. Zhipeng, and C. Wei. A novel electro-optic hybrid current measurement instrument for high-voltage power lines. *IEEE Transactions on Instrumentation and Measurement*, 50(1):59–62, 2001.
- [15] L. Chihyi. *Design and Analysis of Piezoelectric Transformer Converters*. PhD thesis, Virginia Polytechnic Institute and State University, July 1997.
- [16] Y.H. Hsu, C.K. Lee, and W.H. Hsiao. Optimizing piezoelectric transformer for maximum power transfer. *Smart materials and structures*, 373, 2003.
- [17] A.M. Flynn and S.R. Sanders. Fundamental limits on energy transfer and circuit considerations for piezoelectric transformers. *IEEE Transactions on Power Electronics*, 17(1):8–14, 2002.
- [18] T. Zaitso, T. Inoue, and et al. 2 mhz power converter with piezoelectric ceramic transformer. *[Proceedings] Fourteenth International Telecommunications Energy Conference – INTELEC '92*, pages 430–437, 1992.

- [19] V. Dejan, F. Costa, and E. Sarraute. A new mosfet and igbt gate drive insulated by a piezoelectric transformer. *32nd Annual Power Electronics Specialists Conference (IEEE Cat. No.01CH37230)*, pages 1479–1484, 2001.
- [20] P. Alou, J. Cobos, M. Sanz, R. Prieto, and J. Uceda. Subharmonic driving: a new concept to drive piezoelectric transformers in power converters. *APEC 2001. Sixteenth Annual IEEE Applied Power Electronics Conference and Exposition (Cat. No.01CH37181)*, pages 487–491, 2001.
- [21] Smart material. http://en.wikipedia.org/wiki/Smart_material.
- [22] H. W. Katz, editor. *Solid State Magnetic and Dielectric Devices*. John Wiley and Sons, Inc., 1959.
- [23] T. Ikeda. *Fundamentals of Piezoelectricity*. Oxford University Press, 1990.
- [24] D. Damjanovic. *Hysteresis in piezoelectric and ferroelectric materials*, volume 3. Elsevier, 2005.
- [25] S. Martin. *Piezoelectric transformer based power converters; design and control*. PhD thesis, Technical University of Denmark, September 2012.
- [26] W. Mason. *Physical Acoustics*, volume 1. Academic press, 1964.
- [27] E. M. Syed. Analysis and modeling of piezoelectric transformers. Master’s thesis, University of Toronto, 2001.
- [28] R. Holland, editor. *Design of Resonant Piezoelectric Devices*. The M.I.T. Press, 1969.
- [29] E. Wells. Comparing magnetic and piezoelectric transformer approaches in CCFL applications. Technical report, Texas Instruments Incorporated, 2002.
- [30] C. A. Rosen, K. A. Fish, and H. C. Rothenberg. Electromechanical transformer, US Patent 1958/2,830,274.

- [31] V. Dejan, F. Costa, and E. Sarraute. Piezoelectric transformer for integrated mosfet and igbt gate driver. *IEEE Transactions on Power Electronics*, 21(1):56–65, 2006.
- [32] Y.H. Hsu, C.K. Lee, and W.H. Hsiao. Electrical and mechanical fully coupled theory and experimental verification of Rosen-type piezoelectric transformers. *IEEE transactions on ultrasonics, ferroelectrics, and frequency control*, 52(10):1829–39, October 2005.
- [33] E.L. Horsley, M.P. Foster, and D.A. Stone. State-of-the-art piezoelectric transformer technology. In *2007 European Conference on Power Electronics and Applications*, pages 1–10, sept. 2007.
- [34] K. Uchino, P. Laoratanakul, S. Manuspiya, and A. Vázquez-Carazo. High power piezoelectric transformers, 2006.
- [35] NASA. Novel high-voltage, high-power piezoelectric transformer developed and demonstrated for space communications applications. www.grc.nasa.gov/WWW/RT/2003/5000/5620wintucky.html, 2003.
- [36] D. Vasic, E. Sarraute, F. Costa, and et al. Piezoelectric micro-transformer based on PZT unimorph membrane. *Journal of Micromechanics and Microengineering*, 90, 2004.
- [37] B. S. Lee, W. J. Wu, W. P. Shih, D. Vasic, and F. Costa. P2E-3 Power Harvesting Using Piezoelectric MEMS Generator with Interdigital Electrodes. *2007 IEEE Ultrasonics Symposium Proceedings*, pages 1598–1601, October 2007.
- [38] M. Sanz, P. Alou, R. Prieto, J.A. Cobos, and J. Uceda. Comparison of different alternatives to drive piezoelectric transformers. *APEC. Seventeenth Annual IEEE Applied Power Electronics Conference and Exposition (Cat. No.02CH37335)*, pages 358–364, 2002.
- [39] W. Mason. *Electromechanical Transducers and Wave Filters*. D. Van Nostrand Company, Inc., 2 edition, 1948.

- [40] F. Boukazouha and F. Boubenider. Piezoelectric transformer: Comparison between a model and an analytical verification. *Computers & Structures*, 86(3-5):374–378, February 2008.
- [41] G. Ivensky, I. Zafrany, and S. Ben-Yaakov. Generic operational characteristics of piezoelectric transformers. *IEEE Transactions on Power Electronics*, 17(6):1049–1057, 2002.
- [42] V. L. Karlash. Resonant Electromechanical Vibrations of Piezoelectric Plates. *International Applied Mechanics*, 41(7):709–747, July 2005.
- [43] J.A. Oliver, R. Prieto, M. Sanz, J.A. Cobos, and J. Uceda. Id modeling of multi-layer piezoelectric transformers. *IEEE 32nd Annual Power Electronics Specialists Conference, 2001. PESC. 2001*, pages 2097–2102, 2001.
- [44] APC International Ltd. <http://www.americanpiezo.com/knowledge-center/piezo-theory/piezoelectric-constants.html>.
- [45] M. Trindade and A. Benjeddou. Effective Electromechanical Coupling Coefficients of Piezoelectric Adaptive Structures: Critical Evaluation and Optimization. *Mechanics of Advanced Materials and Structures*, 16(3):210–223, April 2009.
- [46] The Institute of Electrical and Electronics Engineers. IEEE Standard on Piezoelectricity, 1988.
- [47] T. Zaitzu, O. Ohnishi, and et al. Piezoelectric transformer operating in thickness extensional vibration and its application to switching converter. *25th Annual IEEE Power Electronics Specialists Conference, PESC '94*, pages 585–589, June 1992.
- [48] A. Benwell, S. Kovaleski, and M. Kemp. A resonantly driven piezoelectric transformer for high voltage generation. *2008 IEEE International Power Modulators and High-Voltage Conference*, pages 113–116, 2008.

- [49] E. Favre and W. Teppan. Current sensing in electric drives – a future and history on multiple innovations. *6th International Symposium on Advanced Electro-mechanical Motion System*, 2005.
- [50] C. Xiao, L. Zhao, T. Asada, W.G. Odendaal, and J.D. van Wyk. An overview of integratable current sensor technologies. *38th IAS Annual Meeting on Conference Record of the Industry Applications Conference*, 2003., 2:1251–1258, 2003.
- [51] H.P. Forghani-zadeh and G.A. Rincon-Mora. Current-sensing techniques for dc-dc converters. In *The 2002 45th Midwest Symposium on Circuits and Systems, 2002 (MWSCAS-2002)*, volume 2, pages II–577–II–580 vol.2, 2002.
- [52] 1–Axis Magnetic Sensor HMC1041Z. <http://www.honeywell.com/magneticsensors>, April 2005.
- [53] 2–Axis Magnetic Sensor HMC1042L. <http://www.honeywell.com/magneticsensors>, November 2006.
- [54] Nanjing AH Electronic Sci & Tech Co. Ltd. Manufacturer’s Specification of WG Series Wiegand Sensors and Wiegand Modules. Technical report, Nanjing AH Electronic Sci & Tech Co., Ltd., P.R.China, 2003.
- [55] Y. N. Ning, Z. P. Wang, A. W. Palmer, K. T. V. Grattan, and D. A. Jackson. Recent progress in optical current sensing techniques. *Review of Scientific Instruments*, 66(5):3097, 1995.
- [56] B. Djokic and E. So. An Optically Isolated Hybrid Two-Stage Current Transformer for Measurements at High Voltage. *IEEE Transactions on Instrumentation and Measurement*, 55(4):1204–1207, August 2006.

- [57] S. Zadvornov and A. Sokolovsky. Electro-Optic Hybrid Multifunctional. In *I2MTC 2008 - IEEE International Instrumentation and Measurement Technology Conference, Victoria, Vancouver Island, Canada, May 12-15, 2008*, pages 16–17, 2008.
- [58] N. McNeill. Active current transformer circuits for low distortion sensing in switched mode power converters. *IEEE Transactions on Power Electronics*, 19(4):908–917, 2004.
- [59] R.S. Popovic. *Hall Effect Devices*. Institute of Physics Publishing, second edition, 2004.
- [60] Honeywell and MICRO SWITCH Sensing and Control. *Hall Effect Sensing and Application*. Honeywell Inc., Illinois, 2011.
- [61] E. Ramsden. *Hall-Effect Sensors*. Newnes, Elsevier, 2006.
- [62] M.J. Caruso and T. Bratland. A new perspective on magnetic field sensing. Technical report, Honeywell Inc., 1998.
- [63] R.S. Popovic, Z. Randjelovic, and D. Manic. Integrated Hall-effect magnetic sensors. *Sensors and Actuators A: Physical*, 91(1-2):46–50, June 2001.
- [64] J. Meer, F.R. Riedijk, E. Kampen, K.A.A. Makinwa, and J.H. Huijsing. A fully integrated CMOS Hall sensor with Hall Sensor Chopped. *2005 IEEE International Solid-State Circuits Conference*, pages 246–247, 2005.
- [65] R. Popovic, R. Racz, J. Hrejsa, and H. Blanchard. Magnetic Field Sensor and Current and/or Energy Sensor, US Patent 1999/5,942,895.
- [66] R. Racz. A Novel Contactless Current Sensor for HEV / EV and Renewable Energy Applications. Technical report, Melexis, 2010.
- [67] R. Lerch. Simulation of piezoelectric devices by two- and three-dimensional finite elements. *IEEE transactions on ultrasonics, ferroelectrics, and frequency control*, 37(3):233–247, May 1990.

- [68] S. Hallaert, E. Sarraute, and B. Le Pioufle. Numerical and analytical modeling of the piezoelectric transformer and experimental verification. *Technical Proceedings of the 1999 International Conference on Modeling and Simulation of Microsystems, MSM 1999*, pages 198–201, 1999.
- [69] T. Tsuchiya, Y. Kagawa, and et al. Finite element simulation of piezoelectric transformers. *IEEE transactions on ultrasonics, ferroelectrics, and frequency control*, 48(4):873–878, July 2001.
- [70] S. Ho. Modeling and analysis on ring-type piezoelectric transformers. *IEEE transactions on ultrasonics, ferroelectrics, and frequency control*, 54(11):2376–2384, November 2007.
- [71] Y. Yang, C. Chen, Y. Chen, and C. Lee. Modeling of piezoelectric transformers using finite-element technique. *Journal of the Chinese Institute of Engineers*, 31(6):925–932, 2008.
- [72] H. Xue, J. Yang, and Y. Hu. Analysis of rosen piezoelectric transformers with a varying cross-section. *Ultrasonics*, 55(7):1632–1639, 2008.
- [73] K. Chang and C. Lee. Fabrication and characteristics of thin disc piezoelectric transformers based on piezoelectric buzzers with gap circles. *Ultrasonics*, 48(2):91–97, 2008.
- [74] F. Pigache. Modeling and Identification of Rosen-Type Transformer in Nonlinear Behavior. *IEEE transactions on ultrasonics, ferroelectrics,*, 58(12):2562–2570, December 2011.
- [75] COMSOL. COMSOL Multiphysics – User’s Guide. www.comsol.com.
- [76] C. Nadal and F. Pigache. Multimodal electromechanical model of piezoelectric transformers by Hamilton’s principle. *IEEE Transactions on Ultrasonics, Ferroelectrics and Frequency Control*, 56(11):2530–2543, 2009.

- [77] S. Tuncdemir and W. Bradley. Experimental Verification of the Power Transfer and Thermal Characteristics of Piezoelectric Transformers Subjected to Combined Mechanical and Electrical Loading. In *2012 COMSOL Conference*, 2012.
- [78] T. Anderson, M. Anderson, and O. Thomsen. Simulation of Piezoelectric Transformers with COMSOL. In *2012 COMSOL Conference*, 2012.
- [79] Piezoelectric Ceramics. <http://www.fujicera.co.jp/product/e/index.html>.
- [80] Y. Shindo. Electroelastic Fracture Mechanics of Piezoelectric Layered Composites. *Journal of Intelligent Material Systems and Structures*, 16(7-8):573–582, July 2005.
- [81] IDC Technologies. Faults Types & Effects. Technical report, IDC Technologies Tech Briefs (Electrical), 2000.
- [82] S.G. Aquiles Perez, M.S. Sachdev, and T.S. Sidhu. Modeling relays for use in power system protection studies. *Canadian Conference on Electrical and Computer Engineering, 2005*, pages 566–569, May 2005.
- [83] Group delay and phase delay. http://en.wikipedia.org/wiki/Group_delay_and_phase_delay.
- [84] Fuji Ceramics Corporation. *Piezoelectric Ceramic for Transformer*.
- [85] A.V. Mezheritsky. Quality factor concept in piezoceramic transformer performance description. *IEEE transactions on ultrasonics, ferroelectrics, and frequency control*, 53(2):429–42, February 2006.
- [86] S. Lineykin and S. Ben-Yaakov. Feedback isolation by piezoelectric transformers: Comparison of amplitude to frequency modulation. *IEEE Power Electronics Specialists*, 2:830–847, 2004.

- [87] S. Lele, R. Sobot, and T. Sidhu. Frequency measurement and disturbance monitoring using piezoelectric transformers. *IEEE Power and Energy Conference at Illinois, 2012 (PECI 2012)*, 2012.
- [88] Y. Shimada and N. Honbo. Actuating circuit of piezoelectric transformer and actuating method thereof, US Patent 1999/5,866,969.
- [89] Manitoba HVDC Research Centre Inc. *Applications of PSCAD/EMTDC*.
- [90] Manitoba HVDC Research Centre Inc. *Power System Waveform Generator, Real Time Playback*. Manitoba HVDC Research Centre Inc., 2002.
- [91] K. Ishii, N. Akimoto, S. Tashirio, and H. Igarashi. Influence of Load Resistance on Higher Harmonic Voltages Generated in a Piezoelectric Transformer. *Japanese Journal of Applied Physics*, 37:5330, September 1998.
- [92] K. Chang and K. Li. Open-circuit test of a piezoelectric transformer and its applications. *30th Annual Conference of IEEE Industrial Electronics Society, 2004. IECON 2004*, pages 2424–2429, 2004.
- [93] G. Swift. The spectra of fault-induced transients. *IEEE transactions on Power Apparatus and Systems*, 98(3):940–947, June 1979.
- [94] J. Du, J. Hu, and K. Tseng. Vibration distribution in output sections of a piezoelectric transformer operating at thickness shear mode. *IEEE transactions on ultrasonics, ferroelectrics, and frequency control*, 54(10):1984–91, October 2007.
- [95] Y. Sato. Piezoelectric transformer with an improved armor case, US Patent 2000/6,054,798.
- [96] G. Vaughn. Piezoelectric device having increased mechanical compliance, US Patent 2002/6,448,697.

- [97] B.W. Hyun, W.H. Lee, and G.L. Na. Piezoelectric transformer device and housing for piezoelectric transformer and method of manufacturing them, US Patent 2004/6,833,653.
- [98] J.M. Cruz-Hernandez and V. Hayward. An approach to reduction of hysteresis in smart materials. *Proceedings. 1998 IEEE International Conference on Robotics and Automation (Cat. No.98CH36146)*, 2(May):1510–1515, 1998.
- [99] I. Kartashev, T. Vontz, and H. Florian. Regimes of piezoelectric transformer operation. *Measurement Science and Technology*, 17(8):2150–2158, August 2006.
- [100] C. Yeack-Scranton. Novel piezoelectric transducers to monitor head-disk interactions. *IEEE Transactions on Magnetics*, 22(5):1011–1016, 1986.
- [101] Melexis. Application Note on Non intrusive current sensing with MLX91205. Technical report, Melexis, 2008.
- [102] Development Kit MLX91205–CSA-1V. <http://www.melexis.com>, March 2009.
- [103] MLX91205 IMC Current Sensor. <http://www.melexis.com>, June 2009.
- [104] C. Schott, R. Racz, and S. Huber. Smart cmos sensors with integrated magnetic concentrators. In *Sensors, 2005 IEEE*, 2005.
- [105] P. Emerald. Non Intrusive Hall Effect Current Sensing Techniques Provide Safe, Reliable Detection and Protection for Power Electronics, 1998.
- [106] H.A. Peterson. *Transients in Power Systems*. John Wiley & Sons, Inc., 1951.
- [107] A. Greenwood. *Electrical Transients in Power Systems*. John Wiley & Sons, Inc., second edition, 1991.
- [108] K. Zimmerman and D. Costello. Fundamentals and improvements for directional relays. *2010 63rd Annual Conference for Protective Relay Engineers*, pages 1–12, 2010.

- [109] J.O. Brien, A. Deronja, C. Liu, and J. Mooney. Use of Synchrophasor Measurements in Protective Relaying Applications. Technical report, Power System Relaying Committee, 2012.
- [110] D. Ducu. Op Amp Rectifiers, Peak Detectors and Clamps. Technical report, Microchip Technology Inc., 2011.
- [111] J. Seymour and T. Horsley. The seven types of power problems. Technical report, Schneider Electric, 2005.
- [112] Analog Devices. Comparators. Technical report, Analog Devices Inc., 2011.
- [113] Texas Instruments. *TLC1078, TLC1078Y, TLC1079, TLC1079Y LinCMOSTM μ Power Precision Operational Amplifiers*, 2001.
- [114] Texas Instruments. *TLV3401, TLV3402, TLV3404 Family of Nanopower Open Drain Output Comparators*, 2000.
- [115] T. Hemsel and S. Priya. Model based analysis of piezoelectric transformers. *Proceedings of Ultrasonics International and World Congress on Ultrasonics (WCU)*, 44(1):e741–e745, 2006.
- [116] GE-Multilin. *Reference guide - Protection, Control, Metering, Communications, Instrument Transformers*. GE Multilin, 2008.
- [117] GE-Multilin. *350C Feeder Protection System*. GE Multilin, 2009.
- [118] K. Chang and K. Li. Open-circuit test of a piezoelectric transformer and its applications. *30th Annual Conference of IEEE Industrial Electronics Society, 2004 (IECON 2004)*, pages 2424–2429, 2004.
- [119] F. Wang, J. Wu, Y. Jia, H. Zhu, X. Zhao, and H. Luo. Rosen-type $\text{Pb}(\text{Mg}_{1/3}\text{Nb}_{2/3})\text{O}_3\text{-PbTiO}_3$ single crystal piezoelectric transformer. *The Review of scientific instruments*, 78(7):073903, July 2007.

- [120] A.M. Sanchez, M. Sanz, R. Prieto, J.A. Oliver, and J.A. Cobos. Mixed analytical and numerical design method for piezoelectric transformers. In *Power Electronics Specialist Conference, 2003. PESC '03. 2003 IEEE 34th Annual*, volume 2, pages 841–846 vol.2, June 2003.

Appendix A : *COMSOL* piezoelectric general equations

1. Eigenfrequency & Frequency Domain Studies:

$$-\rho\omega^2 u - \nabla \cdot T = F_v \quad (1)$$

$$-i\omega = \lambda \quad (2)$$

$$\nabla \cdot (D + J_i(i\omega)^{-1}) = \rho_v \quad (3)$$

2. Time Dependent Study Representation:

$$\rho \frac{\partial^2 u}{\partial t^2} - \nabla \cdot T = F_v \quad (4)$$

$$\nabla \cdot D = \rho_v \quad (5)$$

where, F_v = preload force

3. Susceptance B evaluated using expression, $B = \text{imag}(pzd.Y11)$

4. Dependent variables:

(a) Displacement field components (u, v, w)

(b) Electrical potential (V)

Appendix B : *MATLAB* functions in signal processing model

1. High pass filter with cut-off frequency 200Hz

```
[b,a] = butter(5, 0.02, 'high');  
output1 = filter(b,a,input);
```

2. Bandpass filter with centre frequency 1710Hz and bandwidth of 60Hz around it

```
[d,c] = butter(4, [0.168, 0.174]);  
output2 = filter(d,c,output1);
```

3. Bandpass filter with centre frequency 400Hz and bandwidth of 35Hz around it

```
[f,e] = butter(4, [0.03825, 0.04175]);  
output3 = filter(d,c,output1);
```

4. Frequency spectrum plot (*fft*) code

```
sample_size = 65536;  
f_sampling = 20000;  
N = 2^nextpow2(sample_size);  
figLen = (N/2)+1;  
fscale = (1:figLen)*f_sampling/(2*figLen);  
output_fft = fft(input,N);  
output_fft_absolute = 20*log10(abs(output_fft(1:figLen)));  
plot(fscale,output_fft_absolute);
```

5. Elliptic low pass filter with cut-off frequency 100Hz applied to peak detector output

```
[h,g]=ellip(3,0.5,50,0.01,'low');  
output4 = filter(h,g,output_pk);
```

6. Comparator function for decision signal for positive and negative peak detector outputs

```
for i=1:sample_size_pos  
    if(output4P(i)>=0.08)  
        Pdecision(i) = 1;  
    else if(output4P(i)<0.08)  
        Pdecision(i) = 0;  
    end  
    i=i+1;  
end  
end  
for j=1:sample_size_neg  
    if(output4N(j)<=-0.08)  
        Ndecision(j) = 1;  
    else if(output4N(j)>-0.08)  
        Ndecision(j) = 0;  
    end  
    j=j+1;  
end  
end
```

Curriculum Vitae

Name: Sneha Lele

Post-Secondary Education and Degrees: University of Mumbai
Mumbai, India
B.E. (Electronics)
2002 - 2006

University of Western Ontario
London, ON
M.E.Sc. (Electrical and Computer Engineering)
2008 - 2009 (Transferred to doctorate program)

University of Western Ontario
London, ON
Ph.D. (Electrical and Computer Engineering)
2009 - 2013

Related Work Experience: Teaching Assistant
University of Western Ontario
Electrical and Computer Engineering
2008 - 2013

Executive Engineer
Siemens Ltd., India
Transportation Systems Division (now Mobility)
2006 - 2008

Publications:

1. S. Lele, R. Sobot, and T. Sidhu, Piezoelectric Transformer Based Disturbance Monitoring Methodology for High-Voltage Power Supply Lines – under review with IEEE Sensors Journal (Manuscript No. Sensors–8737–2013)
2. S. Lele, R. Sobot, and T. Sidhu, Numerical Modelling of Piezoelectric Transformers for Low Frequency Measurement and Disturbance Monitoring in Power Systems, IEEE Electrical Power and Energy Conference at London (EPEC 2012), London ON, Canada, October 10-12, 2012
3. S. Lele, R. Sobot, Piezoelectric Transformers for Low Frequency Measurement in Power Systems, IEEE International Conference for Upcoming Engineers (ICUE 2012), Toronto ON, Canada, August 2, 2012 (3rd place Student Paper award)
4. S. Lele, R. Sobot, and T. Sidhu, Frequency Measurement and Disturbance Monitoring Using Piezoelectric Transformers, Power and Energy Conference at Illinois (PECI 2012), Illinois, U.S.A., February 24-25, 2012
5. N. Najmaei, S. Lele, M.R. Kermani, and R. Sobot, Human Factors for Robot Safety Assessment, IEEE/ASME International Conference on Advanced Intelligent Mechatronics (AIM 2010), Montreal, Canada, July 6-9, 2010
6. S. Lele, R. Sobot, M. Waxer and J. Bruce Morton, Steady-state Visually Evoked EEG Signal Processing with Tuneable Continuous-time Bandpass Sigma-Delta Modulators, 19th European Conference on Circuit Theory & Design (ECCTD 2009), Antalya, Turkey, August 23-27, 2009